Wave-Assisted Propulsion for Autonomous Surface Vehicles

by

A thesis submitted to the

School of Graduate Studies

in partial fulfillment of the requirements for the degree of

Master of Engineering

Faculty of Engineering & Applied Science

Memorial University of Newfoundland

May 2018

St. John's Newfoundland

Abstract

Renewable energies, such as solar and wind, have been employed in the recent past to power and propel unmanned marine vehicles. In most cases however, the possibility of using wave energy is not considered. Therefore, in this thesis project, the thrust generating capacity of an oscillating hydrofoil in head seas is investigated. A mathematical model is presented that computes the forces on a two-dimensional hydrofoil oscillating in pitch. Existing empirical force coefficients are used to estimate the horizontal and vertical forces generated by the hydrofoil based on the effective angle of attack. A simulation case is then developed in OpenFOAM enabling the effects of wave height, wave frequency, foil pitch amplitude, and forward speed to be studied. To evaluate theoretical and simulation results, a hydrodynamic testing platform is developed using a DC motor to actuate the foil and a four load cell arrangement to measure forces. The experiments are performed in the wave tank of Memorial University of Newfoundland. Design of experiments methodologies are used to develop regression equations for simulated and physical data. A comparison of both model equations reveals that the simulation model is slightly offset from the physical model; however both models show that thrust can be achieved in head seas by using an actively pitch-controlled hydrofoil in low current conditions.

Keywords— OpenFOAM, Auxiliary Propulsion, Oscillating Foil, Design of Experiments

Acknowledgements

First and foremost, I would like to thank my supervisor, Dr. Ralf Bachmayer, for suggesting the research topic and providing many opportunities for growth and development. My time in Bremen was a particular highlight that will not soon be forgotten.

My colleagues at the Autonomous Oceans Systems Laboratory were integral to my success. Throughout my research process they provided much help and guidance, and for that I am grateful. Special thanks goes to Mihajlo Ćurčić for developing the initial control algorithm and to Vincent Sobalski for sometimes putting my work above his own.

To Dave Snook, and the rest of the staff at Technical Services: I thank you for your knowledge, patience, and ability to provide solutions on short notice.

Next, my gratitude goes to Trevor Clark, and the rest of the staff at the Ocean Engineering Research Center. During times beyond our control you have managed to keep my spirits high.

To my family, old friends and new, I thank you for providing support, perspective and some fun mixed in between.

Lastly, I must thank my girlfriend Joelle Monaghan, for her never-wavering support, roller coaster of emotions, and visiting me no matter where I go. Without you, this thesis would not have been possible.

Contents

List of Tables

List of Figures

Chapter 1

Introduction

1.1 Motivation

Besides the apparent benefit of offsetting fuel costs by harnessing freely available energy, tapping into a renewable energy resource, such as the energy stored in waves, holds sway for many other environmental and political reasons. The main argument for the former is climate change and of particular importance to this investigation is the melting of the polar ice cap. The Arctic sea ice extent is decreasing at a rapid rate of 7.8% per decade in summer months [4]. This has Arctic-neighbouring countries racing to survey newly accessible areas in order to better define their country boundaries and claim potential resources. In addition, less sea ice means an Arctic shipping route may now be feasible. These geopolitics, in turn, motivate further research in oceanographic observation in harsh ocean environments. More specific to this investigation is the monitoring and tracking of icebergs after they separate from western Greenland and threaten the offshore industry. Increased activity in northern waters means increased proximity to icebergs; and therefore knowledge of trajectory, size and condition is paramount for engineers and operators. The challenge becomes finding a means of recording all of these measurements in a cost-effective, sustainable and safe manner.

Autonomous and unmanned marine vehicles have become more prevalent in recent years as they provide a means to monitor and observe ocean environments with minimal supervision, and in zones that are otherwise dangerous or inaccessible for humans. They can be categorized into autonomous underwater vehicles (AUVs) and autonomous surface vehicles (ASVs). AUVs can use propellers and sometimes changes in buoyancy to propel themselves in the desired direction. ASVs can also using traditional propulsive methods such as a propeller for propulsion, but this requires sufficient battery capacity for the desired deployment, which in turn, has a relationship with the size of the vehicle. Hence, a small-scale ASV will require alternative means of subsistence in order to remain operational for long periods of time. This has spawned research into alternative propulsive mechanisms using renewable energy.

Perhaps the most obvious form of energy harnessing for propulsion is the oldest - sailing. Although mostly restricted to pleasure craft and sport, using wind for power and propulsion makes sense for small research-oriented vehicles. While using sails can reduce the drag on the vessel, it generally also requires the vessel to heel under normal operation, which can be undesirable for many applications. Solar panels are also increasingly prevalent in helping power propulsion and other on-board systems alike. Wave energy, however, has taken the longest to be applied, undoubtedly due to the difficulty of successfully designing a wave-energy harnessing system. The following autonomous marine vehicles have employed some form of energy harnessing with varying degrees of success (Table 1.1).

Table 1.1: Energy Harnessing Autonomous Surface Vessels

Manufacturer	Vessel Name	Size (LxWxT) [m]	Means of Propulsion
AMS	Datamaran [5]	2.5 x 1.7 x 1	wind, electric
ASV	C-Enduro [6]	4.2 x 2.4 0.4	diesel, solar, wind
MOST	Autonaut [1]	scalable	wave
Liquid Robotics	Wave Glider [7]	3.05 x 0.81 x 0.23 (float)	wave, electric

Figure 1.1 shows the Autonaut by Autonaut Ltd. [1]. It moves forward using the waves, where the up and down motions of the hull are converted directly into propulsive thrust using fixed hydrofoils between the bow and stern of the vessel. It can achieve speeds up 1.2 knots using its wave propulsion system, and also makes use of solar panels to satisfy powering requirements for its navigation, communications and payload systems.

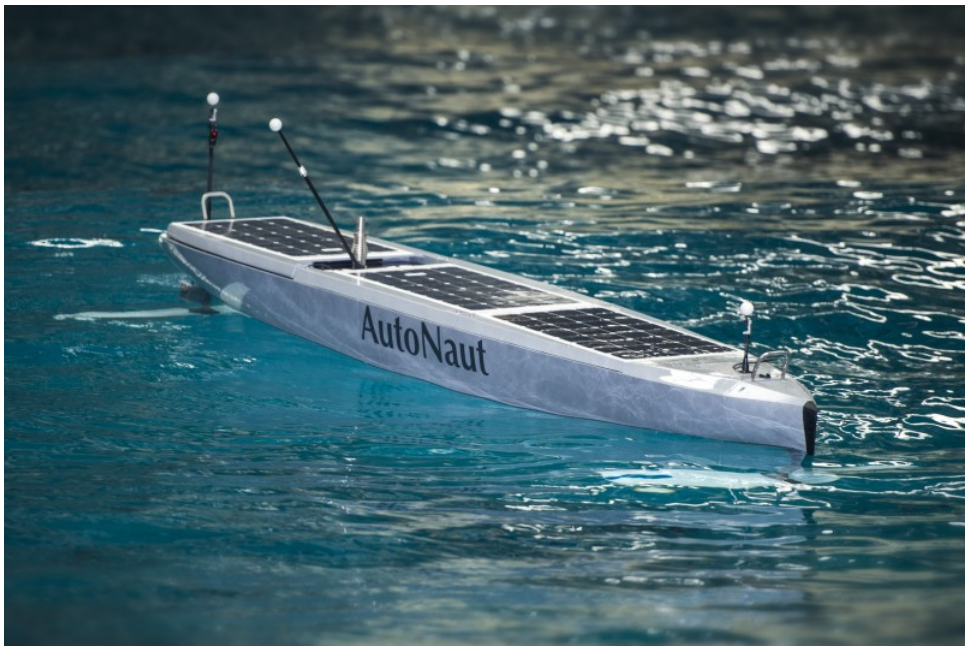

Figure 1.1: The Autonaut from Autonaut Ltd. [1]

The North Atlantic has been shown to be a region of high wave energy density, in fact

most of the global ocean has an energy density[1] above 2kW/m [8], which begs the question of why using wave energy for propulsive means has not been more successful. Interestingly, wave energy itself as a means of propulsion is far from a new idea, as examples of such ideas can be seen as far back as 1858 [2], as Figure 1.2 illustrates. Despite remaining several decades behind wind energy, research into wave energy devices is progressing, as evidenced by the appearance of several commercial business ventures.

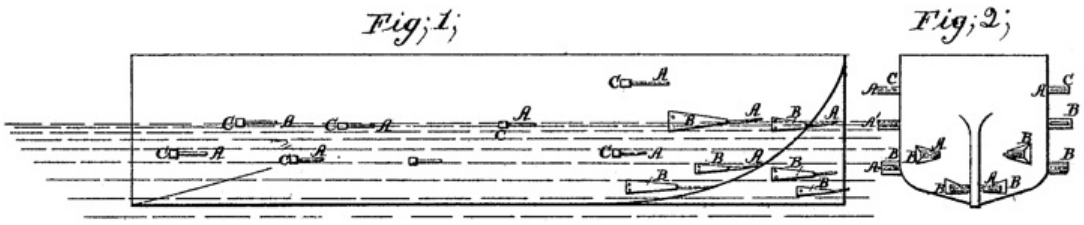

Figure 1.2: US patent submitted by Daniel Vrooman in 1958 describing fins attached to a vessel to aid in propelling itself forward in waves. [2]

One common theme in using wave motion for propulsive means is the presence of a fin or foil shape; an idea drawn logically from the evolution of fish locomotion. Throughout the years, some of the research has focused on actively driving a foil, while another branch focused on a passively driven foil to achieve thrust in waves. These fields have been referred to as flapping foil propulsion and wave-devouring propulsion respectively [9], [10]. The focus of this investigation is to determine whether a hydrofoil, when actively controlled, can be used to achieve forward motion against head seas and to help provide insight into methods where thrust could be achieved passively. What sets the current investigation apart from vehicles such as the Autonaut [1] and the Wave Glider [7], is the desire to have a stable sensor platform by eliminating vessel pitch motions and maintaining the heave motions at a minimum. Correspondingly,

[1] wave energy flux, or energy transfer, per unit crest length of a wave

the objective is to determine the effectiveness of submerged foils restricted to pitch motion only, and their ability to produce thrust in linear ocean waves.

1.1.1 Autonomous Ocean System Laboratory

The Autonomous Ocean Systems Laboratory (AOSL) located at Memorial University of Newfoundland (MUN) focuses on developing systems and technologies for harsh ocean environments. Within the last five years, the lab has designed and built a surface vehicle to be used as a sensor platform for monitoring icebergs [11]. The next iteration of this vehicle will attempt to improve on some shortcomings of the initial design and incorporate changes based on lessons learned, namely motion control and ease of launch and recovery. The vehicle in question will employ two control surfaces on either side of the hull for manoeuvring purposes. The possibility of exploiting the energy stored in waves by using these control surfaces is the focus of this thesis.

1.2 Flapping Foil Propulsion

1.2.1 Theoretical Studies

Biomimicry is a field of study where techniques founded and perfected in nature are applied to the design of smarter and more efficient systems and structures [12]. When considering the propulsion of ocean-going vehicles, the movement of a fish is an obvious starting point. Such an analysis was performed by Wu [13] in the 1960s where the mechanisms of fish locomotion were studied. Shortly after, another investigation was carried out by Lighthill [14] and is one of the main contributors of what today can be labelled as flapping foil propulsion. Lighthill used inviscid-flow theory to develop

an expression for the thrust in a slender-bodied fish, and goes on to discuss efficient conditions for thrust development, such as oscillatory motions and confining fin motion to the rear portion of the fish. Chopra [15], [16], further generalized Lighthill's work and discusses the effects of aspect ratio, reduced frequency, feathering parameter and pitch axis location and how they affect thrust.

More recently, Bose and Yamaguchi [17] investigated using oscillating fins as ship propulsion, where it was determined that an oscillating propulsor resulted in efficiencies 5% higher than a comparable conventional screw propeller. However, the difficulties of developing a suitable driving device are also mentioned.

In addition to those presented, many other theoretical investigations into flapping foil propulsion can be found in the literature [18], [19], [20], [21], [10].

1.2.2 Experimental Studies

In terms of experimental investigations, the majority of research employs a foil-shaped fin which oscillates in heave and pitch, and much of which was performed at the testing tank facility of Massachusetts Institute of Technology. Anderson et al. [22] performed experiments on a harmonically oscillating foil to study the flow around and in the wake of the foil. It was found that under optimal conditions of wake formation efficiencies of up to 87% could be achieved. During these conditions, the development of a leading edge vortex (LEV) every half wave cycle was noted, which resulted in the formation of a reverse Kármán Street. Read et al. [23] performed similar experiments, and found that maximum efficiency occurred with a 35 degree maximum angle of

attack. These authors also reported that a phase difference of 90-100° between pitch and heave motions resulted in the best performance.

As part of his PhD thesis [24], Bockmann performed model experiments with a platform supply vessel outfitted with a hydrofoil attached to the vessel hull. It was discovered that actively pitching foils resulted in less resistance than a fixed foil, while the importance of the phase difference between the heave and pitch motions was also noted.

With regards to small marine vehicles, a biomimetic AUV was designed employing flapping foil propulsion as the main means of propulsion [25]. Four independent foils were installed, and enabled the vehicle to achieve a maximum speed of 0.1 m/s. For a more complete review of experimental work in biomimetic foils see [26].

1.3 Wave Devouring Propulsion

1.3.1 Theoretical Studies

Concerning energy harnessing, Wu [27] studied the extraction of flow energy from an existing wave stream by considering an oscillating hydrofoil in a sinusoidal gravity wave. He states that an advantage can be taken from an existing wave to the fullest extent primarily through appropriate phase selection of the foil heaving motion. While free-surface effects are neglected, Wu reports that flow energy and a net mechanical power can be extracted from the flow when waves of a sufficiently large amplitude are present.

Also investigating flow energy extraction, labelled as "wave-devouring propulsion" as

proposed by Prof. M Bessho in 1980, Isshiki performed a theoretical analysis of the problem in his first two, [28], [29], of four reports. In the first report, a free-surface approximation is added to Wu's model, and an analysis is performed on a linear Wells (non-oscillating) turbine which highlights the importance of including free-surface effects. In the subsequent report, optimum foil motions are suggested which serve one of two purposes; namely, maximizing thrust output or minimizing the ratio of leading edge suction and thrust to avoid leading edge separation.

Returning to biomimicry, Bose & Lien [30] investigate the capacity of a whale fluke in absorbing some of the required propulsive power for whale propulsion using a hydrofoil as a conversion device. It was found that a power savings of approximately 25% could be achieved in head seas by absorbing wave energy.

Simulations on an actively pitch-controlled biomimetic wing performed in [31] using a boundary element code show that actively controlling the foil pitch motions generally results in thrust producing motions. It is also stressed that the power necessary for pitch control is a small percentage of the propulsive force generated. Further simulations on energy extraction of a two-dimensional hydrofoil in waves were performed in [32], which identified several design parameters which can significantly affect thrust production. Further investigations of the foil frequency parameter indicate that maximum efficiency is achieved when the hydrofoil oscillates at the wave encounter frequency. Furthermore, it was noted that efficiency and thrust reach a maximum when the was has a -90 degree phase difference with the foil heave motion, due to high utilization of the wave orbital velocity.

Using the same simulation software as used in the present study, Esmaeilifar et

al. [33] investigated a plunging hydrofoil at various frequencies and submergence depths. It was found that the free-surface dynamics affect the trailing edge vortices (TEVs) and cause an increment in drag when the hydrofoil was at a submergence of 0.5 times the chord length. At larger submergences, this free-surface caused no effect.

1.3.2 Experimental Studies

The original inspiration for the ASV presented in Figure 1.1 is the Autonaut, built in 1895 by Herman Linden (Fig 1.3). In his British patent of a wave powered boat [3], Linden describes a floating body, adapted with fins "so as to affect its propulsion". The flat plate that projects from the stern is actuated by the wave motions, vessel motions, or both.

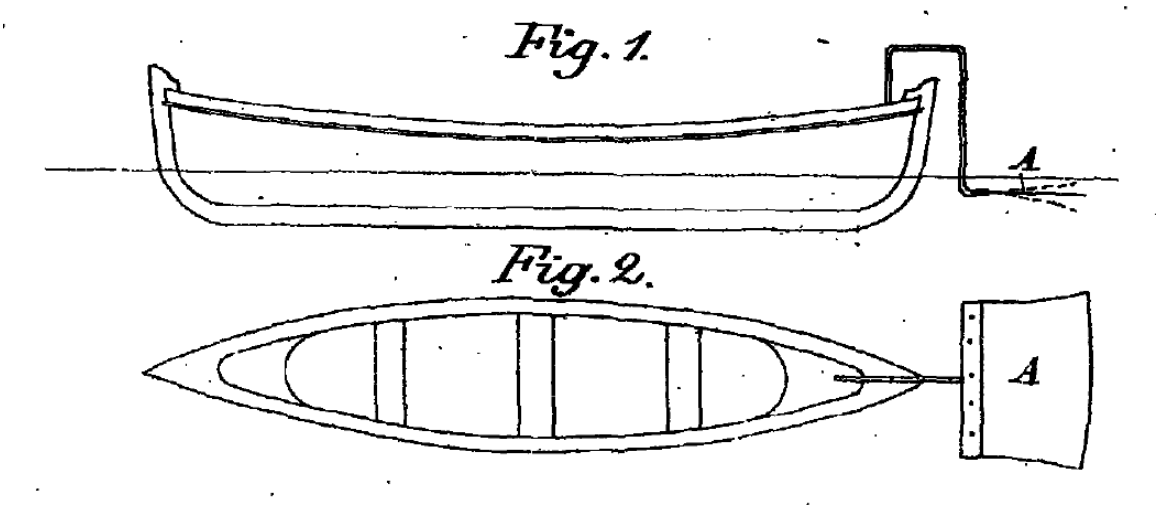

Figure 1.3: US patent submitted by Hermann Linden of the Zoological Station, Naples, describing a wave powered boat [3]

More recently, Terao [34] designed a catamaran vessel equipped with a wave devouring propulsion system (WDPS). Dual fins were installed 0.15 meters below the surface at

the bow of the vessel, both of which were equipped with a pitch restoring spring have a maximum pitch angle set to 45 degrees. In 2008, this vessel successfully crossed the Pacific ocean from Hawaii to Japan relying on wave power alone. While robust and inexpensive, one notable weakness of the WDPS is the narrow band of wave frequencies that resulted in optimal thrust production.

As well as his theoretical developments, Bockmann [35] performed experiments with a horizontal hydrofoil undergoing oscillatory motions while moving at a constant forward speed. In these experiments two pitch strategies were tested; the first making use of a motor to actively pitch the hydrofoil based on a specified control algorithm, and the second using pitch springs on the foil to cause a restoring force. It was found that higher efficiencies could be achieved with the spring loaded case when the pitch motion led the heave motion by 90 degrees.

In another experimental analysis, Bowker implements a flapping energy utilization and recovery (FLEUR) system aboard a small surface vessel [36] that provides a thrust production mode and energy recovery mode. On the vessel, a foil is connected on a pivot arm which is attached to the vessel at the bow and stern portions of the hull. In the thrust production mode, thrust was produced when the pivot arm is fixed and the foil oscillates passively due to hull and wave motions. The spring constant of the foil is altered by adjusting the working length of a piece of spring steel. In energy recovery mode, the pivot arm is free to rotate such that the energy exerted on the foil serves to turn a rotary damper.

Further experimental examples of wave devouring propulsion can be found [37], [38], [39].

1.4 Thesis Outline

In Chapter 1, the benefits of using waves as a means of propulsion are discussed and provides motivation for the thesis project. Flapping foil propulsion and wave devouring propulsion are introduced as existing branches of wave energy harnessing and a literature review of relevant research is provided. In Chapter 2, quasi-steady and fully unsteady mathematical models of a two-dimensional oscillating hydrofoil in linear ocean waves are developed. The presented models allows for some preliminary analysis wherein the results are used to govern parameter selection in simulation and physical experiments. The development of the computational fluid dynamics (CFD) simulation model is outlined in Chapter 3. The governing equations are presented and discretized and the background mesh is created and refined to ensure important phenomena are captured. The simulation results are computed and a polynomial regression equation is presented. In Chapter 4, a hydrodynamic testing platform is developed to house the hydrofoil and enable the simulated results to be verified. The platform is designed to fit the towing carriage at the Ocean Engineering Research Center (OERC) and only permits the foil to rotate in pitch. The required electronics and foil control strategies are also presented. The experimental design is developed in Chapter 5 and ground truth tests are first performed to ensure the platform is capable of producing reasonable results. Next, the oscillating foil experiments are performed and the results are presented and analyzed. A polynomial regression equation is developed and compared with that of the simulation model. Lastly, conclusions and recommendations of future works are presented in Chapter 6.

Chapter 2

Mathematical Model

This chapter will introduce two mathematical models helping to understand the system dynamics and justify the selection of parameters for numerical simulation and physical experimentation. The first is the quasi-steady model, which computes forces on the hydrofoil at successive instants in time using static empirical force coefficients. The second is a fully unsteady model, which augments the quasi-steady model by taking into account added mass and wake effects. The outcomes of the mathematical models indicate that there exists a significant benefit in an oscillating versus a stationary hydrofoil and that the hydrofoil pitch amplitude and the phase lag between foil angle and the wave are significant variables. It is also shown that thrust increases with the hydrofoil oscillation frequency and amplitude, and decreases with increasing current velocity or forward speed.

2.1 Overview

In order to better define the model, there are various assumptions and variable ranges that must be set. Linear, deep water waves are assumed, and 2-D airfoil theory is

adopted. The initial chord length is selected based on a preliminary study of the directional deviation of the flow vector across the chord length of the foil. Figure 2.1 shows the directional deviations for eight different wavelength to chord length ratios. The dotted line represents the maximum allowable deviation, which is chosen to be $\frac{1}{20}$ radians (2.86°), due to the wave lengths that it accommodates. Consequently, for a ratio of 150, a foil with a 0.25 meter chord length is suitable for wavelengths as short as 37.5 meters, which is on the lower end of possible ocean wavelengths [40]. Thus it can be assumed that the foil as a whole receives the same flow directionality, and this assumption becomes more acceptable as the ratio increases. Another consideration for determining the chord length is based on practical reasons. For wave tank experimental work at the Ocean Engineering Research Center (OERC) at Memorial University of Newfoundland (MUN), free surface effects of the waves due to the foil are neglected. As such, it is recommended that a submergence of three times the chord length be retained [27]. The maximum physically achievable submergence is 0.6 meters, and is thus used in simulation as well as experimentation. The wave specifications and current speeds selected were also constrained by the OERC hydraulic wave board, and towing carriage. Wave frequencies ranging from 0.3-0.5 Hz, and wave heights ranging from 10 - 50 cm are selected. A current velocity range of 0 - 0.4 m/s is selected to assess the impact of an oscillating foil at low speeds only. The span of the foil is selected following the constraints of 2D foil theory which increases in validity with a higher aspect ratio [41]. An aspect ratio of 4 is selected resulting in a foil span of one meter. Lastly, the foil shape was chosen as a NACA 0015, due to the abundance of relevant data available including empirical force coefficients for large attack angles. In future works, different profiles (unsymmetrical, dual-symmetric) could be tested to optimize the shape for thrust production. Table 2.1 highlights the wave and foil particulars chosen.

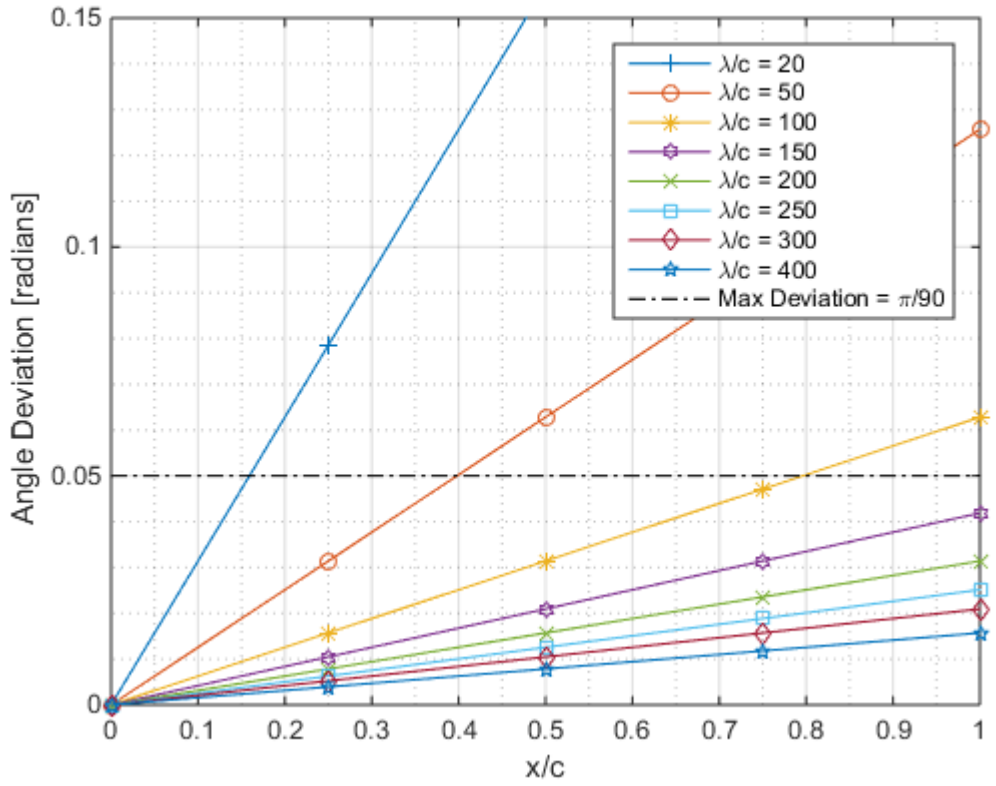

Figure 2.1: The deviation of fluid velocity direction across the chord length of the foil. $\frac{1}{90}(2.86°)$ is chosen as the max allowable deviation.

Table 2.1: System Particulars

Parameter	Value	Units
Chord Length	0.25	m
Submergence	0.6	m
Span	1	m
Wave Frequency	0.3 - 0.5	Hz
Wave Amplitude	1 - 5	cm
Current Velocity	0 - 0.4	m/s
Density	1000	kg/m^2
Reynolds Number	10^4-10^5	

With the parameters selected, the model is implemented in MATLAB® [42]. The fundamental feature of the model is ensuring the empirical force coefficients change appropriately to reflect the angle of attack throughout the wave. The angle of attack will depend on the phase of the wave, the position of the foil, and the presence of a current. All three components are necessary to define the angle of attack.

2.1.1 Linear Wave Theory

In order to define the phase of the wave, and ultimately the angle of attack on the hydrofoil, a description of the waves is necessary. Accordingly, a brief overview of linear wave theory is provided.

Consider first, the case of a submerged, stationary hydrofoil in waves with zero current. The surface profile and particle velocity equations can be derived by making several assumptions. Firstly, assuming that the fluid is inviscid, incompressible, and irrotational allows the flow velocity to be described in terms of velocity potential ϕ as shown in Eq. 2.1 below:

$$u = \frac{\partial \phi}{\partial x}; w = \frac{\partial \phi}{\partial z}; \tag{2.1}$$

Since the velocity in the y-direction is assumed to be zero, it is omitted from the derivation.

Next, the incompressibility assumption (ρ is constant) is described using the continuity equation (Eq. 2.2), and when combined with Equation 2.1 the Laplace equation (Eq. 2.3) results:

$$\frac{\partial u}{\partial x} + \frac{\partial w}{\partial z} = 0; \tag{2.2}$$

$$\frac{\partial^2 \phi}{\partial x^2} + \frac{\partial^2 \phi}{\partial z^2} = 0 \tag{2.3}$$

The Laplace equation is a second order partial differential equation and as such, boundary conditions are necessary to provide a solution. In total, three boundary conditions are needed; one at the bottom and two at the water surface. They are commonly known as the bottom boundary condition, the kinematic boundary condition, and the dynamic boundary condition. Figure 2.2 shows the defined boundaries.

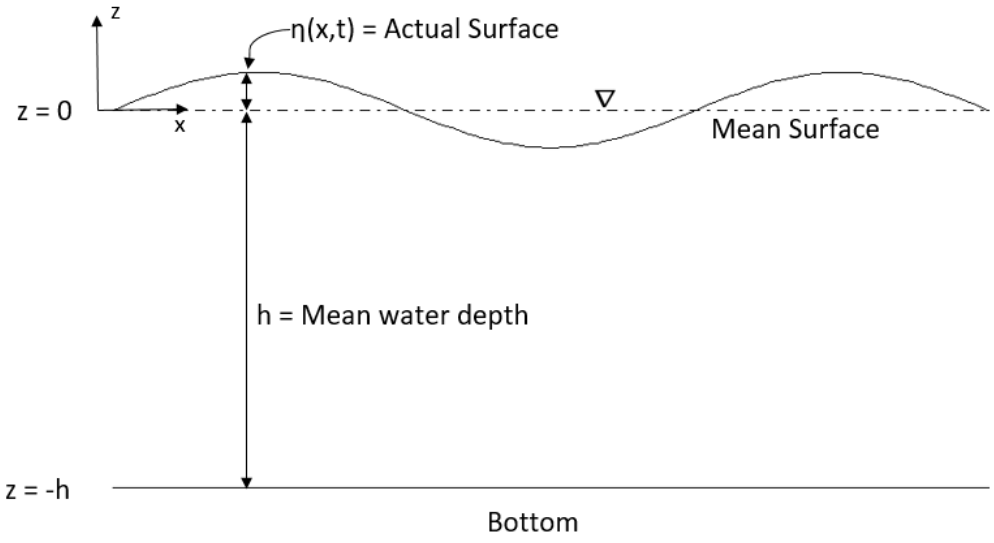

Figure 2.2: Boundary Definitions

The bottom boundary condition (Eq. 2.4) states that the vertical velocity at the bottom surface (z = -h) is equal to zero. This is only the case if the bottom surface is assumed impermeable.

$$w(-h) = 0 \tag{2.4}$$

The kinematic boundary condition (Eq. 2.5) occurs at the water surface ($\eta = 0$) and physically states that the fluid particles near the surface will remain near the surface provided the waves do not break.

$$\frac{\partial \eta}{\partial t} + u\frac{\partial \eta}{\partial x} = w \tag{2.5}$$

The pressure at the water surface is assumed equal to the atmospheric pressure. Since the surface elevation η is an extra unknown, the dynamic boundary condition at the free surface is needed. This can be mathematically described using Bernoulli's equation for unsteady, irrotational flow shown in Equation 2.6 below.

$$\frac{P}{\rho} + \frac{\partial \phi}{\partial t} + \frac{1}{2}(u^2 + w^2) + g\eta = 0 \tag{2.6}$$

At this point, the general case of the Laplace equation (Eq. 2.3) cannot yet be solved and further assumptions must be made. In the case of small amplitude waves (i.e. cases where the wave amplitude is much smaller than wavelength), the kinematic and dynamic boundary conditions can be linearized using dimensional analysis and scaling. The full system of equations for small-amplitude waves, including the linearized boundary conditions, is stated below:

$$\frac{\partial^2 \phi}{\partial x^2} + \frac{\partial^2 \phi}{\partial z^2} = 0 \tag{2.7}$$

$$w(-h) = 0 \tag{2.8}$$

$$\frac{\partial \eta}{\partial t} = w(0) \tag{2.9}$$

$$\frac{\partial \phi}{\partial t} = g\eta \tag{2.10}$$

The system is solved for the velocity potential ϕ by assuming a wave-like form, and ensuring the assumed form satisfies the linearized boundary conditions. For a full derivation of small-amplitude waves using velocity potential see [43] or [44]. Ultimately, the form shown in Eq. 2.11 results.

$$\phi = \frac{gA}{\omega}\frac{cosh(k(z+h)}{cosh(kh)}cos(\omega t - kx) \tag{2.11}$$

Where g is the acceleration due to gravity, ω is the wave angular frequency, A is wave amplitude, and k is the wave number which represents spatial frequency. Additionally, if only deep-water waves are considered (i.e. $A << h$) then the velocity potential can be further reduced to:

$$\phi = \frac{gA}{\omega}e^{kz}cos(\omega t - kx) \tag{2.12}$$

By deriving Eq. 2.12 with respect to the corresponding coordinate direction, the particle velocity equations are computed. The expression for the wave surface profile can be derived from the linearized dynamic boundary condition (Eq. 2.10). All three equations are stated below. The wave surface profile and the particle velocity vector at a fixed location are illustrated in Fig. 2.3 over one wave cycle.

$$u = \omega A e^{kz} sin(\omega t - kx) \tag{2.13}$$

$$w = \omega A e^{kz} cos(\omega t - kx) \tag{2.14}$$

$$\eta = A sin(\omega t - kx) \tag{2.15}$$

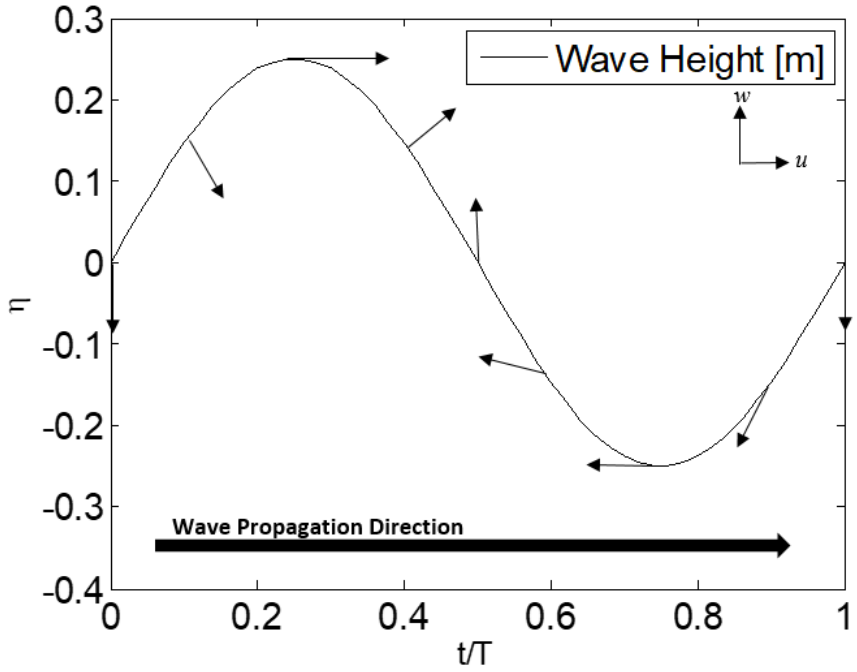

Figure 2.3: Wave profile and wave particle velocity components. The x-axis represents the ratio of time to wave period at a fixed location in the wave field.

The particle velocities can be combined into the flow vector, $\vec{V}$:

$$\vec{V} = \begin{bmatrix} u \\ w \end{bmatrix} \tag{2.16}$$

2.1.2 Wave Phase

The phase angle Φ of the wave reveals the position of the wave relative to a reference location at a certain point in time. Normally, this is the product of the wave angular frequency ω and time, and rotates from zero to 2π. However, if a current velocity $\vec{U_c}$ is present, the combination of a wave and current can actually cause the combined phase angle to oscillate rather than rotate. The current velocity is defined as:

$$\vec{U_c} = \begin{bmatrix} U_c \\ 0 \end{bmatrix} \tag{2.17}$$

Where U_c acts in the positive x direction. Using Figure 2.4 as a reference, consider the case when a current velocity (green arrow) is present and larger in magnitude than the flow vector (blue arrow). The wave component is set such that the initial component acts vertically downward.

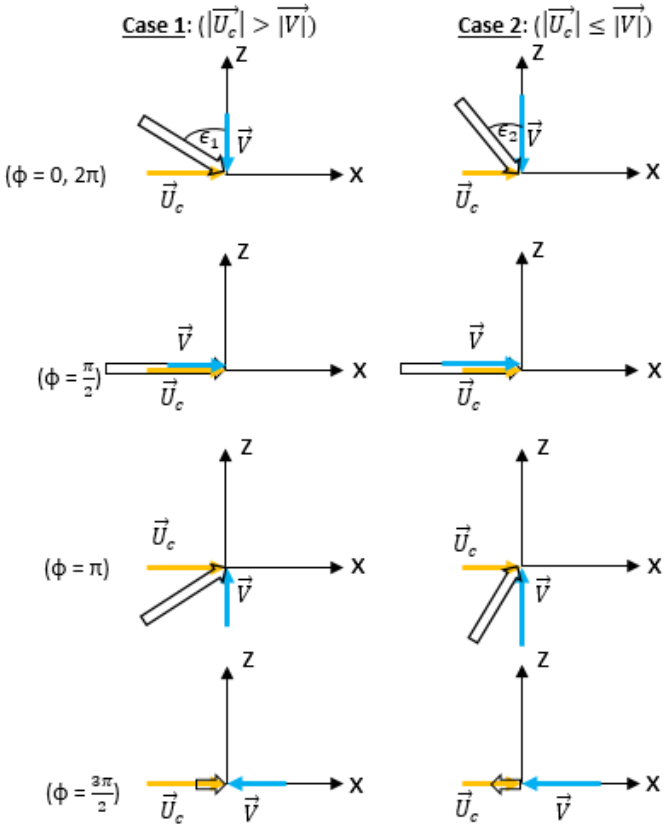

Figure 2.4: The starting wave phase angle ϵ and the motion of the resultant vector is dependent on the wave and current velocity vectors.

In Case 1, the presence of a current changes the initial wave phase angle ϵ compared to the wave-only case and also causes the resultant wave phase (black arrow) to *oscillate* instead of undergoing a rotation. This occurs since the current velocity cancels out the wave velocity when the flow vector acts in the negative x direction ($\pi < \Phi < 2\pi$). In contrast, when the current magnitude is less than the flow vector magnitude (Case 2), the starting phase angle will be altered to a different angle than Case 1, and the phase angle will continue from this starting position and undergo a full rotation per wave cycle. Here the resultant magnitude of the current and wave components acting against the current direction (i.e. this occurs when $\pi < \Phi < 2\pi$) will be much smaller than the wave-only case, but is at least present unlike in Case 1. To account the combined effect of wave and current within the model, logical statements are used. The combined wave phase and the starting angle are defined below:

$$\Phi(t) = \frac{3\pi}{2} + \epsilon + var1(\omega t) + var2[(\frac{\pi}{2} - \epsilon) * cos(\omega t + \frac{\pi}{2})] \tag{2.18}$$

Where var1 and var2 can equal 0 or 1 depending on the magnitudes of $\vec{U}c$ and $\vec{V}$. The $\frac{3\pi}{2}$ is added to make the initial wave component act downward as in Figure 2.4. The starting angle ϵ depends on the magnitudes of wave particle and current velocity vectors:

$$\epsilon = acos(\frac{|\vec{V}|}{\sqrt{|\vec{V}|^2 + |\vec{U_c}|^2}}) \tag{2.19}$$

In addition to the wave phase, the instantaneous foil angle, $\varphi(t)$, must also be known before the angle of attack can be defined. The position of the hydrofoil is defined as:

$$\varphi(t) = H_{foil} sin(\omega t + \psi) \tag{2.20}$$

Where H_{foil} is the hydrofoil amplitude and the phase lag, ψ, is added to investigate the effect of phase differences between the foil and wave. Note that the wave angular frequency ω also defines the foil oscillation frequency. Conceivably, in larger period waves commonly found in the Atlantic ocean, it may be possible to make use of a drag plate to take advantage of the forward and reverse flow halves of the wave. For instance to move in the wave propagation direction, the drag plate could be set to horizontal during the reverse flow half of the wave, and vertical during the forward flow half. This could be reversed when moving against the wave. The choice of sinusoidal motion for active wave energy harnessing is derived from the motion of linear ocean waves, and the eventual desire to create a fully passive wave harnessing system.

At this point the angle of attack on the foil can be defined as:

$$\alpha(t) = \varphi(t) + \Phi(t) \tag{2.21}$$

Lastly, there is also a downwash, or induced vertical velocity on the hydrofoil caused by the pitching motion at the 1/4 chord position [45]. A representative flow can be generated by the heave motion at the 3/4 chord position. This can also have an effect on the angle of attack on the foil, however it was not considered in the model due to the relatively small pitch amplitudes.

2.1.3 Model Dynamics

With the angle of attack defined, the model is now capable of computing the forces on an oscillating foil in waves. Figure 2.5 illustrates the foil angle, φ, attack angle, α, the flow vector, $\vec{V}$ (shown in blue) as well as the force progression throughout a wave cycle where the foil motion leads the wave motion by 90 degrees. It can be seen that

while the drag vector rotates with the flow velocity vector, the lift actually changes sign every quarter wave cycle. This is an important phenomenon to consider when resolving forces.

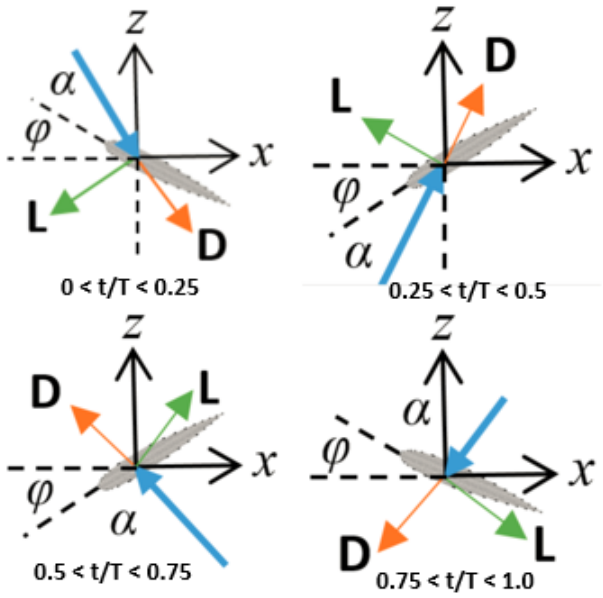

Figure 2.5: Progression of idealized forces as the flow vector (blue arrow) rotates throughout one wave cycle.

Empirical lift, drag, and moment coefficients taken from [46] have been plotted (Fig. 2.6) to permit the development of a Fourier curve-fit equation. This was performed using the curve-fitting toolbox in MATLAB® [42].

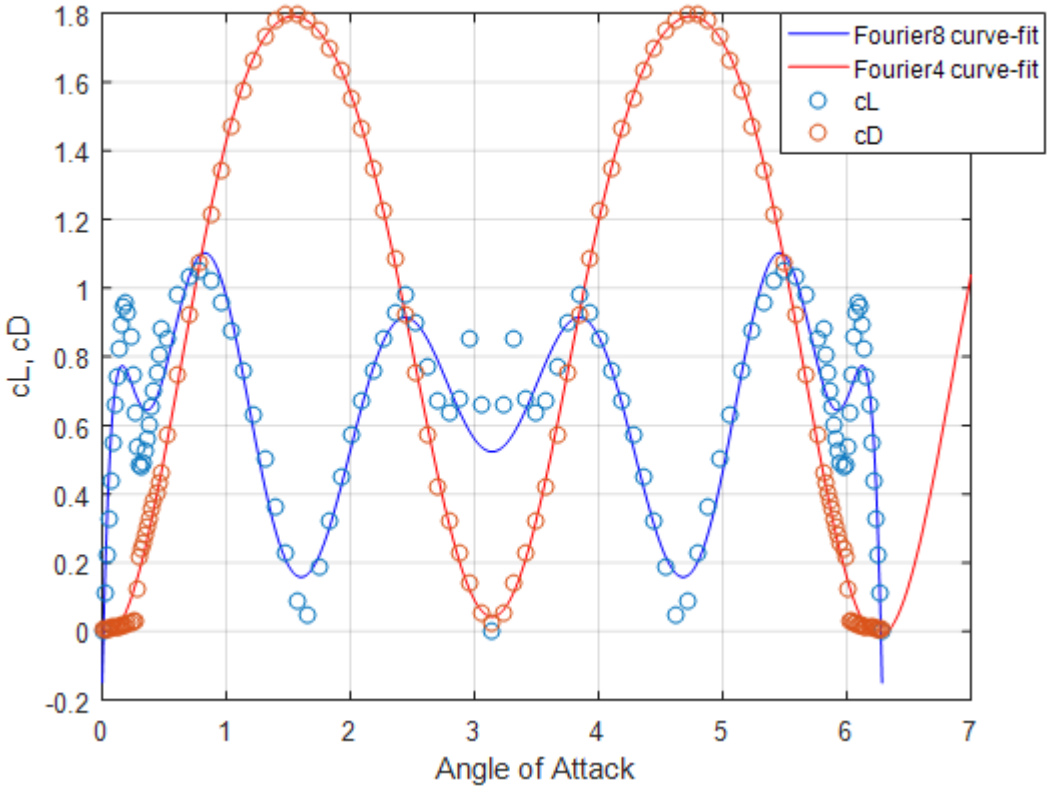

Figure 2.6: Empirical aerodynamic coefficients and Fourier curve-fit

Note that all of the lift coefficients were modified to be positive since the direction of the resultant forces is resolved using a rotation matrix. Alternatively, this can be described as a rotating flow-based coordinate system with its origin on the foil. In this manner, the lift and drag forces are first computed in the flow-based coordinate system and then rotated to the foil-fixed coordinate system to give horizontal (thrust) and vertical forces. Table 2.2 describes the coordinate systems and Figure 2.7 illustrates.

Table 2.2: Coordinate Systems

Coordinate System	Origin	X axis	Z axis
Foil-fixed	1/4 chord	Towards trailing edge when foil horizontal	Vertically upward
Flow-based	1/4 chord	Resultant flow direction	90 degrees CCW from X

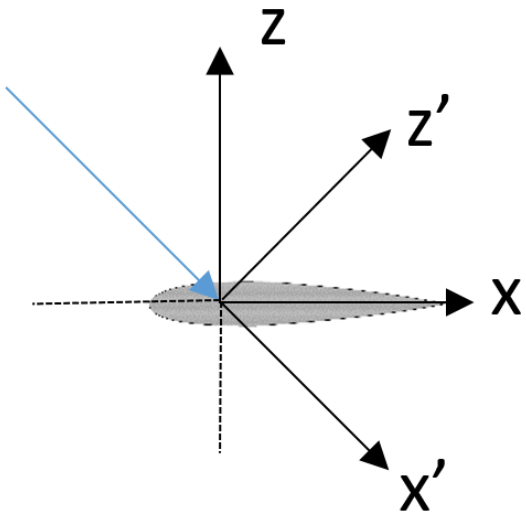

Figure 2.7: Foil-fixed (x, z) and rotating flow-based (x', z') coordinate systems. Both systems share the same origin but the flow fixed system is defined by the flow direction.

The rotation matrix uses the combined wave phase (Eq. 2.18) as the input argument. Referring back to Figure 2.5, logical statements are implemented to account for the lift force changes. The resolved horizontal and vertical forces are then computed as shown below:

$$\begin{bmatrix} F_x \\ F_z \end{bmatrix} = \begin{bmatrix} cos(\Phi) & -sin(\Phi) \\ sin(\Phi) & cos(\Phi) \end{bmatrix} * \begin{bmatrix} L \\ D \end{bmatrix} \tag{2.22}$$

Where lift, L, and drag, D, expressions are stated in the next section according to the specific model. The horizontal force component, F_x, is what enables a net force with or against the wave propagation direction. Based on the foil-fixed coordinate system defined in Figure 2.7, a negative horizontal force is desired and indicates a force opposite the wave propagation direction.

2.2 Quasi-Steady Foil Theory

A quasi-steady model applies steady state analysis to a dynamic problem and, as such, is not expected to be an accurate representation of the system. Nonetheless, it is a good benchmark for system identification and provides for comparison once the model is augmented to include dynamic influences, namely, added mass and wake effects.

The lift and drag forces for the quasi-steady model are defined as:

$$\begin{aligned} L &= \frac{1}{2}\rho A_{proj}|\vec{V}_{comb}|^2 c_L \\ D &= \frac{1}{2}\rho A_{proj}|\vec{V}_{comb}|^2 c_D \end{aligned} \tag{2.23}$$

Where A_{proj} is the projected area of the foil which is the product of chord length c and span S. $|\vec{V}_{comb}|$ is the magnitude of the combined current and wave velocity vector, and ρ is the fluid density. The non-dimensional coefficients c_L and c_D are a function of the dynamic angle of attack.

2.2.1 Fixed versus Oscillating Hydrofoil

Firstly, the quasi-steady model is used to determine if there is a noticeable benefit to an oscillating hydrofoil versus a fixed hydrofoil. In the model, the hydrofoil pitch amplitude was set to 30 degrees at a frequency of 0.5 Hz, and the current was set to 0.217 m/s. These parameters were chosen as they correspond to a Strouhal number of 0.5. The Strouhal number is a ratio of inertial forces to the flow 'unsteadiness' and is useful in unsteady, oscillating flow problems. Here, the numerator represents the transit time for a flow velocity driven water particle to move a chord length and the denominator is the foil period. It has been shown to be an integral parameter in oscillating foil propulsion [22], and can be defined as:

$$St = \frac{f 2 y_{te}}{U_c} \tag{2.24}$$

Where f is the frequency of oscillation in Hz, y_{te} is the vertical excursion of the trailing edge of the hydrofoil from the horizontal, and U_c is the current velocity. For the comparison, non-dimensional force coefficients are used as defined in Eq. 2.25. Figure 2.8 illustrates the results.

$$\begin{aligned} c_T &= \frac{-F_x}{0.5 * \rho * A_{proj} * U_c^2} \\ c_z &= \frac{F_y}{0.5 * \rho * A_{proj} * U_c^2} \end{aligned} \tag{2.25}$$

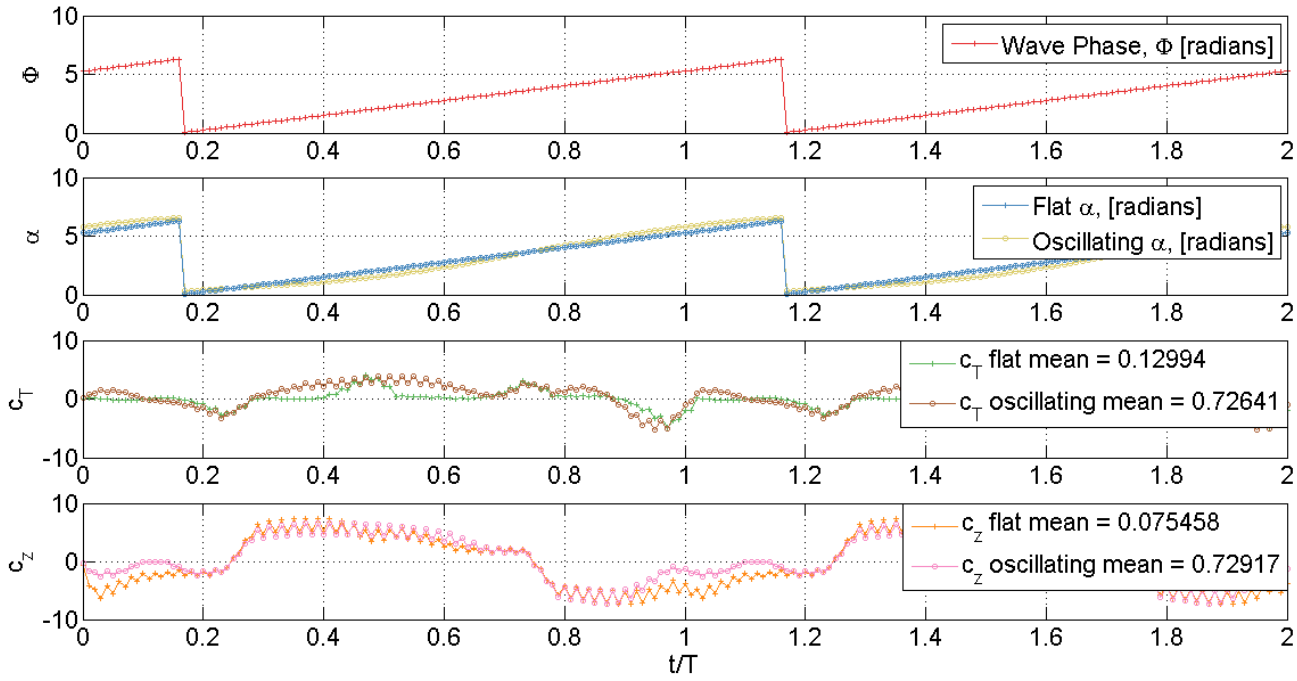

Figure 2.8: Comparison of flat versus oscillating force coefficients

The first two plots in Figure 2.8 show the wave phase and angle of attack respectively. It can be seen that the wave phase is not affected by the foil oscillations and that, logically, in the stationary case the wave phase and angle of attack are equal. When the foil is made to oscillate, the angle of attack becomes slightly curvilinear, with two inflection points at approximately t/T = 0.17 and 0.77. This corresponds to when the flow passes over the leading and trailing edges of the foil respectively, also the location where the foil angle switches sign. The sign of the foil angle causes the peak and valley to occur. When the foil angle is negative, a valley occurs, and when positive a peak occurs. Figure 2.5 and Eq. 2.21 can be useful as a reference. The thrust coefficient is noticeably increased in the oscillating case compared to the flat case with the main increase occurring when $0.25 < \frac{t}{T} < 0.75$. The increase is due to the angle of attack at first being more favourable for lift generation in the negative x (positive thrust)

direction ($0.25 < \frac{t}{T} < 0.4$) and then for drag generation ($0.5 < \frac{t}{T} < 0.7$). The vertical coefficients also see a significant increase in mean value, however the main increase happens when $0 < \frac{t}{T} < 0.2$ and $0.8 < \frac{t}{T} < 1.0$. These are the instances when both the lift and drag forces act vertically downwards. In summary, the oscillations serve to increase both thrust and vertical coefficients in the instances where they would otherwise be more negative, and do not noticeably change the maximum and minimum values. It is also worth noting that the lift coefficients go through one full oscillation during a wave length while the thrust values appear to oscillate at twice the wave frequency.

2.3 Unsteady Theory

The model was next augmented to include added mass and wake effects which are neglected in the quasi-steady model.

2.3.1 Added Mass

Added mass is a non-circulatory force produced due to the foil accelerating the surrounding fluid. Although the foil system develops forces and moments in three degrees of freedom (surge, heave, pitch), the foil itself is restricted to all degrees of freedom except pitch, and so added mass effects must be considered here. While added mass is only really known for simple shapes, it must be approximated as it can significantly affect the torque felt on the foil pivot, and thus has an effect on the dynamics and the selection of drive mechanism for controlled pitch motion. The added mass, a_{55} of a flat plate in pitch is given by [47]:

$$a_{55} = \rho\frac{\pi}{8}(\frac{c}{2})^4 \tag{2.26}$$

With the pivot point located at the quarter chord position, the corresponding added mass moment in pitch is:

$$M_{am} = a_{55}\ddot{\phi} \tag{2.27}$$

Where $\ddot{\phi}$ is the angular acceleration of the hydrofoil.

2.3.2 Wake Effects

Wake effects are circulatory effects that arise due a change in circulation about the hydrofoil. This problem was first solved by Theodorsen [48] and gives a solution to the unsteady loads on a harmonically oscillated airfoil in an inviscid, incompressible fluid. A change in angle of attack results in a change in the foil circulation Γ_{foil} about the foil. Kelvin's theorem states that the circulation must be conserved, and so there must exist a corresponding circulation $\Gamma_{te} = -\Gamma_{foil}$ that results at the tip of the trailing edge. This serves to alter the angle of attack that is *felt* by the foil. As the foil angle of attack becomes steady, the distance between Γ_{te} & Γ_{foil} increases and the quasi-steady case arises. The Theodorsen function is effectively a lift deficiency function and is given by

$$C(k_\omega) = F(k_\omega) + iG(k_\omega) = \frac{H_1^2(k_\omega)}{H_1^2(k_\omega) + iH_0^2(k_\omega)} \tag{2.28}$$

where F and G are the real and imaginary parts of $C(k)$ and $H_n^2(k)$ are Hankel functions [49]. Hankel functions are defined as

$$H_n^2(k_\omega) = J_n - iY_n \tag{2.29}$$

where J_n and Y_n are Bessel functions of the first and second kind respectively and depend on the reduced frequency k_ω. The reduced frequency is an important parameter in unsteady aerodynamics and is used to characterize the degree of unsteadiness of the problem [49]. The reduced frequency is

$$k_\omega = \frac{\omega c}{2U_c} \tag{2.30}$$

Where ω is the foil frequency, which is equivalent to the wave angular frequency, f. Based on the parameters given in Table 2.1 the reduced frequency for the present model could range from 0.0375 to 0.75. Since the majority is greater than 0.05, the flow should be modelled as unsteady [49], further justifying an unsteady model. Lastly, it should be stated that the Theodorsen function mainly accounts for the upwash and downwash caused by the shed vortices, and ignores the free surface above the foil.

2.4 Preliminary Results

The lift and drag forces, as well the moment for the unsteady model are defined as:

$$\begin{aligned} L &= \frac{1}{2}\rho A_{proj}|\vec{V}_{comb}|^2 c_L * C(k) \\ D &= \frac{1}{2}\rho A_{proj}|\vec{V}_{comb}|^2 c_D \end{aligned} \tag{2.31}$$

$$M_{pm} = \frac{1}{2}\rho A_{proj}|\vec{V}_{comb}|^2 c^2 c_m * C(k) - a_{55}\ddot{\alpha}(\frac{c}{2} - x) \tag{2.32}$$

The unsteady model parameters are stated in Table 2.3.

Table 2.3: Unsteady Model Parameters

Parameter	Description
A_{proj}	Projected area
$\|\vec{V}_{comb}\|$	Combined flow magnitude
c	Chord length
c_L	Lift coefficient
c_D	Drag coefficient
c_m	Moment coefficient
$C(k)$	Theodorsen deficiency function
a_{55}	Added mass in pitch
$\ddot{\alpha}$	Foil angular acceleration
x	Horizontal foil position where moment acts

2.4.1 Quasi-steady versus Unsteady

Figure 2.9 shows the forces for the unsteady model in comparison to the quasi-steady model. The system parameters were kept the same for both cases. It can be seen that the negative amplitude of the thrust coefficients is noticeably reduced and the shape of the positive thrust is altered. The moment sees a significant decrease in magnitude, indicating that the added mass component of Eq. 2.32 and/or the the wake (circulatory) effects given by the deficiency function are significant.

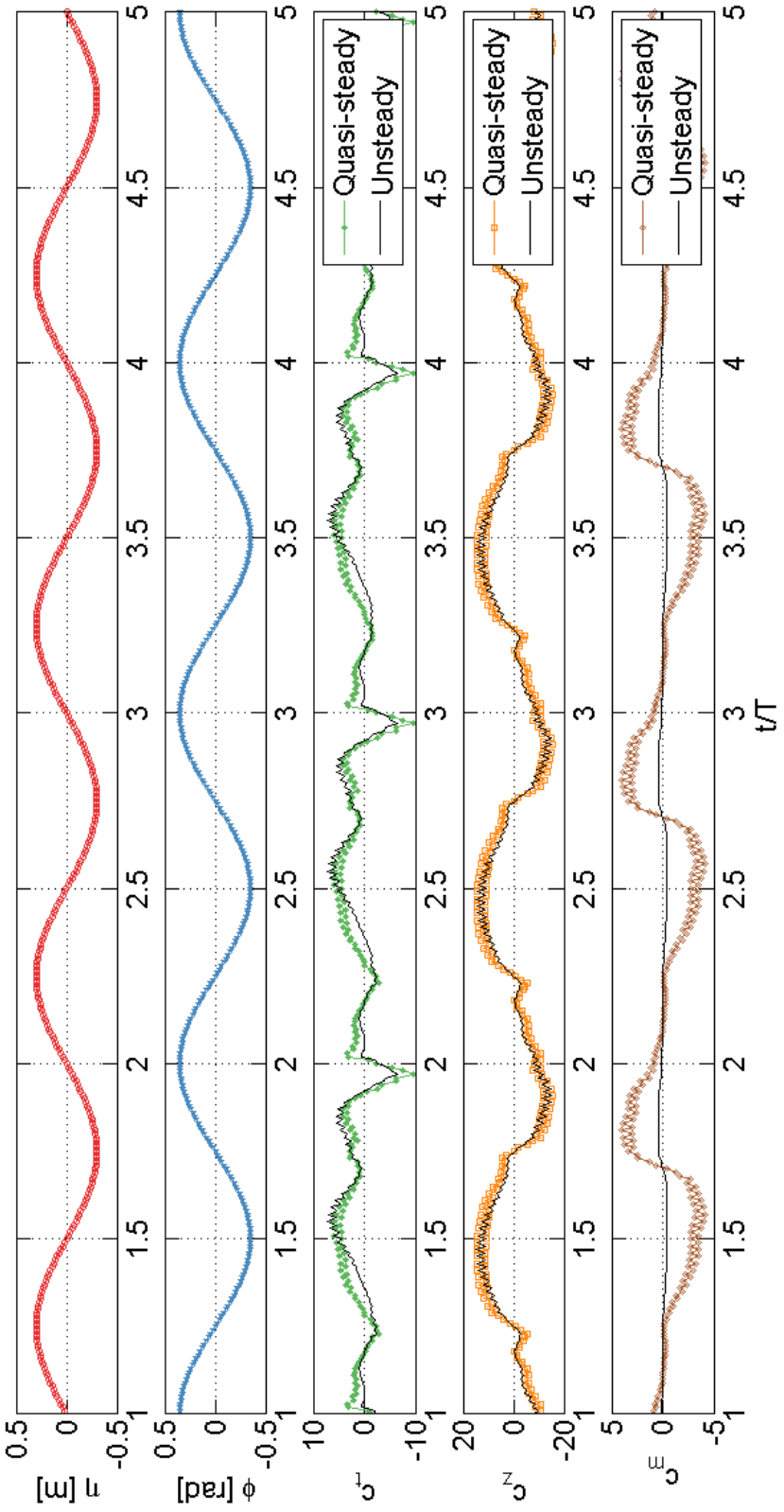

Figure 2.9: Comparison of forces between quasi-steady and unsteady models

Next, the thrust and vertical coefficients are plotted against the dimensionless Strouhal number. Figure 2.10 illustrates the thrust coefficients where two distinct parts of the curves are apparent and have been separated for clarity. In the lower Strouhal range, the thrust initially starts increasing before decreasing slightly for an increasing Strouhal number. The suspected reason for this is the increase in the angle of attack past the stall angle that occurs as the current speed is reduced but still remains large enough to cause the wave phase to oscillate rather than rotate (recall Fig. 2.4). The increasing coefficients result in larger forces in the positive x direction. The thrust coefficients only become positive when the Strouhal number increases to where the current velocity is less than the wave component of velocity, and the combined flow vector undergoes a full rotation. The thrust coefficients also show a strong dependence on wave height, H, and submergence depth, z. The closer the hydrofoil is to the surface, or the larger the wave height, results in a higher thrust coefficient. Although it should be restated that free-surface effects are neglected in the present model and thus lower $\frac{z}{H}$ values may suffer in accuracy.

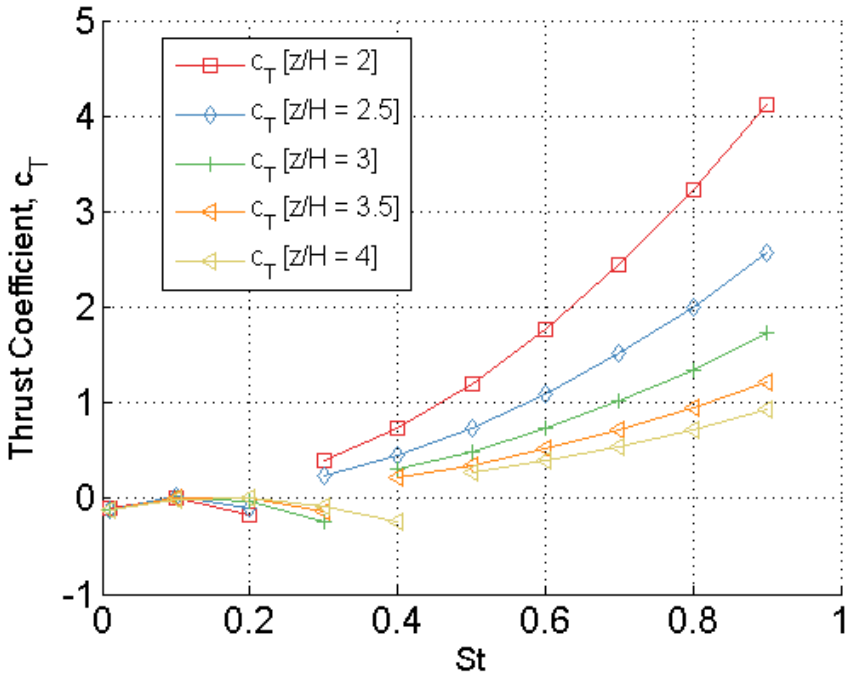

Figure 2.10: Thrust versus. Strouhal number

The vertical coefficient also increases with Strouhal number once the wave phase undergoes full rotation. In the lower Strouhal range, the vertical coefficients remain approximately zero as the wave phase is only oscillating, causing the vertical components to effectively cancel out. Similarly to the thrust coefficients, a lower $\frac{z}{H}$ ratio results in a larger coefficient.

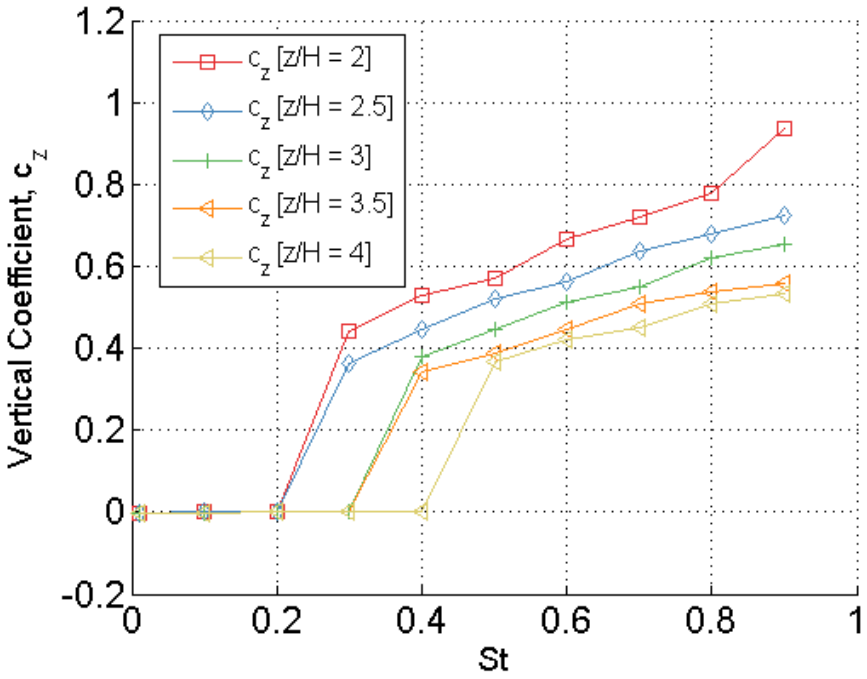

Figure 2.11: Lift versus Strouhal number

2.5 Further Considerations

The phase difference between the foil oscillations and the wave were also investigated. In this case, a $\frac{z}{H}$ ratio of 3 is used. Figure 2.12 shows that a phase lag of 120 degrees provides the most desirable thrust conditions regardless of the Strouhal number, provided the wave phase fully rotates (St $>$ 0.3). When the wave phase oscillates (St $<$ 0.3), a phase lag of 90 degrees is optimal. In most existing oscillating foil research, waves are not used and the hydrofoil is made to oscillate mechanically in heave with prescribed motion. Nevertheless, a 90 degree lag between pitch and heave motion is often found to be the most beneficial [23], [32], [38]. Indeed, when a foil undergoes self-excited oscillations or flutter, the pitch and heave motions are 90 degrees out of phase [50] providing further justification to the selection of phase lag, especially when

the heave degree of freedom is considered. The higher optimal phase lag shown here is likely due to the waves, and their effect on the combined phase angle.

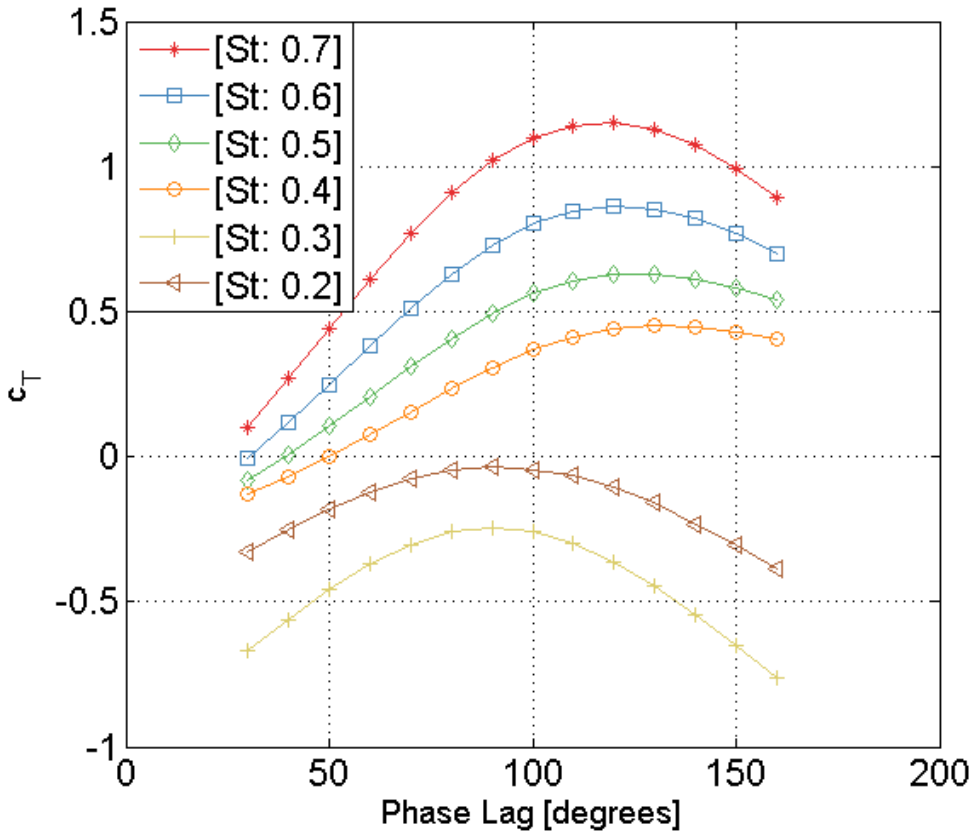

Figure 2.12: Effect of phase lag between the wave and foil oscillations on thrust generated

Lastly, the effect of the foil pitch amplitude is investigated. Figure 2.13 shows that amplitudes between 45 - 50 degrees seem to provide the best results, independent of the $\frac{z}{H}$ ratio. There is also a noticeable drop in thrust visible immediately after the optimal amplitude, suggesting that it may be best to set amplitude in the 20-40 degree range.

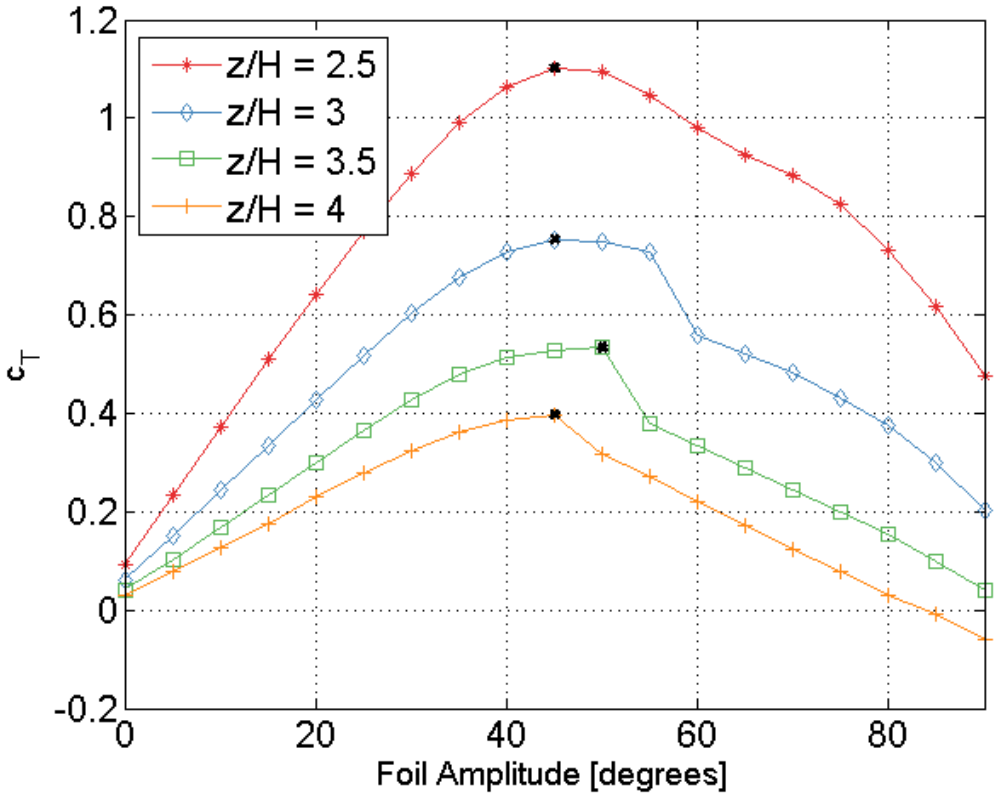

Figure 2.13: Effect of pitch amplitude on thrust generated

The advantage of the presented mathematical models is in providing some preliminary analysis of oscillating foil propulsion and consequently have enabled some system parameters to be selected. Firstly, the Strouhal number needs to be high enough to permit thrust to be generated, meaning the wave/foil frequency and current velocity must be selected carefully. In addition, the phase lag between foil and wave oscillations should be set between 90 and 120 degrees and the pitch amplitude of the hydrofoil should not exceed 50 degrees.

A significant limitation of the presented model is that the models are based on static force coefficients. The unsteady model attempts to account for dynamic effects, however turbulence is still not considered. For further investigation, CFD analysis will be performed where a turbulence model is employed to approximate these effects.

Chapter 3

CFD Simulation

Open Source Field Operation and Manipulation (OpenFOAM) software package [51] is a C++ toolbox suitable for modelling a wide range of fluid flow phenomena. The open source nature of the software means that anyone can develop solvers and utilities to suit a specific need. In this case, one of the existing solvers was used to model the rigid body motion problem of a submerged oscillating hydrofoil in linear gravity waves. Results indicate that positive thrust can be achieved provided the forwrd speed remain below a threshold value. A regression equation is developed and visualization of the wake is presented.

3.1 Problem Description

The problem described in the mathematical model was implemented within OpenFOAM by defining boundaries and applying appropriate boundary conditions (Fig. 3.2).

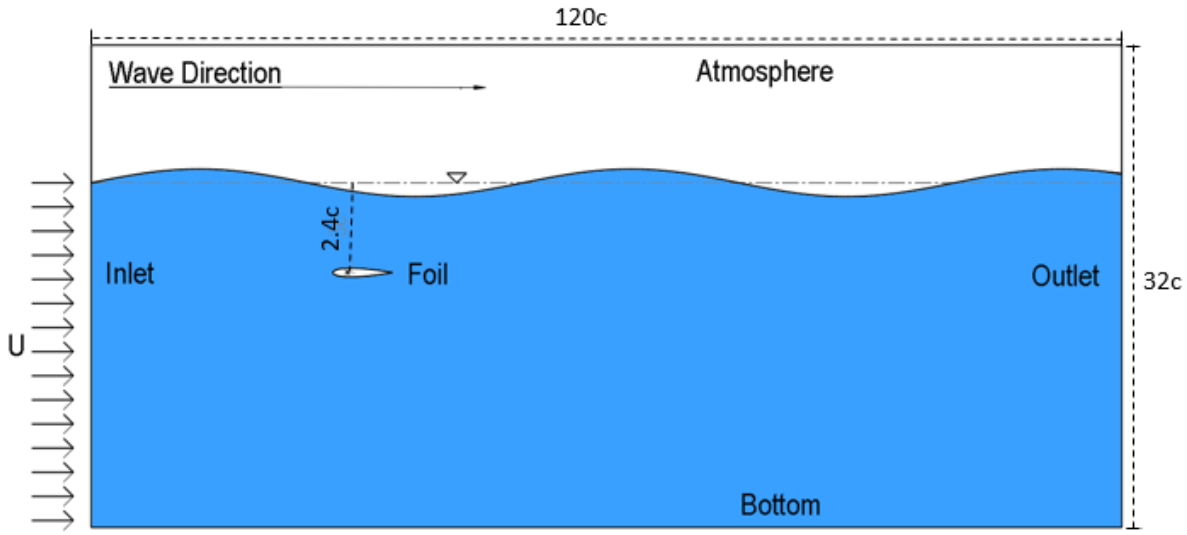

Figure 3.1: Case geometry (Not to scale)

As shown, the incoming linear wave propagates from left to right with the leading edge of the hydrofoil of chord length c facing opposite the propagation direction. The submergence and pivot point location of the foil are equivalent to the mathematical model. The depth of the wave tank was chosen to permit deep water waves ($\frac{h}{\lambda} \geq 0.5$) and the length chosen to help minimize wave reflection off of the outlet boundary back into the computational domain. This is a common challenge of numerical wave tanks and can be handled in several ways, including using relaxation functions, numerical beaches, or increasing the length of the domain. For the purposes of this investigation, the latter was implemented to complement the active relaxation function built-in the solver.

3.2 Model Equations

In this case, the choice of solver affects the form of the classical model equations. Typically, the interfoam, and interDyMFoam solvers are used for two-phase simulation

within OpenFOAM, where the addition of 'DyM'indicates the presence of a dynamic, moving mesh. These solvers are based on the Pressure Implicit with Splitting of Operator (PISO) and Semi-Implicit Method for Pressure-Linked Equations (SIMPLE) solution algorithms, which when combined, are known as the PIMPLE algorithm, more details of which can be found [52]. In this case, the OLAFOAM and OlaDyMFoam solvers [53] (formerly IHFoam), which are heavily based on the interFoam solvers, were selected, as in addition to multiphase flow modelling, they include the ability of generating and absorbing waves at the boundaries.

3.2.1 Mass Conservation

The fluid is modelled incompressible, meaning that the density of the fluid is assumed constant over time. The continuity equation results:

$$\frac{\partial u_i}{\partial x_i} = 0 \tag{3.1}$$

Where:

x_i: (i = 1,2) are the x & z coordinate directions

u_i: (i = 1,2) are the velocity components in the x & z coordinate directions

3.2.2 Momentum Conservation

The presence of two phases and a free-surface results in a modification of the classical Reynolds-averaged Navier-Stokes (RANS) equations to include the effects of a time dependent density and viscosity. OpenFOAM uses the volume of fluid (VoF) method to model the free-surface, meaning that the physical properties at the interface are calculated as a weighted average of the volume fraction of the two fluids. The

assumptions of incompressibility and that both fluids are Newtonian result in the following momentum equation.

$$\underbrace{\frac{\partial \rho u_i}{\partial t}}_{\text{Instationary}} + \underbrace{\frac{\partial \rho u_i u_j}{\partial x_i}}_{\text{Convective}} - \underbrace{\frac{\partial \mu}{\partial x_j}\left(\frac{\partial u_i}{\partial x_j} + \frac{\partial u_j}{\partial x_i}\right)}_{\text{Diffusive}} = \underbrace{-\frac{\partial p}{\partial x_i}}_{\text{Pressure Gradient}} + \underbrace{\rho g}_{\text{Source}} - \underbrace{F_s}_{\text{Surface Tension}} \tag{3.2}$$

Where:

μ: is the dynamic viscosity

p: is the pressure

ρ: is the fluid density

t: is time

g: is gravity

The surface tension F_s, is computed as:

$$F_s = \sigma \kappa(x) n \tag{3.3}$$

Where σ is the surface tension coefficient of 0.07, n is a unit vector normal to the air-water interface calculated by:

$$n = \frac{\nabla \alpha}{|\nabla \alpha|} \tag{3.4}$$

and κ is the curvature of the interface calculated by:

$$\kappa(x) = \nabla n \tag{3.5}$$

3.2.3 Volume of Fluid Method

The VoF method is used within the multiphase solvers in OpenFOAM to track the movement of the interface over time. It operates by computing the volume fraction of each phase that exists in a cell of the computational mesh at every time-step [54]. The transport equation for the volume fraction (α_{vf}) is stated below.

$$\frac{\partial \alpha_{vf}}{\partial t} + \frac{\partial \alpha_{vf} u_i}{\partial x_i} + \frac{\partial \alpha_{vf}(1-\alpha_{vf})U_r}{\partial x_i} = 0 \tag{3.6}$$

Alpha can vary between 0 and 1, where 1 indicates water and 0 represents air. The latter term in the transport equation is necessary to compress the interface. U_r is a velocity field suitable to compress the interface. This term is only operational at the interface due to the $\alpha(1-\alpha)$ term.

Using the volume fraction, the density at the interface can be computed as the weighted average of the densities of the two fluids, or:

$$\rho = \alpha\rho_1 + (1-\alpha)\rho_2 \tag{3.7}$$

A current velocity can be added to the water portion of the computational domain in addition to the presence of waves by specifying the desired velocity in the *waveDict* dictionary. In the air region of the domain, the velocity can be set as desired which, in turn, sets the pressure due to the *fixedFluxPressure* boundary condition which is described in the next section. For the purposes of the present simulations, where no portion of the hydrofoil penetrates the surface, the air velocity was defaulted to atmospheric which resulted in the air region being a region of fixed pressure.

3.3 Boundary Conditions

Boundary conditions must be selected for each of the flow properties in order to accurately represent the physics of the problem. The boundary conditions selected for the surfaces defined in Figure 3.2 are summarized in Table 3.1.

Table 3.1: Boundary Conditions

Surface	U	p_{rgh}	alpha
Inlet	waveVelocity	fixedFluxPressure	waveAlpha
Outlet	waveAbsorption2DVelocity	fixedFluxPressure	zeroGradient
Wing	movingWallVelocity	fixedFluxPressure	zeroGradient
Atmosphere	pressureInletOutletVelocity	totalPressure	inletOutlet
Bottom	slip	fixedFluxPressure	zeroGradient

To generate waves using OLAFOAM, three boundary conditions are needed. Firstly, the velocity (U) file uses the *waveVelocity* boundary condition, which applies a wave velocity for the parameters specified in the *waveDict* file. This is the wave generation dictionary where the target wave conditions can be stipulated, such as the wave theory, wave height and frequency, and also a current velocity. The *waveAlpha* boundary condition is also necessary for the volume fraction or *alpha.water* file, while *fixedFluxPressure* is necessary for the p_{rgh} (dynamic Viscosity) file. The *fixedFluxPressure* boundary condition adjusts the pressure gradient on the surface such that the flux on the boundary is specified by the velocity.

The *pressureInletOutletVelocity* is used for the velocity boundary condition at the top boundary where the pressure is specified. The pressure is specified using the *totalPressure* boundary condition, which prescribes the pressure using a reference

pressure (set to zero in this case) and velocity.

Of the remaining boundary conditions, the *inletOutlet* boundary condition applies a *zeroGradient* condition when the velocity points out of the domain, and is set to zero when pointing into the domain. *zeroGradient* is applied where the flow property is known and assumed to be constant and the *slip* condition is set at the bottom as bottom viscous effects can be considered negligible for deep water waves. Lastly, the *movingWallVelocity* condition specifies the velocity at a moving boundary. This boundary condition corrects the flux due to mesh motion such that no flux moves through the moving wall.

The *dynamicMeshDict* dictionary file specifies the solid body motion parameters of the hydrofoil. The foil was made to oscillate sinusoidally as in the math model. The *oscillatingRotatingMotion* function was employed, which requires a rotating cell zone be defined. The *controlDict*, as well as the *waveDict*, U, and *dynamicMeshDict* scripts are included in Appendix B for reference.

3.4 Discretization

Discretization is generally split into two sections; the first is approximating the partial differential model equations presented by algebraic equations, and the second is developing an appropriate computational domain, or mesh, by dividing the domain into smaller cells or regions. This is a fundamental component of a CFD model and is further explained in the following paragraphs.

3.4.1 Discretization of Equations

The model equations presented must be approximated by algebraic equations in order to be solved numerically. This is done using the finite volume method. First, the volume integral of all equation terms is taken, then the rule of Gauss is applied on the spatial terms (i.e. convective and diffusive terms) resulting in surface integrals. The surface integral then employ a Taylor series with the midpoint rule to achieve an algebraic approximation that is second order exact. The remaining volume integrals (the instationary and pressure gradient terms) are also approximated by the midpoint rule. These approximations introduce numerical errors to the equation. The numerical schemes used to solve the algebraic approximations must be specified in OpenFOAM in the *fvSchemes* file. Further descriptions of the numerical schemes in OpenFOAM can be seen in [55]. The schemes chosen are shown in Table 3.2.

Table 3.2: Discretization Schemes

Term	Numerical Scheme	Notes
Instationary	Euler	First order implicit
Convective - U	Gauss limited linear V1	Vector limiting scheme
Convective - α	VanLeer	Limiting scheme
Convective - α	interfaceCompression	Interface sharpening [Weller]
Pressure Gradient	Gauss linear	2nd order, unbounded
Diffusive	Gauss linear corrected	Non-orthogonal correction

3.4.2 Mesh

The development of the background mesh for the numerical wave tank was accomplished using OpenFOAM utility, blockMesh. The mesh was first separated into

multiple blocks to facilitate cell grading such that the cell distribution at the interface and in the neighbourhood of the hydrofoil is sufficient to capture the flow phenomena. A visualization of the mesh grading and blocking is shown in Figure 3.2.

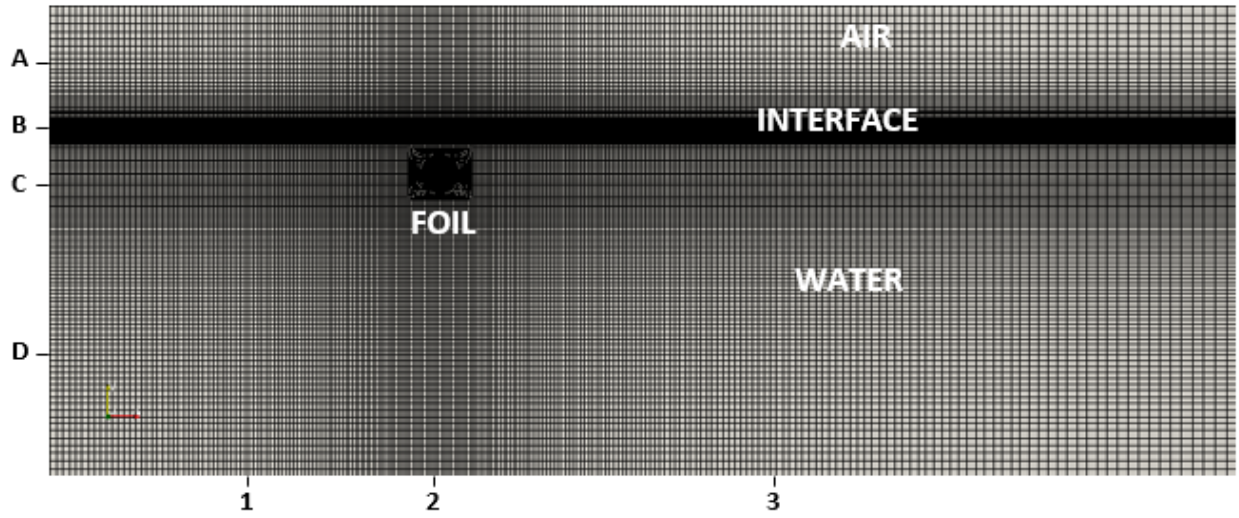

Figure 3.2: Visualization of mesh grading. The letters and numbers represent the blocks.

To minimize the computational requirement, many of the blocks were graded to avoid providing a high cell density in less important regions, such as the deeper water zone and the atmosphere. The final grading and cell sizes used are stated in Table 3.3.

Table 3.3: Background Mesh Characteristics

Block	Graded	Avg. X size [m]	Avg. Y size [m]
A1	Yes	0.09	0.07
A2	Yes	0.05	0.07
A3	Yes	1.175	0.07
B1	Yes	0.09	0.015
B2	Yes	0.05	0.015
B3	Yes	1.175	0.015
C1	No	0.09	0.05
C2	Yes	0.05	0.05
C3	Yes	1.175	0.05
D1	Yes	0.09	0.1
D2	Yes	0.05	0.1
D3	Yes	1.175	0.1

With the background mesh created, the foil shape was inserted into the mesh using the *snappyHexMesh* (SHM) utility. This utility takes a stereolithography file (.stl) and inserts it into the specified location within the base mesh. In principle, SHM refines the cells as specified in *snappyHexMeshDict* in order to form the mesh around the foil. Since SHM creates a 3D mesh, the *extrudeMesh* utility was used to extrude a face one cell deep to create a 2D mesh.

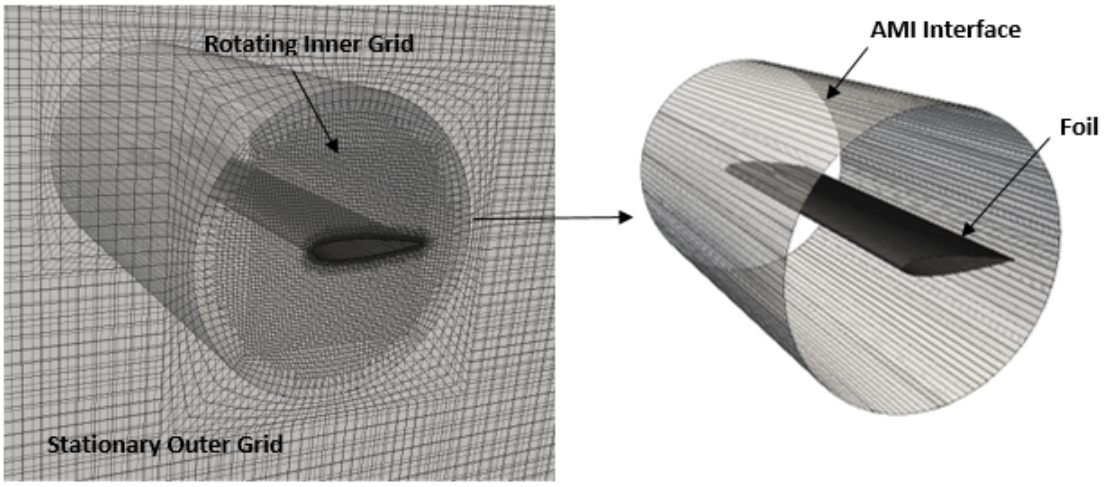

Figure 3.3: Rotating portion of mesh

To permit the rotational motion required without severely reducing mesh quality, an arbitrary mesh interface (AMI) was employed around the hydrofoil (Fig. 3.3). This allows the inner, rotor portion of the mesh to rotate as desired, while the outer, stator portion of the mesh remains stationary. Without this feature, only small pitch amplitudes could be realized without causing the simulation to diverge. The AMI requires two separate meshes which are merged together using the *mergeMeshes* utility and coupled at the boundary using the *cyclicAMI* boundary condition. This procedure is useful for rotating geometries and has been proven effective for marine and marine energy related simulations [56], [57] .

In order to prevent the reflection of wave energy at boundaries, the OLAFOAM solver provides an absorption condition at both the inlet and the outlet. The boundary condition at the inlet allows incident waves to flow outwards while not affecting the target wave generation. The active wave absorption at the outlet allows wave energy to flow out and maintains water level without needing to further enlarge the domain.

By setting the velocity field boundary condition to *2DWaveAbsorptionVelocity*, the boundary generates a velocity equal and opposite to the incident (reflected) velocity. This is calculated using the reflected free-surface height η_R, which is the difference between the measured and target surface elevation. The reflected velocity calulation is shown in Equation 3.8 below. For further information see [53]

$$U_c = -\sqrt{\frac{g}{h}}\eta_R \tag{3.8}$$

3.4.3 Grid Refinement

As the mesh is refined, the solution should converge to a single value, and become less sensitive to grid spacing. Therefore it is important to optimize the model and capture the desired phenomena in a timely manner. To ensure the spatial domain is accurately capturing the flow phenomena, three mesh sizes were tested and the forces generated by an oscillating foil in waves were compared. Since this is a dynamic case, the forces of the different meshes were compared over several wavelengths as the wave fully develops. The results are shown in Figures 3.4 & 3.5 below

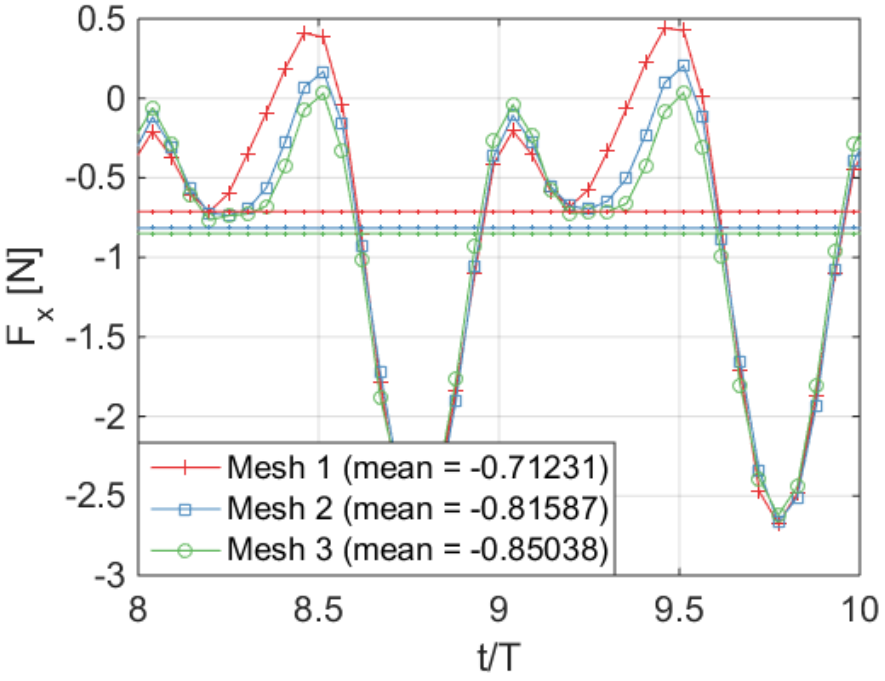

Figure 3.4: Horizontal forces

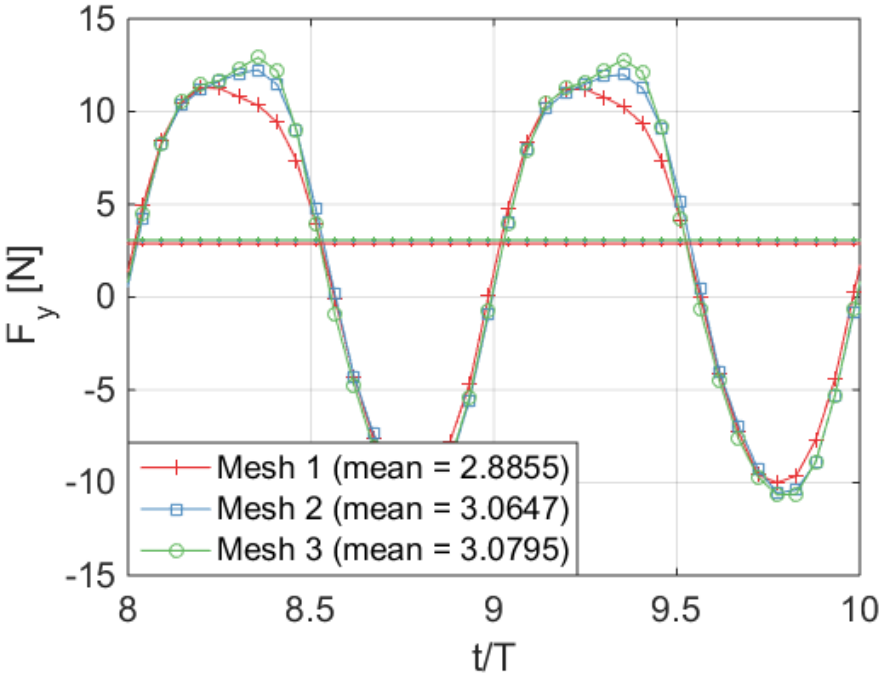

Figure 3.5: Vertical forces

It can be seen that Mesh 1 does not accurately capture the extreme values at the peaks and troughs of the curve. Mesh 2 & Mesh 3 agree much more closely in these regions. The three mesh conditions, force coefficient values and computational time requirement are stated in Table 3.4.

Table 3.4: Mesh Convergence

Mesh	No. of Cells	$c_D\%error$	$c_L\%error$	CPU time [s]
Mesh 1	33793	-	-	1157
Mesh 2	85245	14.5%	6.2%	3172
Mesh 3	131137	4.2%	0.4%	15724

As shown, the finest mesh requires a significantly larger time for processing and results in a relatively small change in coefficient value (less than 5%). Consequently, Mesh 2 was selected for the simulation.

3.5 Turbulence Model

Concerning turbulence modelling, the mesh in the vicinity of the foil itself must be sized to accurately capture the turbulent flow effects. The Y+ value is used to help determine the appropriate cell size of those cells directly on the wall of the body in question, in order to capture boundary layer effects. To avoid having to resolve the viscous sub-layer, the size of the cells on the body is selected such that wall functions can be used. This is a main difference between RANS and direct numerical simulation (DNS) and significantly reduces computational time. The simulation characteristics of the mesh can be seen in Table 3.5, and the resulting boundary layer in Figure 3.6

Table 3.5: Mesh Properties

Element	Value
No. of Cells	85245
yPlus	20
Max non-orthogonality	54.0701
Maximum Skewness	1.45668

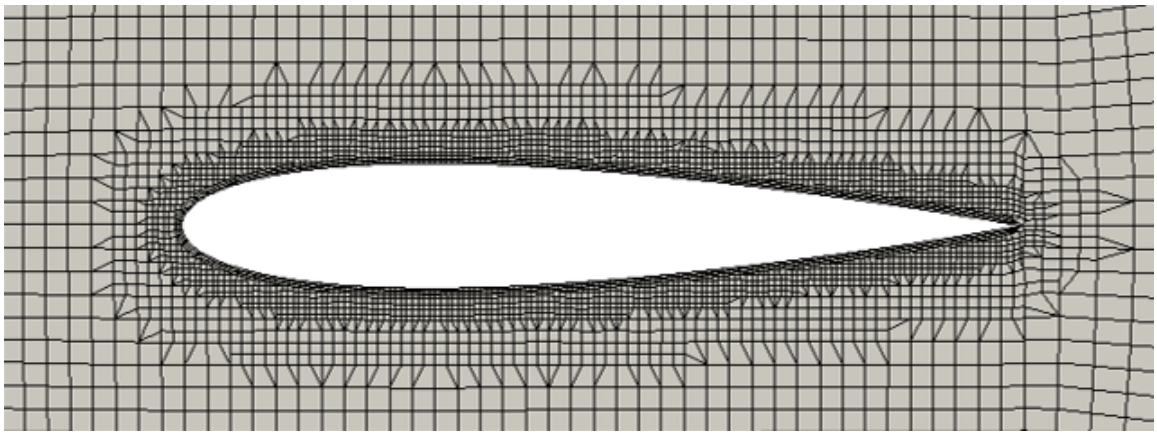

Figure 3.6: Boundary layer

After selecting the appropriate wall functions, a turbulence model is then used to approximate the Reynolds stress tensor within the RANS equations. The Reynolds stress' represent the turbulent phenomena. The Reynolds stress tensor is not included in the model equations (See Section 3.2) because it introduces too many unknowns within the system of equations without adding any new information. This is sometimes referred to as the closure problem of turbulence. As a result, turbulence models have been developed. The $\kappa - \epsilon$ SST turbulence model contains two transport equations and combines the $\kappa - \epsilon$ and $\kappa - \omega$ models into one. It was selected for this simulation due to its behaviour in simulationg large pressure gradients and separating flow [58]. The turbulent model coefficients are stated in Table 3.6 below:

Table 3.6: $\kappa - \omega$ SST model coefficients

Coefficient	Value
σ_{k1}	0.85
σ_{k2}	1
$\sigma_{\omega 1}$	0.5
$\sigma_{\omega 2}$	0.856
γ_1	0.566
γ_2	0.44
β_1	0.075
β_2	0.0828
β^*	0.09
a_1	0.31
b_1	1.0
c_1	10
$F3$	false

3.6 Preliminary Results

3.6.1 Design of Experiments

Design of Experiments (DOE) methods were used for this computer simulation using Design-Expert software [59] in order to learn what conditions result in positive thrust development for an oscillating foil in linear ocean waves. DOE provides a systematic means of determining relationships between factors affecting a process, and their effect on the response. It is based on the three pillars of experimental design, namely, randomization, blocking, and repetition. DOE methods allow more data to be extracted from experimental results with less effort, when compared to the classical one factor at a time (OFAT) experiments [60]. For a computer experiment, Latin

hypercube sampling (LHS) or uniform design (UD) are common experimental designs, with the latter being chosen in this case. UD is known as a 'space-filling' design, useful for experiments where there is a large experimental domain to be explored [61]. The UD was first proposed by Fang [62], and Wang and Fang [63] and positions design points uniformly within the experimental domain. The basis of the uniform design is the Koksma-Hlawka inequality which provides an upper error limit of the design which is the product of the discrepancy (the measure of uniformity) and the variation of the results. In this case, a centered L_2 (CD), level 3 uniform design was selected, resulting in a more time feasible run requirement of 21 (a classic factorial design would have resulted in a run requirement of 81) and allowing up to a quadratic model to be fit. The selected centered L_2 (CD) discrepancy satisfies many criteria and is commonly used for design tables with good uniformity [64]. In this case, four factors are varied to discover which are significant to positive thrust development. The factors tested are wave height, wave frequency, hydrofoil pitch angle, and forward speed, with each factor having three levels. Assumptions of normality, independence, and constant variance were met by both regression models, as confirmed by the residual plots. The run list, parameters, and responses are listed in Table 3.7 below.

Table 3.7: Uniform Design Run List

Run No.	Wave Height H [cm]	Wave Freq. f [Hz]	Pitch Amp. ϕ [degrees]	Flow Vel. U [m/s]	R1:F_x [N]	R2:F_z [N]
1	3	0.5	0.4	30	3.59	4.70
2	1	0.4	0.2	10	-0.06	2.26
3	1	0.4	0.4	20	-1.645	3.82
4	5	0.4	0.4	20	-1.44	9.05
5	5	0.5	0.2	30	1.95	7.57
6	5	0.3	0	20	1.09	3.08
7	1	0.4	0	30	3.61	0.86
8	5	0.4	0	10	0.62	5.10
9	1	0.3	0.2	10	-0.14	2.32
10	3	0.5	0.4	10	-0.51	3.19
11	1	0.3	0.4	20	-1.94	3.15
12	5	0.5	0.5	10	0.54	3.70
13	3	0.3	0.4	10	-0.70	3.30
14	1	0.5	0.2	30	0.99	3.61
15	3	0.5	0	20	2.42	1.71
16	5	0.3	0.2	20	0.17	4.74
17	3	0.4	0	10	0.46	4.14
18	3	0.3	0	30	2.08	1.84
19	3	0.3	0.2	30	-0.53	4.80
20	1	0.5	0	20	2.07	1.30
21	5	0.4	0.4	30	-4.46	13.82

The control variables and their subsequent ranges are stated in Table 3.8.

Table 3.8: Control Variables and Subsequent Ranges

Factor	Description	Low (-1)	High (+1)
A	Wave Height, H [cm]	1	5
B	Wave Frequency, f [Hz]	0.3	0.5
C	Foil Amplitude, ϕ [Deg]	10	30
D	Forward Speed, [m/s]	0	0.4
R1	Horizontal Force, F_x		
R2	Vertical Force, F_z		

Note that since the wave heights tested are only a small fraction of the total chord length, the wave driven particles move very minimally making it unlikely that wave height will be a significant control variable.

3.6.1.1 Thrust Force

For the analysis of the uniform design results, a stepwise regression approach was used with a significance level of 5%. The Pareto plot in Figure 3.7 shows the respective contributions of factors and factor interactions to the thrust force.

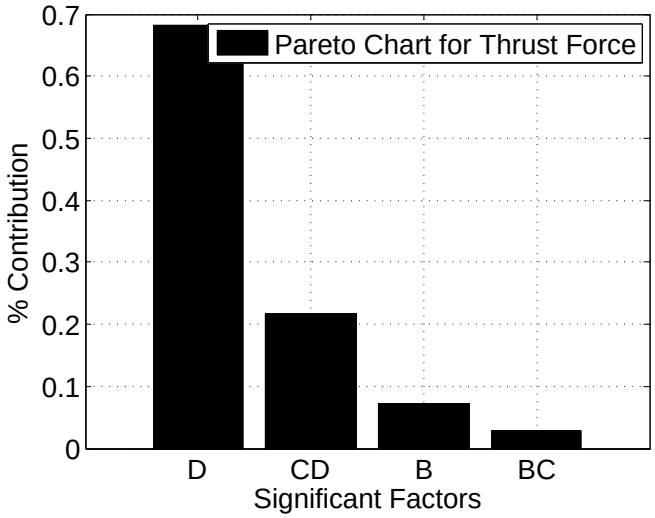

Figure 3.7: Pareto chart for the thrust force in the uniform design analysis

The forward speed factor (D) is by far the most significant factor accounting for almost 70% of the thrust effect, and also results in a significant two-factor interaction (2FI) when combined with the hydrofoil amplitude (CD). The remainder of the thrust effects are caused by the wave frequency (B) as well as its interaction with the hydrofoil amplitude (BC). Noticeably absent from the figure is the wave height, which was found to have no significant effect on thrust development within the range of wave heights tested. It is expected however, that testing a larger range would increase the thrust development. The resulting design equation provides more input into what conditions produce positive thrust. The coded regression equation stated below (Eq. 3.9) resulted in an adjusted R^2 value of 0.95 and a predicted R^2 value of 0.91. A coded regression equation converts the three factor levels to a high (+1), middle (0), and low (-1) value and is useful in identifying the relative impacts of individual factors on the response. Adjusted R^2 is taken rather than the classic R^2 as it only increases when the correct factors are included in the analysis, unlike the classic R^2. The actual versus predicted plot can be seen in Figure 3.8.

$$(F_x + 4.91)^{1.52} = 12.23 + 2.02f + 0.76\phi - 6.26U + 1.62f\phi - 4.85\phi U \tag{3.9}$$

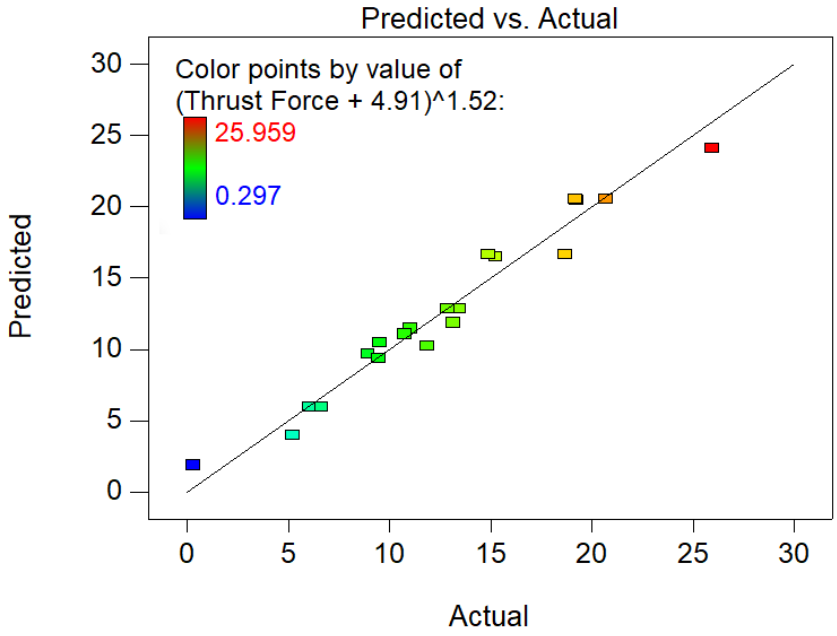

Figure 3.8: Actual versus predicted values for the thrust forces in the uniform design analysis

Figure 3.9 shows an interaction surface between hydrofoil amplitude and forward speed. In this circumstance, the wave height and wave frequency are set to their corresponding mid-range values of 3 cm and 0.4 Hz cm respectively.

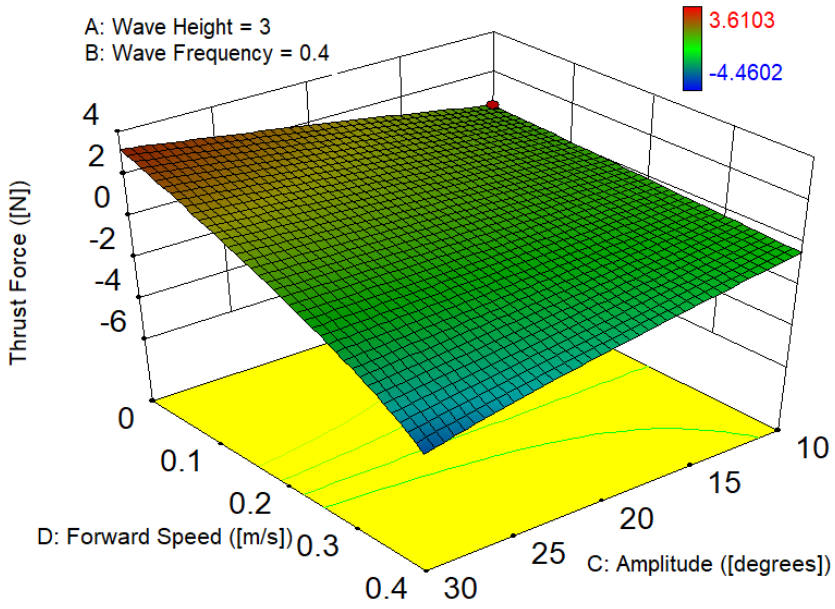

Figure 3.9: Three-dimensional surface showing the interaction between the hydrofoil amplitude and forward speed

It can be seen that the most beneficial conditions are lower speeds with larger pitch amplitudes, and the worst conditions are higher speeds with larger pitch amplitudes. The thrust development occurs mainly when the forward speed is less than approximately 0.2 m/s. This is confirmed when looking at the interaction plot between wave frequency and pitch amplitude shown in Figure 3.10, where the forward speed is held constant at 0.2 m/s. Here, it is shown that positive thrust occurs only as the wave frequency approaches 0.4 Hz and higher. A frequency of 0.3 Hz results only in negative thrust, and varying the wave height was found to have no effect.

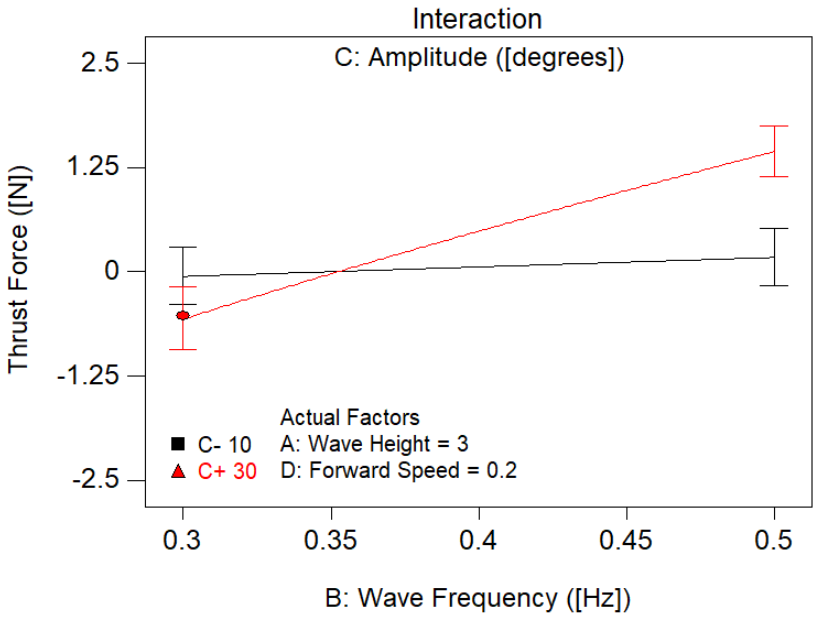

Figure 3.10: Interaction diagram between the wave frequency and the hydrofoil amplitude (U = 0.2 m/s; H = 3 cm)

Figure 3.11 shows that a larger foil amplitude becomes a negative contributor to thrust as the forward speed increases, and appears to become non-linear as the amplitude increases. A possible explanation is that the increased drag caused by a larger foil area incident to the flow overpowers the momentum generated by the foil.

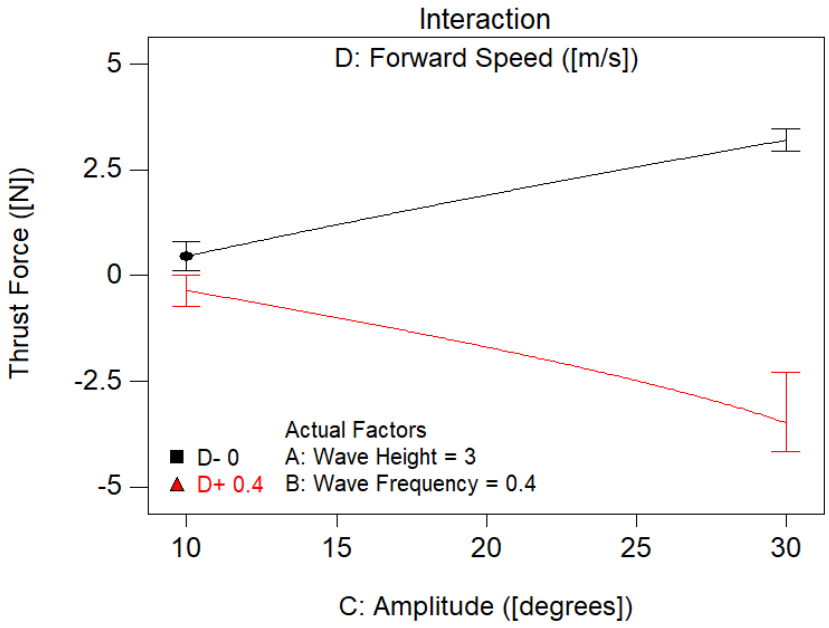

Figure 3.11: Interaction diagram showing the effect of hydrofoil amplitude and forward speed on thrust

3.6.1.2 Vertical Force

Concerning the vertical forces, the Pareto plot in Figure 3.12 shows the respective contributions of factors and factor interactions to the response.

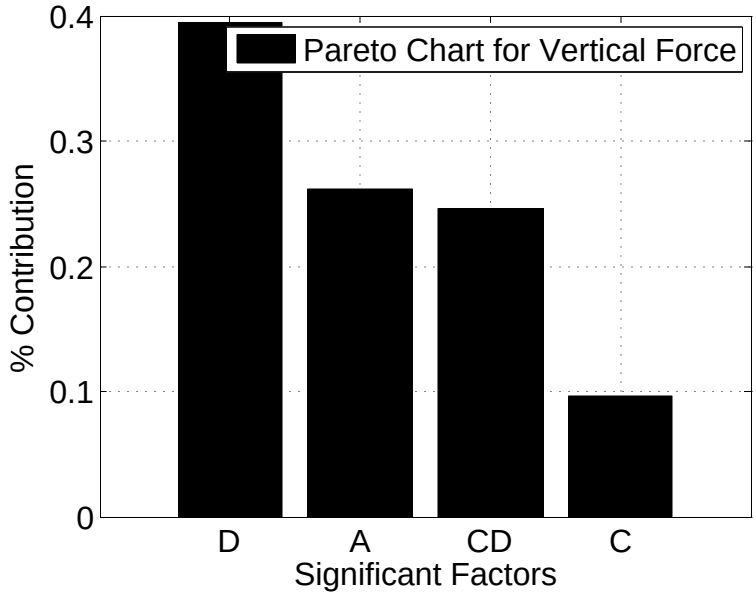

Figure 3.12: Pareto chart for the vertical force in the uniform design model

Similar to the horizontal forces, the forward speed and subsequent interaction with the hydrofoil amplitude are significant factors for the vertical forces. In this circumstance, however, the wave height also becomes significant along with the hydrofoil amplitude. The coded regression equation shown below indicates that all factors contribute to positive vertical force development.

$$\sqrt{F_y} = 2.00 + 0.38H + 0.23\phi + 0.46U + 0.53\phi U \tag{3.10}$$

Equation 3.10 results in adjusted R^2 and predicted R^2 values of 0.93 and 0.90 respectively. The actual versus predicted plot is shown in Figure 3.13 below:

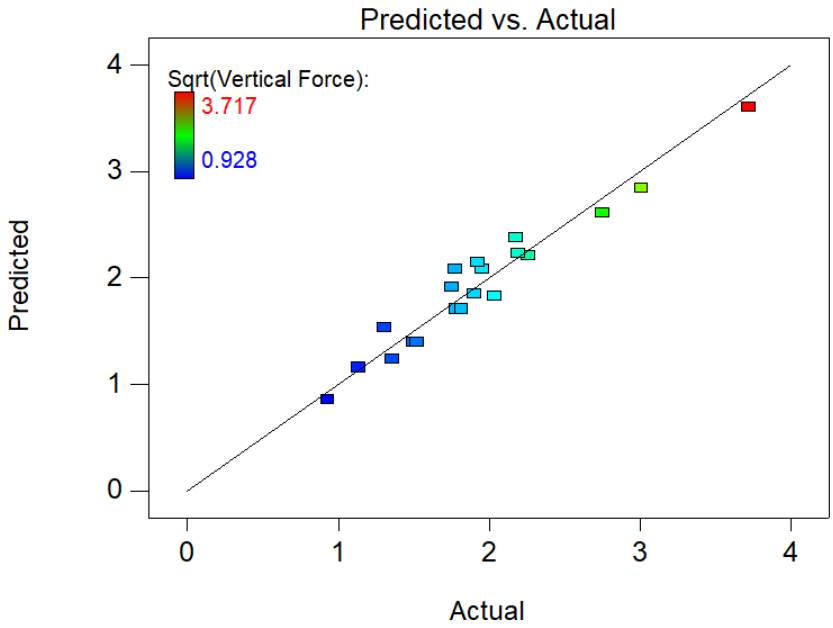

Figure 3.13: Actual versus predicted values for the vertical force in the uniform design analysis

The interaction between the hydrofoil amplitude and the forward speed can be seen in Figure 3.14.

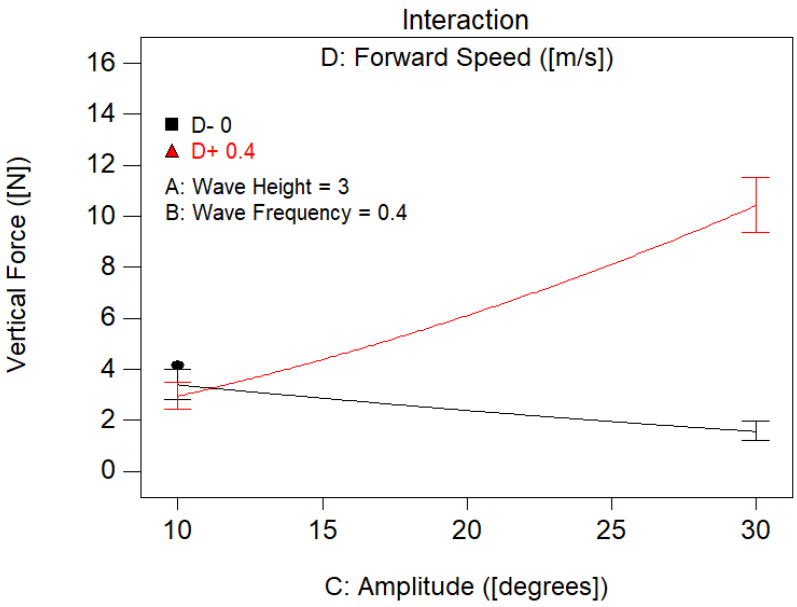

Figure 3.14: Interaction diagram between the hydrofoil pitch amplitude and the forward speed (f = 0.4 Hz; H = 3 cm)

It is observed that increasing pitch amplitude with a zero forward speed causes a slight reduction to the vertical force, although it still remains positive within the ranges tested. As forward speed is increased, the vertical force increases with increasing pitch amplitude at a higher rate.

For the moment response, the uniform design analysis recommends that no model be fit, and the mean value be used as a predictor since the moment values vary only slightly about zero.

3.6.2 Comparison with Mathematical Model

The goal of the present comparison is to determine if similar trends are present between the mathematical and numerical models. The mathematical model was based on static

force and moment coefficients, an estimation of wave and added mass effects, and the assumption that free-surface effects are negligible. As such, a sufficient representation of the system is not expected. Figure 3.15 shows a comparison of the wave profiles for three forward speeds (0 m/s, 0.5 m/s, & 1 m/s). Figure 3.15a indicates that the foil oscillations themselves do not cause any significant deviation from the theoretical wave profile. However, this is not the case when the forward speed is increased. Figures 3.15b & 3.15c show the wave profile results with forward speeds of 0.5 m/s and 1 m/s respectively, where deviations start to become apparent. In 3.15b, a slight shift of the wave upward can be seen as well as an elongation of the wave crest. In 3.15c, the OpenFOAM wave no longer shares the same wave particle position at any point during the wave. These free surface effects are likely to cause changes in the resulting forces, and were not accounted for in the mathematical model.

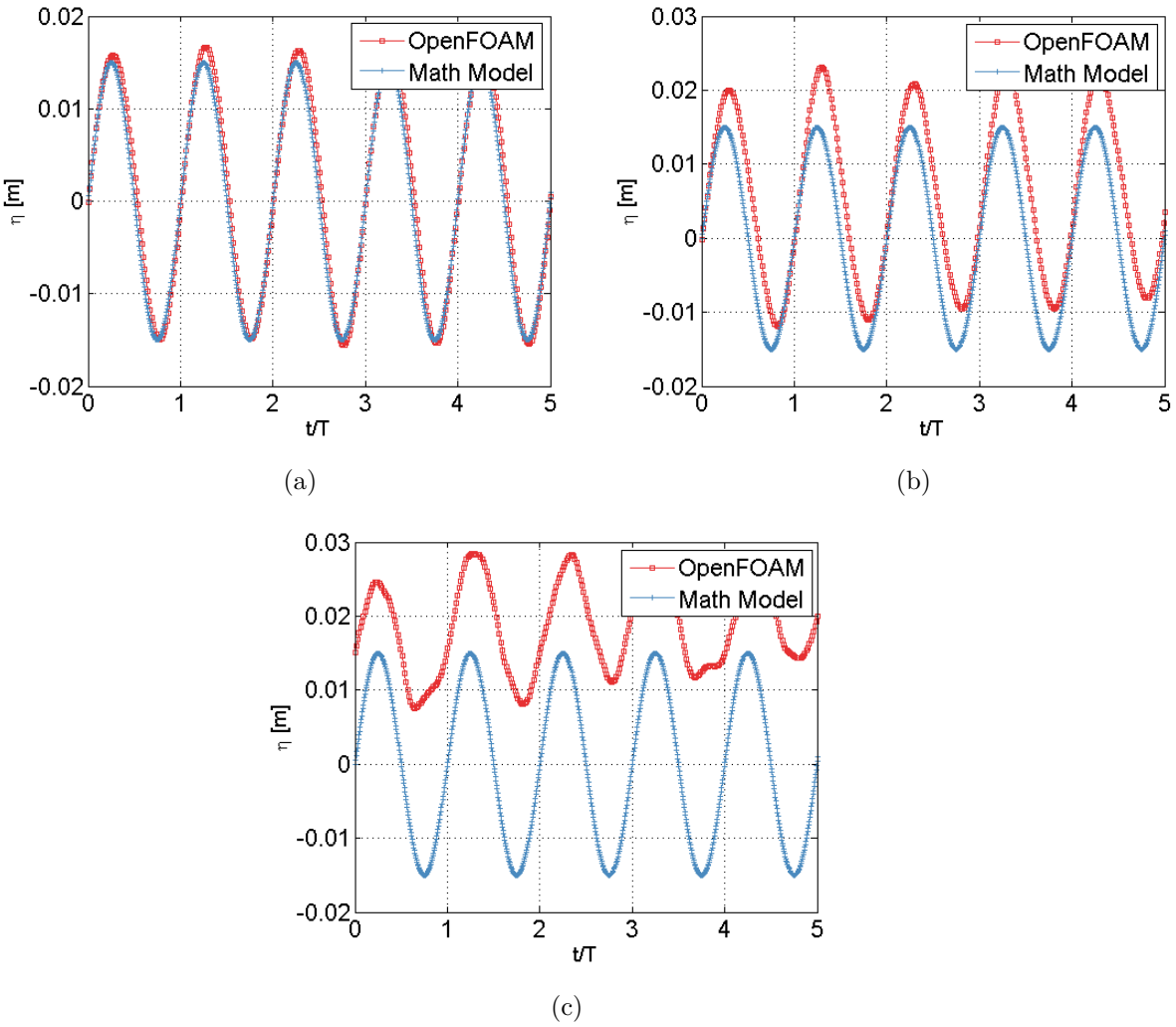

Figure 3.15: Wave profile comparison with a = 5 cm, f = 0.3 Hz, $\phi = 30°$: (a) U = 0 m/s (b) U = 0.5 m/s (c) U = 1 m/s

Next, as performed with the math model, the average resultant forces are compared for a fixed versus oscillating hydrofoil. The first scenario (Fig. 3.16a) indicates an increase in thrust with an oscillating foil at zero forward speed, as was the case in the mathematical model. When the forward speed is increased to 0.5 m/s however, the drag takes over, and is represented as negative thrust in Figure 3.16b. The most plausible explanation for this is that the momentum generated by the oscillations

are not sufficient to counteract the added drag due to more foil area incident to the flow. A possible solution could be increasing the Strouhal number, by either reducing the forward speed, increasing foil pitch amplitude, or increasing oscillation frequency. Aside from the oscillating force being 3-4 times larger than the fixed case, it can also distinctly be seen that the oscillating case is also twice as frequent. This is due to the effect that the foil oscillations have on the angle of attack.

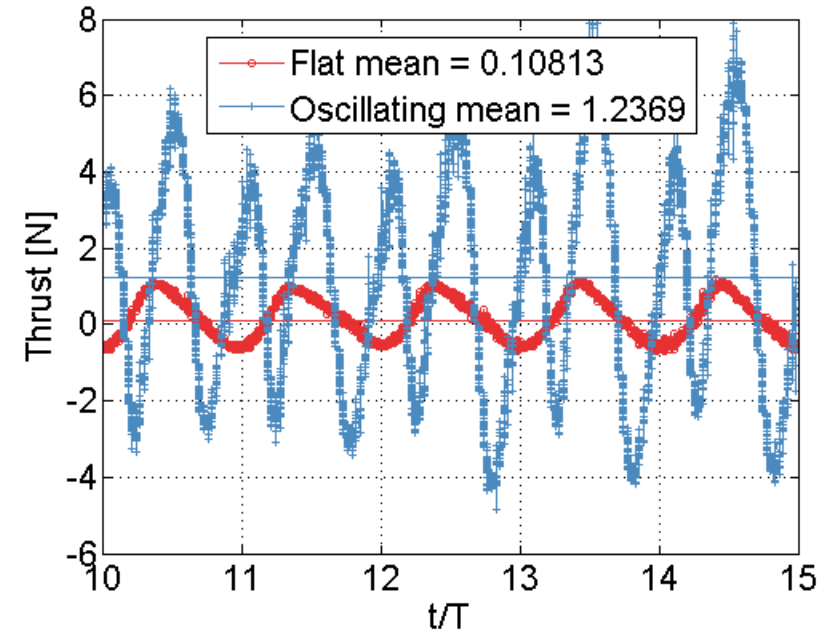

(a)

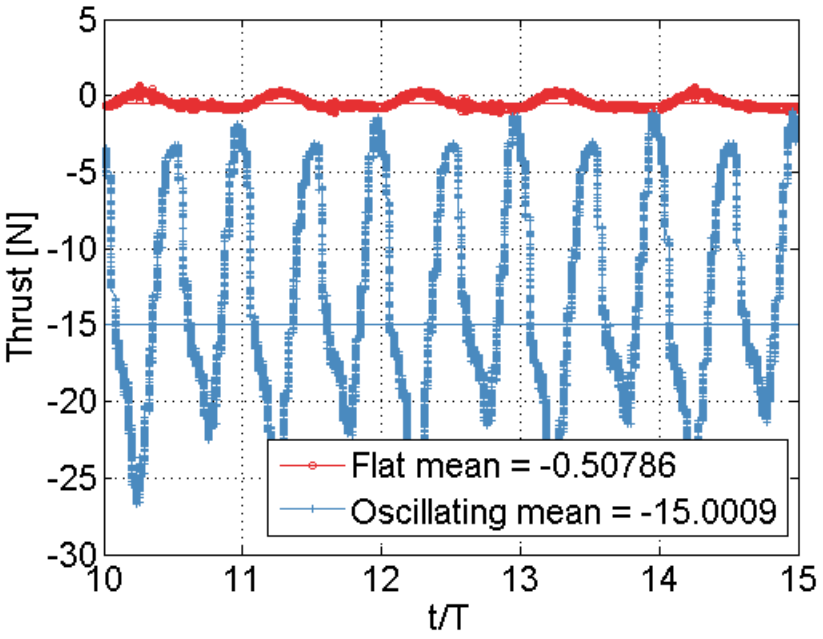

(b)

Figure 3.16: Flat vs. oscillating hydrofoil: (a) U = 0 m/s (b) = 0.5 m/s

A comparison of the thrust forces developed between the models shows that the OpenFOAM results have a lag of approximately $\frac{1}{4}$ of a wavelength (although this changes depending on the wave), which is due to the wave needing time to fully develop. While the average values are relatively similar, it can be seen that the math model underestimates the peak forces, an element that becomes even more pronounced when comparing the vertical forces and moments (not shown). Due to the several shortcomings of the mathematical model, the OpenFOAM values alone will be compared to experimental results.

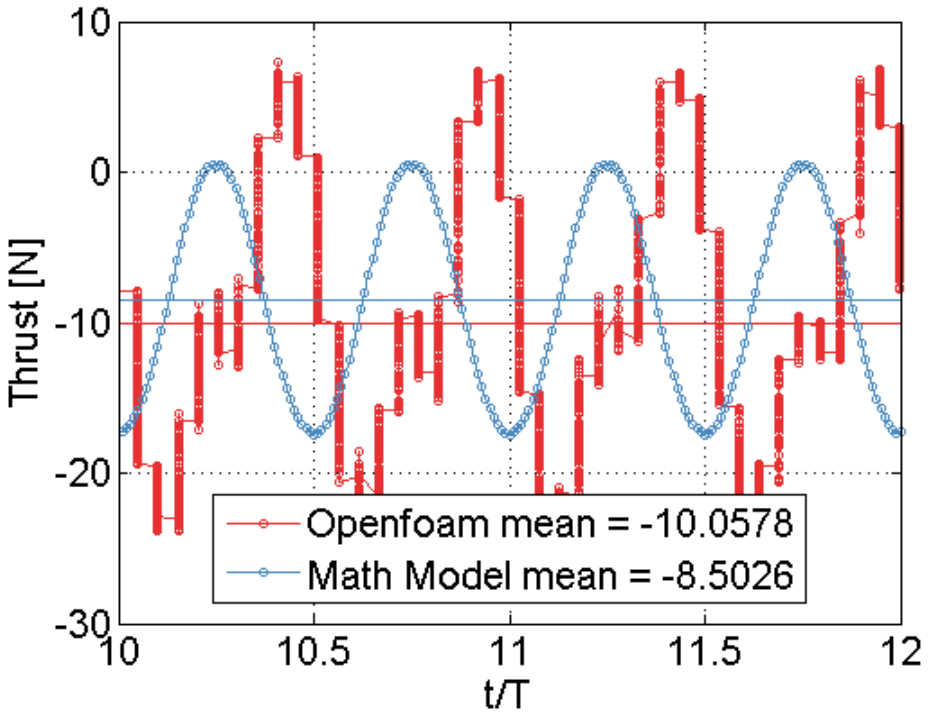

Figure 3.17: Simulation vs. mathematical model (a = 5 cm, U = 0.5 m/s, $\phi = 30°$)

3.6.3 Visualization

Paraview, the post-processing software packaged with OpenFOAM allows for some visualization of the flow around foil. Figure 3.18 shows the vorticity field surrounding

the hydrofoil at every $\frac{1}{4}$ wavelength for a test case with a 5 cm wave height, a wave frequency of 0.3 Hz, a hydrofoil pitch amplitude of 30°, and a forward speed of 0.5 m/s.

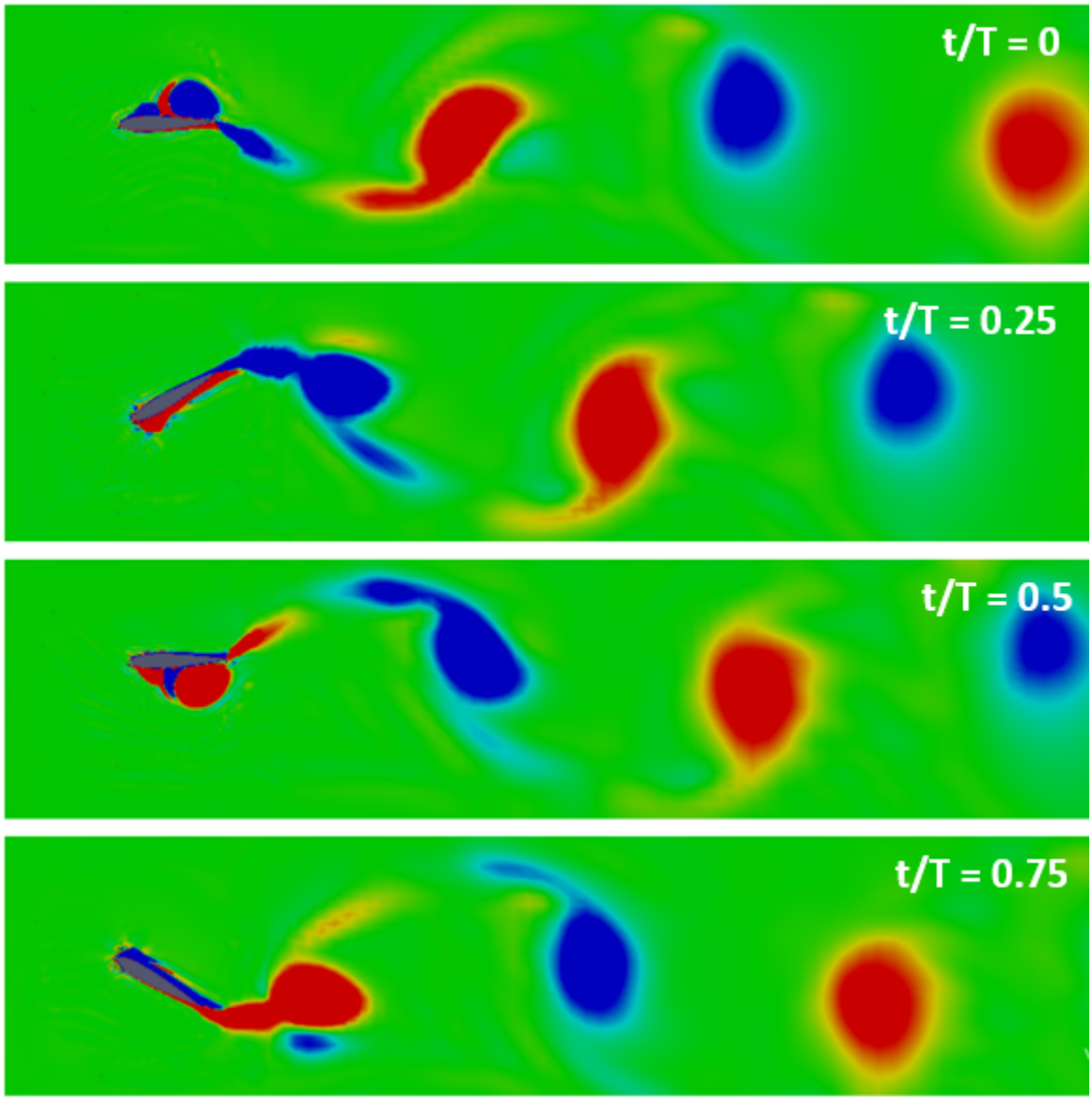

Figure 3.18: Vorticity field (a = 5 cm, f = 0.3 Hz, ϕ = 30°, U = 0.5 m/s)

As shown, the wake pattern appears similar to a classic von Kármán street. Regions of positive vorticity (blue) and negative vorticity (red) separate from the hydrofoil

around the point that it reaches maximum pitch amplitude. The blobs of negative vorticity are situated in the upper portion of the wake, and positive vorticity on the lower. The two shed vortices per cycle continue downstream and slowly diminish in magnitude. Considering the forces developed throughout the full oscillation, Figure 3.19 shows that maximum drag is also occurring when the pitch amplitudes are at a maximum value ($\frac{t}{T}$ = 0.25 & 0.75 respectively).

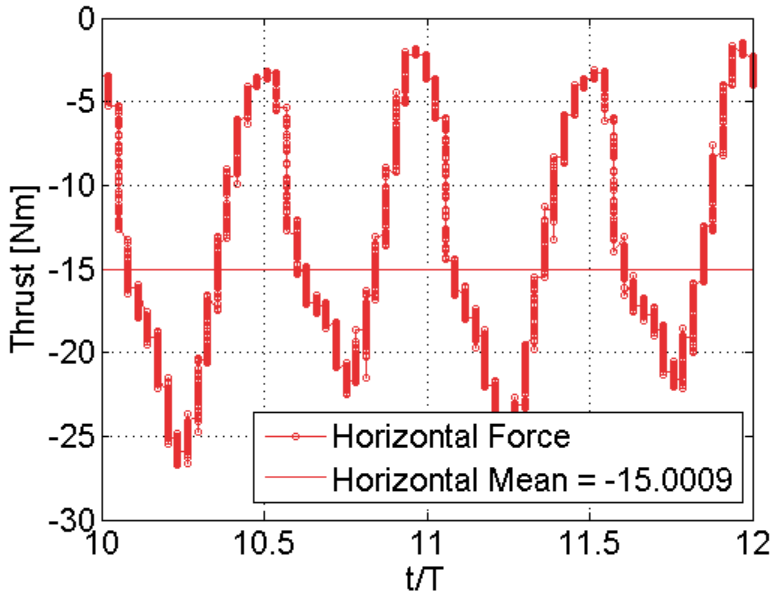

Figure 3.19: Test case forces (a = 5 cm, f = 0.3 Hz, $\phi = 30°$, U = 0.5 m/s)

It is likely that the Strouhal number for this case is slightly too small for thrust to be generated. For comparison, the same case was rerun with a forward speed of only 0.1 m/s, which resulted in a Strouhal number of 0.65. The results can be seen in the Figures 3.20 & 3.21 below.

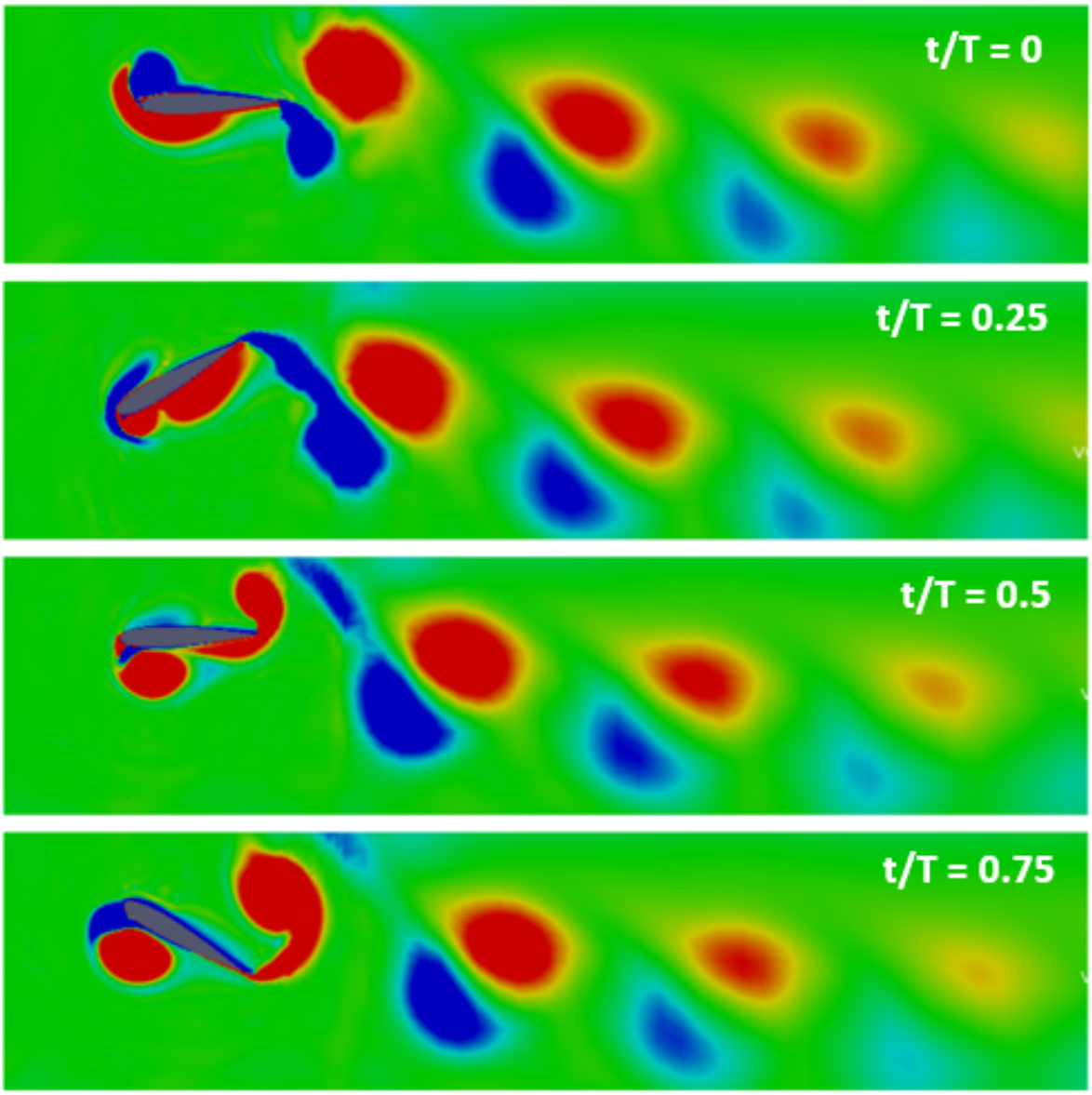

Figure 3.20: Vorticity field (a = 5 cm, f = 0.3 Hz, $\phi = 30°$, U = 0.1 m/s)

In comparing the two wake patterns, some distinct differences can be noted. Perhaps the most apparent is how the shed vortices angle slightly downward in Figure 3.20, as opposed to the relatively straight line seen in Figure 3.18. This deflection is likely due to the change in the vortex arrangement in the wake. The positive and negative vortices appear to be shed in pairs for the higher Strouhal case, which is not the case

in Figure 3.18. Indicative of a reverse von Kármán street, the regions of negative vorticity are on the bottom while positive vorticity is on the top. Indeed, in comparing the von Kármán and reverse von Kármán vortices generated by Schnipper [65] and Godoy-Diana [66], similarities to the present case can be noted.

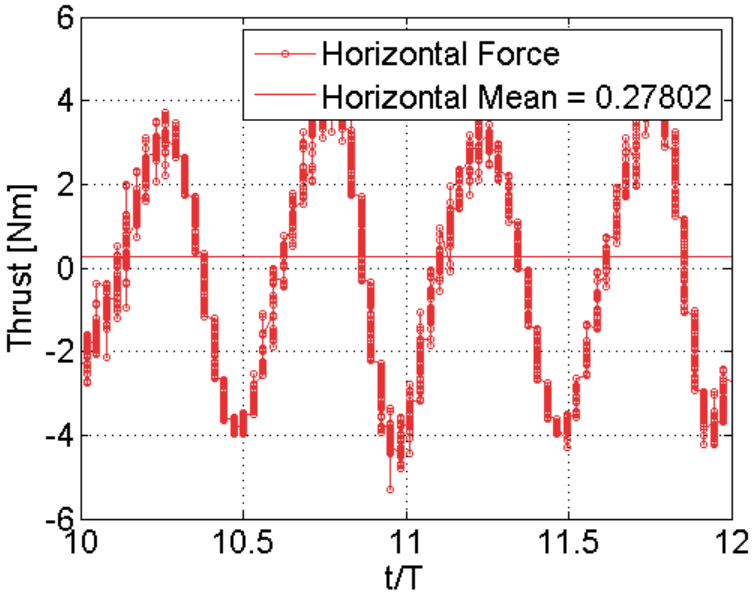

Figure 3.21: Test case forces with reduced speed (a = 5 cm, f = 0.3 Hz, $\phi = 30°$, U = 0.1 m/s)

In viewing the thrust forces generated (Fig. 3.21), it is shown that a net forward thrust is achieved, which further suggests the presence of a reverse von Kármán street. It can be seen that, contrary to the lower Strouhal number case, the maximum thrust forces are generated at the $\frac{t}{T} = 0.25$ & 0.75 instances, or where the hydrofoil amplitude is at a maximum.

Chapter 4

Test Platform Development

This chapter describes the design and construction of the experimental platform used to generate experimental data for comparison with the numerical model. The computer-aided design (CAD) model of the experimental design is presented enabling the important considerations to be better explained. Firstly, the necessary measurements are stated along with how they are achieved mechanically. Next, the construction of the platform and the foil is fully documented. Based on the projected forces and physical arrangements, the electronics were selected. Lastly, two foil control strategies are discussed. All construction was performed at Technical Services of Memorial University of Newfoundland. The complete drawing package can be seen in Appendix C.

4.1 Relevant Measurements

In the interest of evaluating oscillating foil capabilities and enabling comparison between mathematical and numerical models, the following measurements are required.

1. The dynamic horizontal and vertical forces
2. The angular position and speed of the foil.
3. The hydrodynamic torque at the pivot point of the foil.
4. The wave heights and frequencies.

Figure 4.1 shows the CAD model of the experimental platform after several iterations. The design of the platform itself will affect the manner in which the quantities are measured. With this in mind, a decision was made to measure the position, angular speed, and torque of the foil, directly at the location of the foil itself (i.e. underwater) requiring an additional waterproof housing to be developed. The thrust and vertical forces are measured above the water surface by using a L-shaped strut and a four load cell arrangement. A more detailed explanation follows.

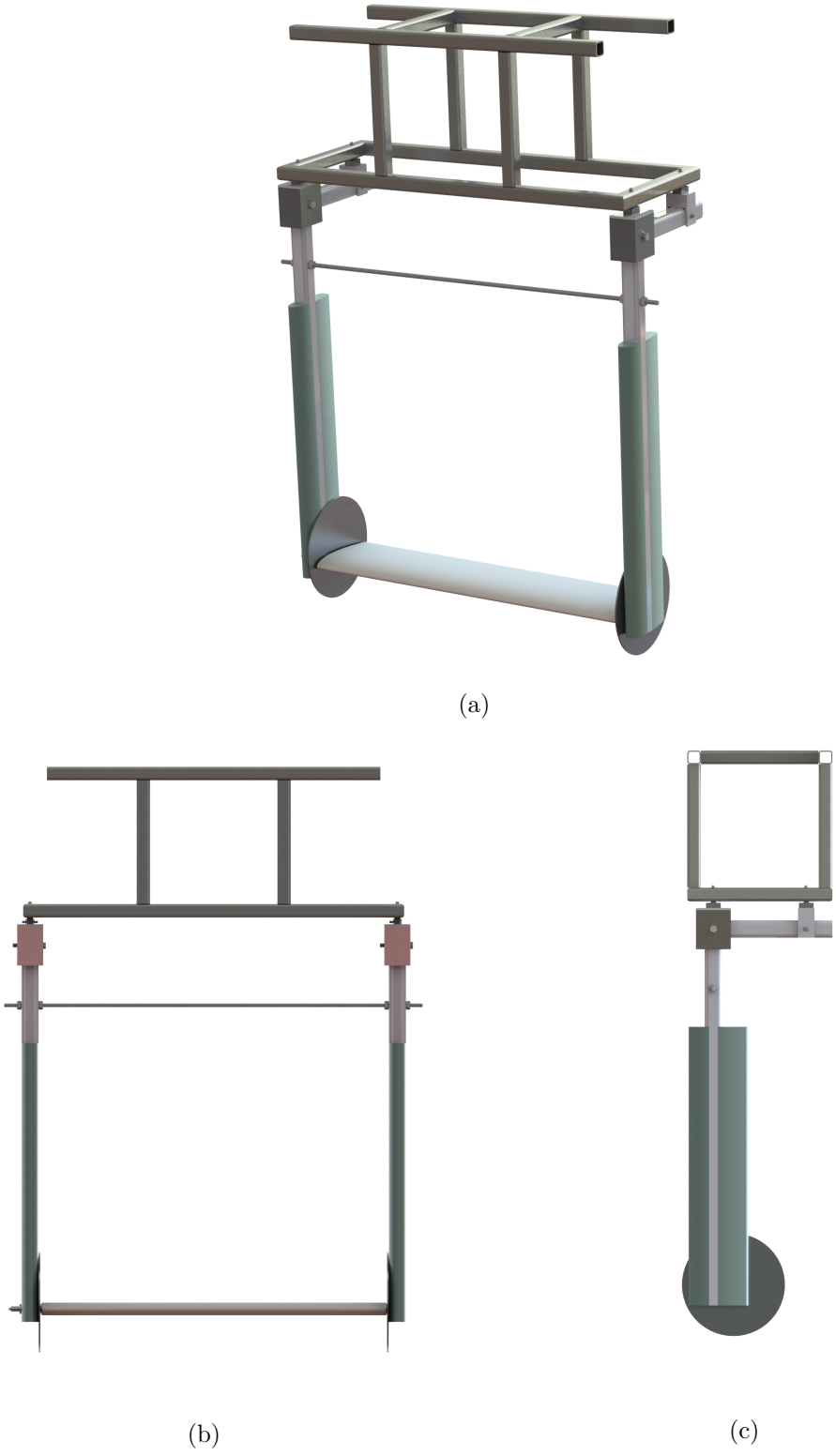

(a)

(b)

(c)

Figure 4.1: Platform overview: (a) Isometric view (b) Front view (c) Side view

4.2 Platform Design

4.2.1 Mechanical

The complete mechanical platform without the foil is shown in Figure 4.2. The frame provides a means of easy installation on the tow tank carriage and acts as a top base for load cell attachment. For installation, the platform is twisted 90 degrees, and a ceiling crane is used to lift the platform through the carriage rails. After the top portion of the frame is clear, the entire platform is rotated back and set in place. Figure 4.3 shows the platform installed.

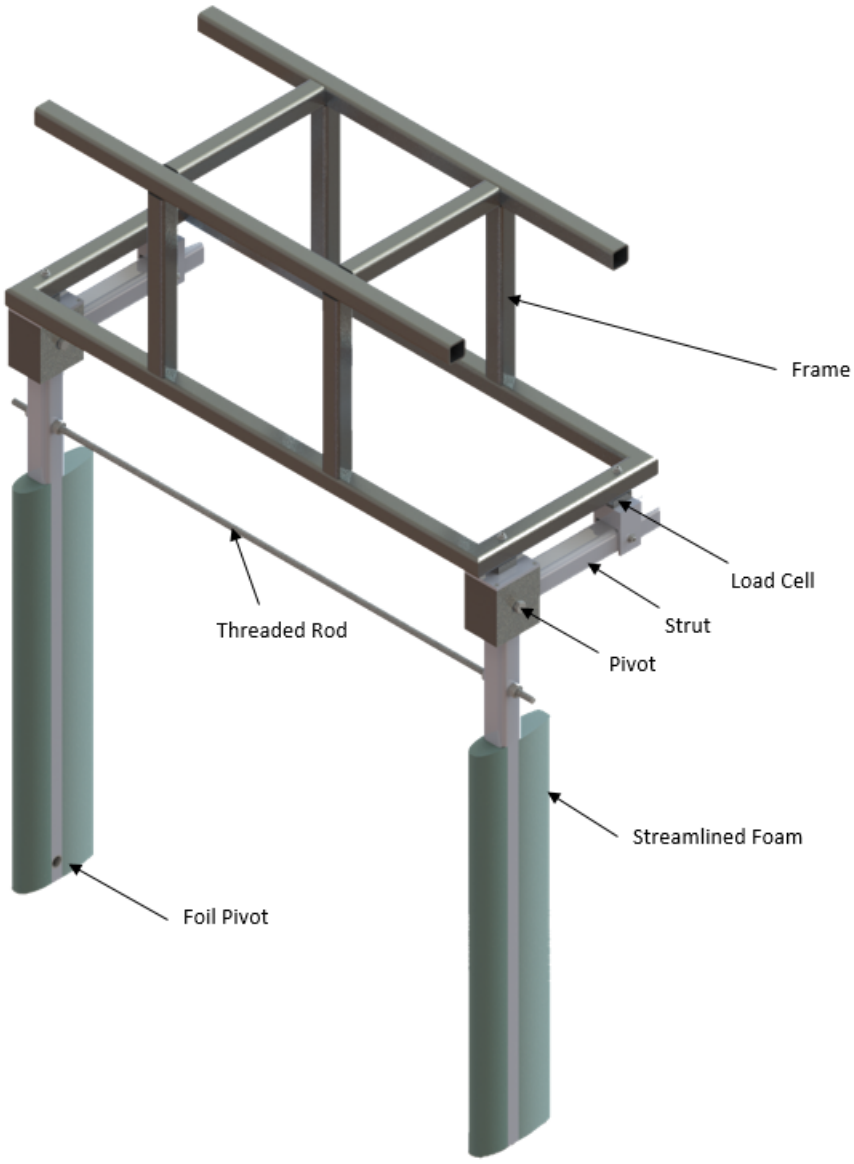

Figure 4.2: Mechanical frame

Figure 4.3: Installed frame

The two L-shaped struts were designed to facilitate force measurement, as stated in the previous section, as well as providing an attachment point for the foil. Both the frame and the struts are made from aluminum. The significance of the threaded

rod on the platform struts is two-fold. Firstly, being able to tighten and loosen the struts facilitates the installation and removal of the foil on the frame, and secondly, tightening the bolts reduces the platform vibrations felt during testing.

4.2.1.1 Hydrodynamic Considerations

The underwater components of the experimental platform will have an influence on the measured forces, possibly drowning out the horizontal and vertical forces that are of interest. To minimize this effect, the underwater portions of the experimental platform must be streamlined. To this end, 3-D printed streamline pieces of polystyrene foam were cut into two inch thick pieces using a water jet and attached to the submerged sections of the two struts. In addition to the polystyrene pieces, circular end plates were attached to each strut to minimize three-dimensional effects.

4.3 Hydrofoil

High-density polyethylene (HDPE) was chosen as the material for the hydrofoil due to its desirable surface finish, machineability, and similar density to water. Twenty pieces were cut using the CNC machine and attached to one another using screws and dowels. As shown in Figure 4.4, an aluminum tube was inserted within the foil to provide torsional rigidity.

Figure 4.4: Foil segment

In order to use the selected motor to control the hydrofoil and minimize any disturbance to the flow, it was decided to use the aluminum tube as an underwater housing. End caps with o-ring seals, and a shaft seal were designed to prevent any water ingress. As shown in Figure 4.5, the motor is screwed to the motor adapter piece, which is attached to the end cap and secured to the foil itself. The motor shaft is then fixed to the left strut via the shaft ground piece using a key-way. In this manner, under

normal operation the shaft remains stationary and the motor assembly moves, thereby moving the foil with it. This unusual method of operating a motor supersedes the need for any external housing. The power and encoder leads are connected using a high strength ROV cable which protrudes through a cord grip seal, out the right side end cap and through the right side strut and ultimately to the surface electronics.

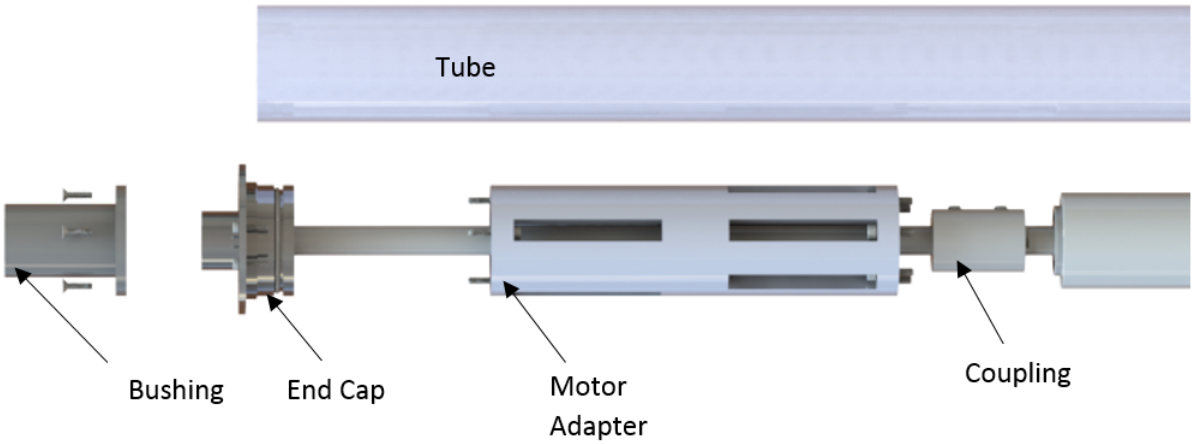

Figure 4.5: Exploded view of the motor assembly

4.4 Electronics

The following sections will outline the electronic components selected to complement the test platform.

4.4.1 Load Cells

The main constraints governing load cell selection was providing an economical means of measuring tension and compression forces in both directions and have a small form factor. The LC703 from OMEGA provides the tension-compression operation desired in a low profile, rugged, and high accuracy design. Based on the expected loads from

mathematical and simulation models, the 50 lb configuration was chosen (Figures 4.6 & 4.7). The specification sheet can be viewed in Appendix E.

Figure 4.6: Selected load cell

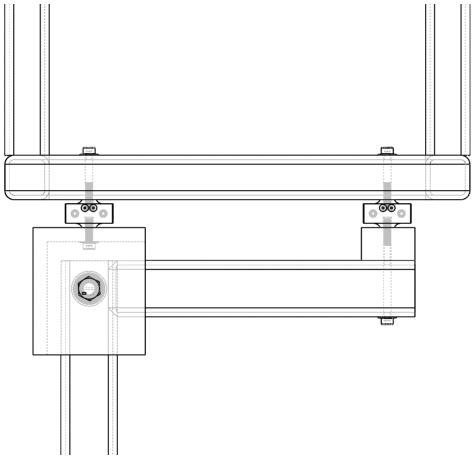

Figure 4.7: Sensor installation

The load cells output a voltage signal with a range of ± 5 mV, which must be amplified in order to be read by standard means. The signal conditioners selected are Dataforth SCM5B38 which have a simple strain gage input and output a ± 10V signal. Figure 4.8 shows the signal conditioner.

Figure 4.8: Dataforth signal conditioner

4.4.2 Maxon Motor

Using the simulation data, a maximum torque on the 1/4 chord position of the hydrofoil of approximately 3 Nm was assumed, and a safety factor of 1.5 applied, resulting in a motor requirement that can resist a torque of at least 4.5 Nm. The safety factor was selected to be high, as stalling the motor is likely to cause damage and must be avoided at all costs. An appropriate motor with a continuous stall torque of 5 Nm was selected from Maxon® (see Fig. 4.9). The specifications can be viewed in Appendix E

Figure 4.9: Selected motor

The position of the foil at any point during testing will be known from the 1024 CPR quadrature encoder included on the DC motor. The reference (or zero) position is when the foil is placed flat and the leading edge faces opposite the wave propagation direction. The angular velocity of the foil can be obtained via the output from the motor encoder and the time-stamp that is obtained from the Mbed® micro-controller.

4.4.3 Motor Driver

The Maxon motor requires a motor driver to amplify the control signal sent from the micro-controller. A Polulu 36v20 CS was selected to complement the voltage and current limits of the motor, with the added benefit of outputting a voltage signal proportional to motor current. This measurement will be used as an indirect means of inferring the hydrodynamic torque on the foil. The on-board current sensor is powered by shorting pins 5V(out) to VCS as shown in the driver pin-out in Figure 4.10.

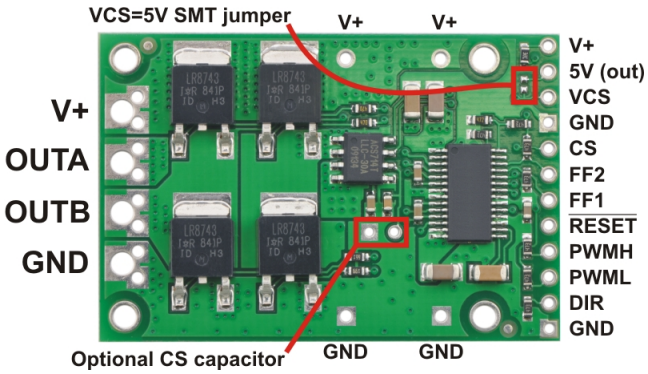

Figure 4.10: Polulu high-powered motor driver with current sense

The driver also has the added advantage of a 'coast'mode, where also connecting the PWM control signal to the PWML pin enables the foil to spin freely, bar only the system friction when the motor is powered. This being in contrast to normal motor operations, where the motor will hold position when powered. It should also be noted that the speed and direction command signals sent from the micro controller were first converted from 3.3 volts to 5 volts using a small circuit using bidirectional field-effect transistors (MOSFET) and resistors to satisfy minimum voltage requirements of the driver.

4.4.4 Teensy 3.1

A Teensy® development board was selected as the prototype micro-controller for foil control and data logging for its relatively easy coding environment, small footprint, and high precision encoder library. Figure 4.11 illustrates the various capabilities of the micro-controller. It is connected via USB serial to the PC, where data can be sent and received over the serial connection. In this scenario, the Teensy was used to receive the control signal from the PC and output it to the driver. It was also used to log both the analog voltage reading from the current sensor, and the digital signal from the encoder.

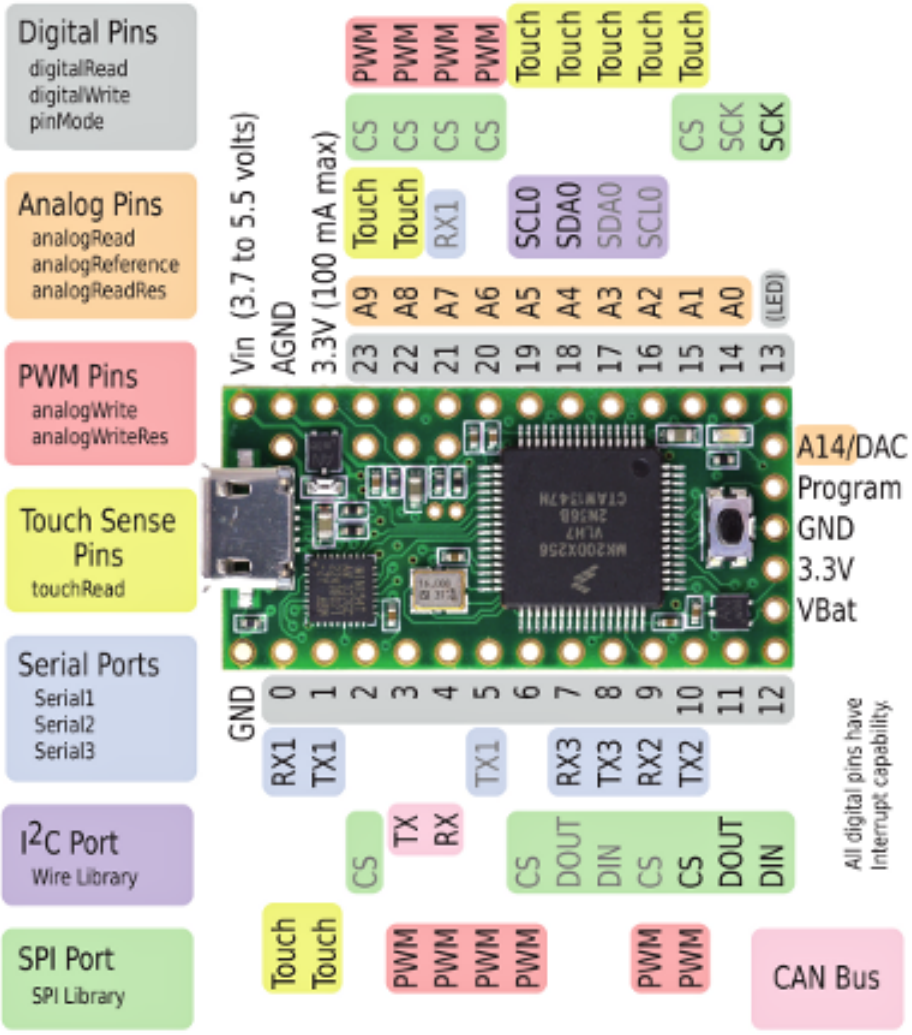

Figure 4.11: Teensy micro-controller

4.4.5 Labview

Lastly, the sensor and motor control data is interfaced with the Teensy environment using Labview® graphical programming software by National Instruments [67]. A graphical user interface (GUI) is developed, permitting the user to start and stop the motor, log data, and monitor of the all measurements in real-time. The latter being very convenient in the case of a sensor giving false measurements or the motor

malfunctioning. The load cell and wave probe readings are fed into the NI 6211 data acquisition unit and connected to the PC via serial connection.

4.4.6 Electronics Installation

The installed electronics are illustrated below.

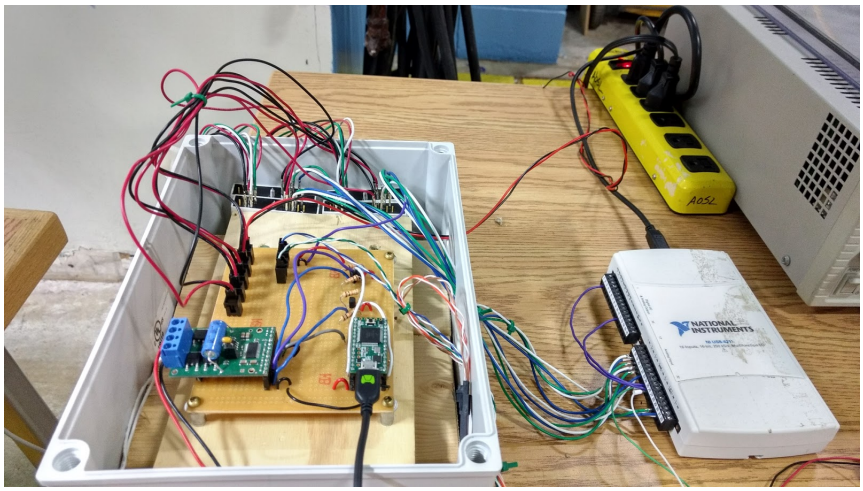

Figure 4.12: Installed electronics

This combination was installed on the tow tank carriage along with the required power supplies and control computer.

4.5 Foil Control Strategy

Two control modes were developed for experimental testing, namely, a prescribed mode and a spring mode. In the prescribed mode, the foil is made to oscillate sinusoidally wherein the foil amplitude is variable, and the frequency is same as the incident wave. In the spring mode, the foil reacts to being displaced by the waves and returns to its initial position. The code was written using the Teensyduino editor. A control diagram is presented in Figure 4.13 below.

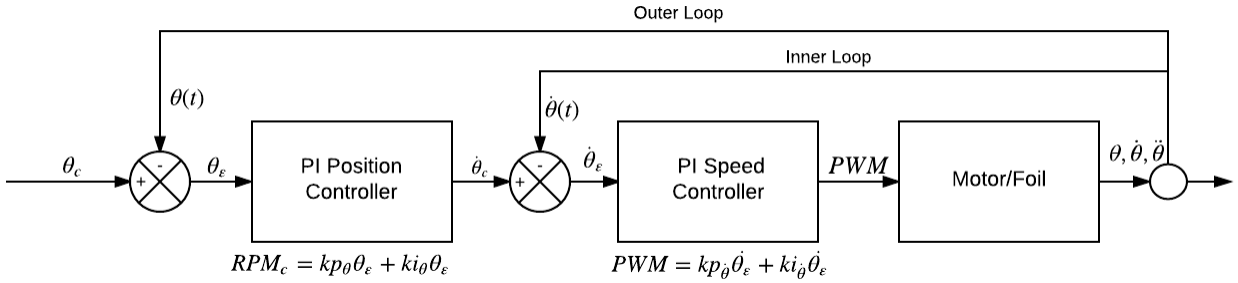

(a)

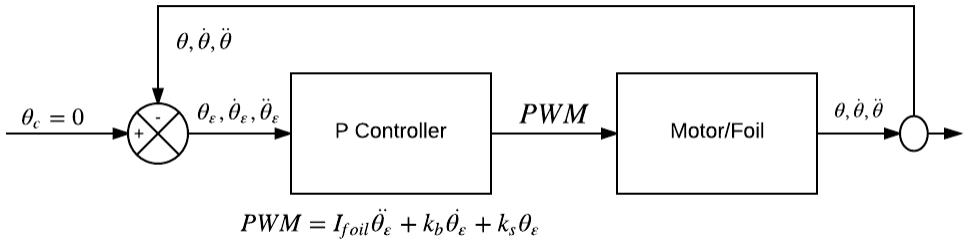

(b)

Figure 4.13: (a) Prescribed mode (b) Spring mode

In the prescribed mode (Fig. 4.13a), an inner and outer loop can be seen, where the outer (or primary) position control loop creates the reference signal needed for the inner (or secondary) speed control loop. This is known as cascaded control. This control method was selected over a classic PID controller, since the speed reference signal provides an early warning of a disturbance, such that the speed controller can immediately begin corrective action before the position has been substantially impacted. In other words, this results in less variability in the position. The proportional and derivative gains were selected sequentially in the innermost speed loop first, followed by the outer position loop, and then the gains were fine-tuned to achieve motion with minimal deviation from the input signal. The resulting feedback deviated less than one degree from the input sine wave and was thus considered as sinusoidal.

For the spring mode, a simple P-controller was implemented, where the main challenge for success is accurately determining the coefficients of position and its derivatives. This is discussed in the following chapter.

Chapter 5

Physical Testing

In Chapter 4, the hydrodynamic platform was constructed and electronics selected. Before testing could occur, the motor and load cells were calibrated and ground truth tests were be performed to ensure the platform produced accurate results. Once complete, an experimental design was developed and executed at the wave tank of OERC. As done with the simulation, the data was used to develop a regression equation highlighting the important factors in force development. Comparison with the simulation model shows that both models exhibit similar trends, although there is small offset between the models.

5.1 System Identification

Due to the unusual operation of the motor, and the desire to use the current sensor as an output torque reference, the full system was calibrated in steady-state and dynamic conditions to determine the contribution of various inherent frictional losses. The system inertia was also measured to enable a system equation of motion to be developed. Next, the load cells were calibrated in-situ, by applying a combination of known loads in both horizontal and vertical directions. Lastly, the wave probe was

calibrated.

5.1.1 Motor and Current Sensor Calibration

For the torque reference, the signal of the current sensor was first analysed to determine if any filtering was required. For finer signal smoothing, a exponential moving-average (EMA) filter was implemented in the micro-controller code resulting in a smooth, responsive signal. It was found that the current sensor samples are obtained at a minimum rate of approximately 5 Hz. While this is less than the input PWM signal, it is much faster than the fastest wave frequency (0.5 Hz) tested, permitting the wave influence on the hydrodynamic torque to be measured.

Next, the friction of the motor and gearbox were characterized in steady-state conditions, by applying known mechanical loads on the motor shaft at various duty cycles and logging the encoder and current sensor data. Figures 5.1 and 5.2 show the bench set-up.

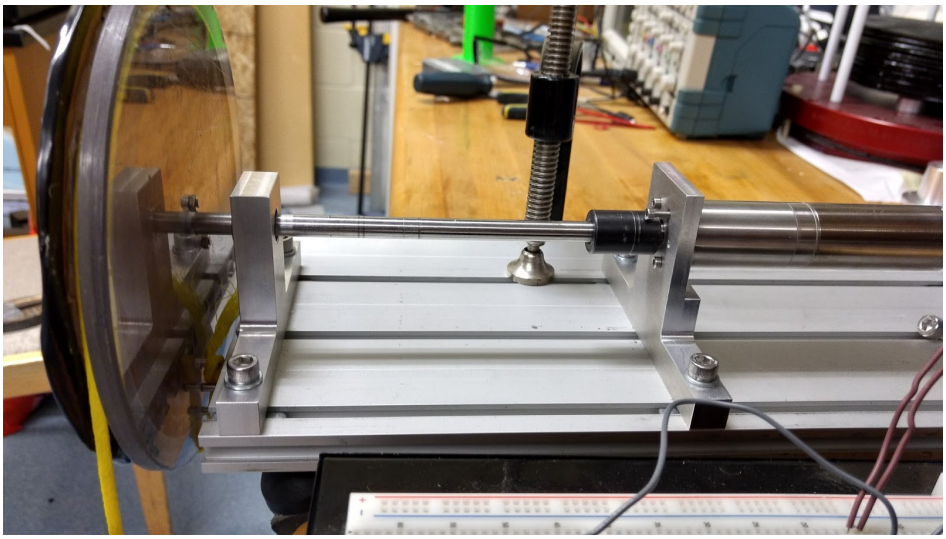

Figure 5.1: Side view

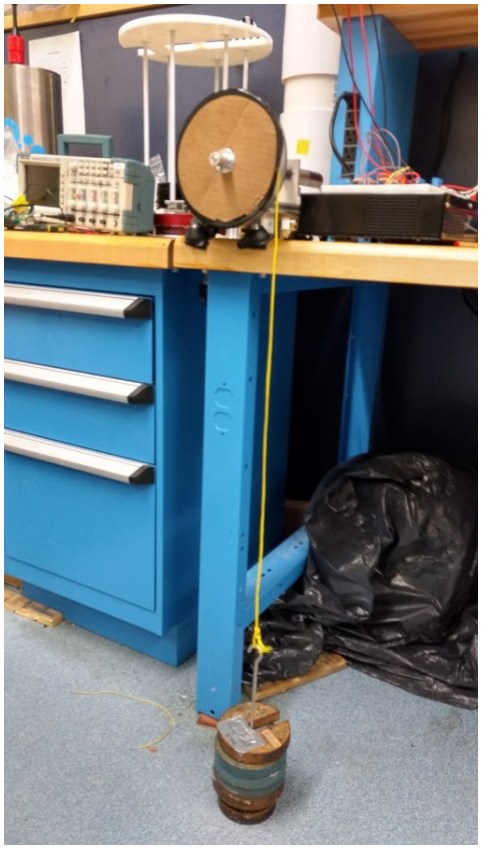

Figure 5.2: Front view

A circular disc was attached to the shaft, on which a weight was hung. This provided a constant moment vector as the motor spun. Operationally, the motor was run in both clockwise and counter-clockwise directions with various mechanical loads applied in a pyramidal test order. The load was gradually increased to the maximum rated continuous load of the motor and then subsequently unloaded. This enabled any tendency of the motor measuring in one direction more than the other to be evaluated. For each load, the voltage output of the current sensor was measured, and converted to a change in applied current and used to estimate the output (system) torque required for different loading conditions. This was done at 25%, 50%, 75%, and 100% duty cycles, to reflect the operation in the spring mode, where the PWM duty-cycle self-adjusts based on the encoder readings.

The full results of the experimental speed-torque curve is shown in Figure 5.3.

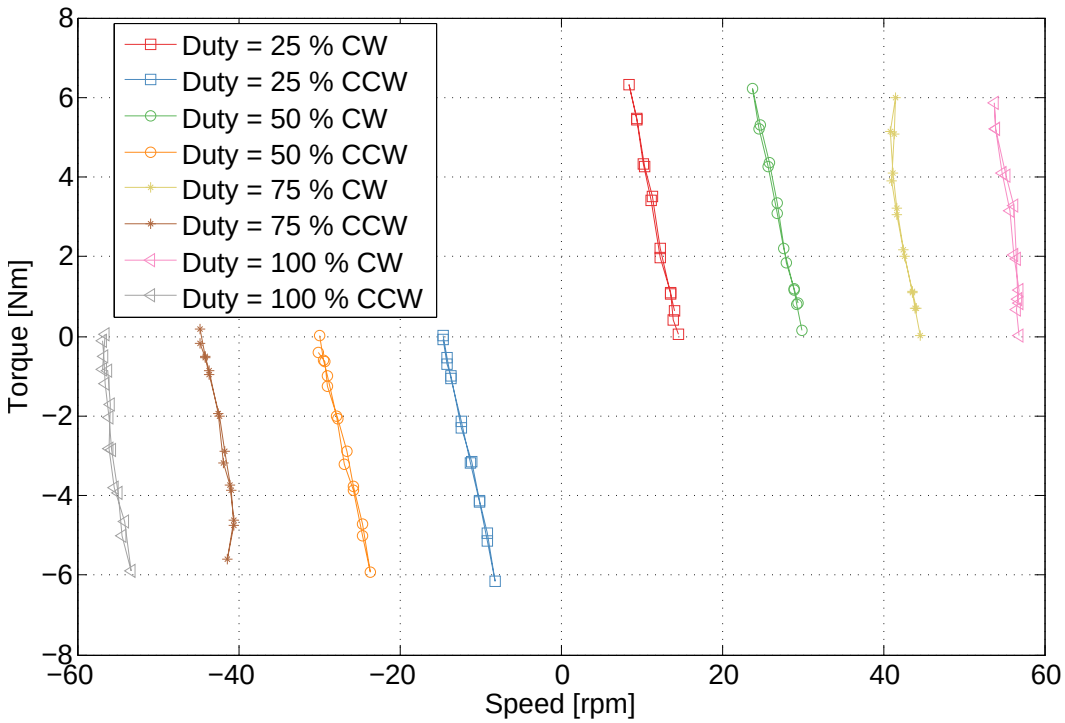

Figure 5.3: Torque-Speed curve

To obtain the contribution of internal friction on the torque, the known loads applied were subtracted resulting in the following curve (Fig. 5.4).

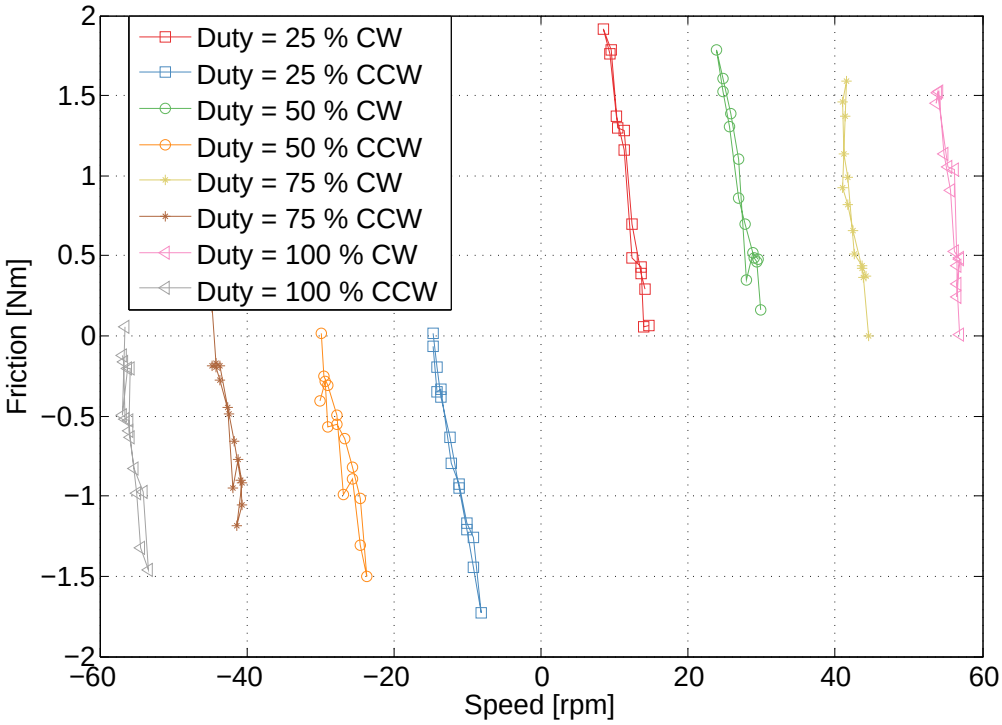

Figure 5.4: Friction-Speed curve

As expected, the different duty cycles only affect the motor speed since it directly controls the voltage. The range of torques applied by the motor remains relatively constant. By applying a linear curve fit equation to all of the duty cycles individually, the frictional coefficient contribution due to the motor and gearbox can be estimated. Additionally, there will be a frictional component due to the shaft seal and the foil bearings. To estimate this value, the motor is installed in its final position within the foil and given steady state velocities in both directions. The current sensor and encoder data is used to develop a friction speed curve, where the previously determined frictional effect of the motor internal friction and gear box is removed, as is the moment contribution due to the weight of the foil. In the last dry land test, the foil is given a prescribed sinusoidal motion at the frequencies of the waves to be tested, allowing the dry system inertia to be measured. The latter test was performed again with

the foil completely submerged. By redeveloping the friction-speed curve, the added mass effect caused by the foil accelerating the surrounding fluid was estimated. The coefficients listed below in Table 5.1 were used to develop a system equation of motion 5.1. This equation is required for the implementation of the variable spring-mode within the Teensy code.

Table 5.1: System Coefficients

Coefficient	Value	Description
k_{f1}	0.45	Internal friction
k_{f2}	0.005	seal/bearing friction
I_{sysDry}	5.0197 $\frac{kg}{m^2}$	System Inertia (within 10% of Solidworks value)
I_{sysWet}	5.719	Added mass + wet inertia
k_s	1-3	User-defined spring constant
k_m	0.0429 $\frac{Nm}{Amp}$	Motor constant
i_m	dynamic	Current sensor measurement
M_{foil}	6.18 [kg]	Dry foil mass

$$I_{sys}\ddot{\theta} + (k_{f1} + k_{f2})\dot{\theta} + M_{foil}rsin\theta = k_m i_m \tag{5.1}$$

5.1.2 Force Measurement

Considering that positive and negative force measurements in both horizontal and vertical directions are necessary, the load cells were calibrated in-situ to determine any tendency of cross-talk between load cells. Since the load cells must be fixed both to the strut and the frame in order to measure in two directions, cross-talk will occur. The calibration was performed on the staging platform shown in Figure 5.5. A combination of pulleys and ropes were used to apply the loads.

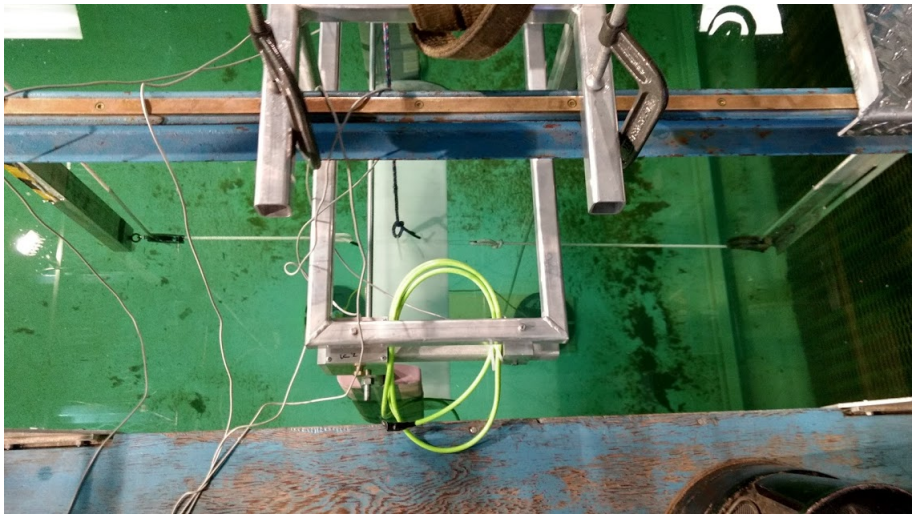

Figure 5.5: Load cell calibration set-up

In order to decouple the load cell readings, a calibration matrix was developed by applying known loads in a combination of horizontal and vertical directions. The Moore-Penrose pseudo-inverse method was applied to extract the calibration matrix, which was then evaluated by predicting the known applied loads. It can be seen in Figures 5.6, and 5.7 that the root mean square error (RMSE) of the vertical forces is larger than the that of the horizontal, but is still quite acceptable.

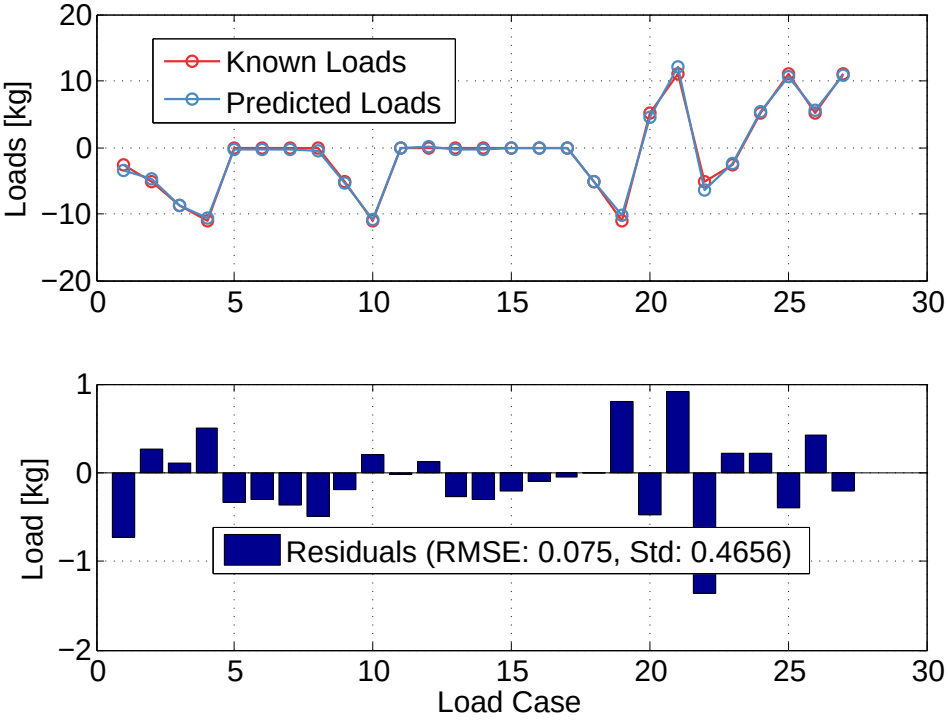

Figure 5.6: Horizontal loads

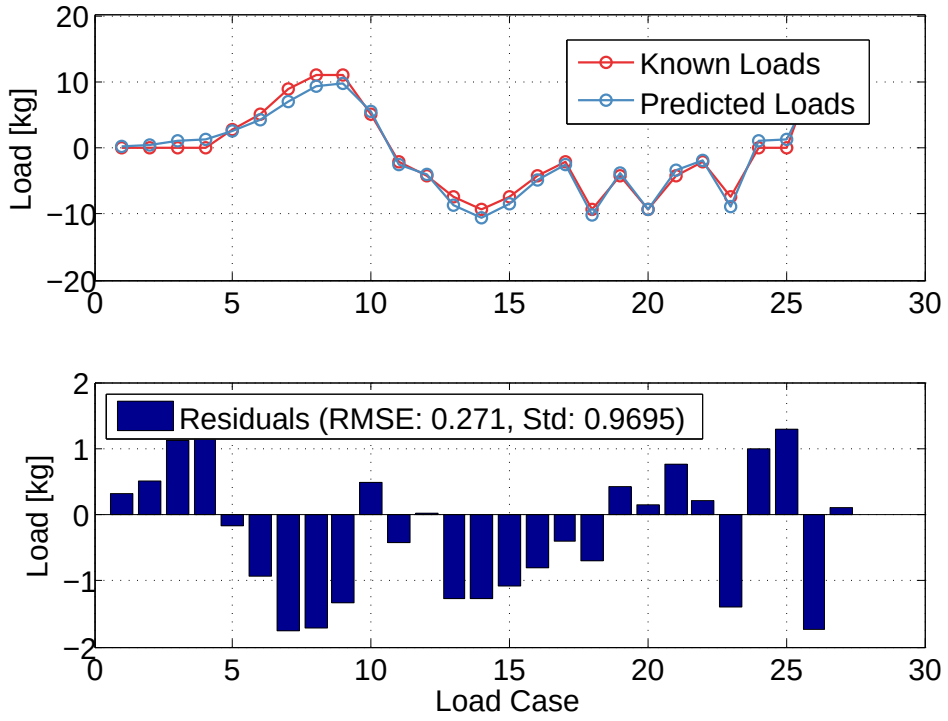

Figure 5.7: Vertical loads

5.1.3 Wave Probe

A wave probe similar to that shown in Figure 5.8 measures the change in capacitance in the wires when the water depth changes. It was calibrated by taking measurements at 50 mm increments to develop a linear equation. The equation slope was implemented within Labview® to log the data in centimetres.

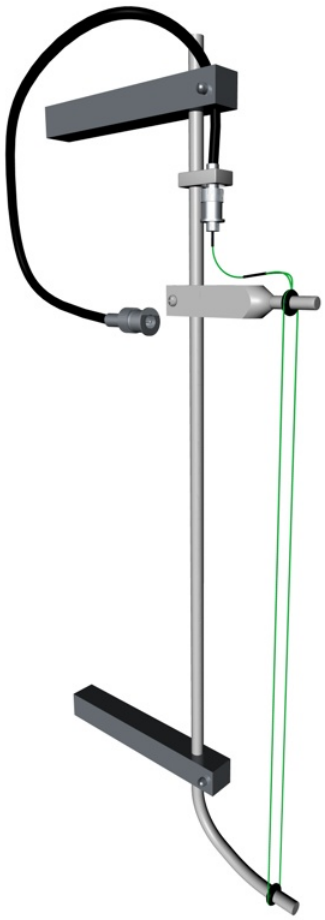

Figure 5.8: Wave probe (Image from http://www.akamina.com)

The wave board at the OERC was found to provide reliable, repeatable wave frequencies, however the wave heights were often unpredictable. For this reason, the measured wave heights will be used within the developed experimental model to compare the

agreement between experiment and simulation. In addition, it should be noted that due to the dispersion relation for deep water waves, and the physical depth of the wave tank, the water particle orbit at the water surface is actually elliptical rather than circular. This results in the vertical excursion of wave particles at the surface equalling the wave height, and the horizontal excursion being slightly larger. This is worth mentioning as in true deep water waves the horizontal range of motion of the water particle will be smaller, possibly affecting the resulting forces on the hydrofoil.

5.2 Test Plan

As with the simulation experiment, DOE methodologies were also selected for the physical experiment. A response surface methodology (RSM) known as a central-composite design (CCD) was selected to permit up to a quadratic model to be developed. This popular design was selected over a Box-Behnken Design (BBD) since BBDs are not recommended for extreme treatment combinations (i.e. at the extreme points of each factor). The CCD contains an embedded factorial design and adds treatment combinations at axial points and center points. Although typically a CCD contains five levels per factor, in this case, a face-centered CCD was selected to facilitate experimentation, resulting in only three levels per factor. Further details can be found in [68]. This RSM technique is used to develop an optimization model, where, in this case, an averaged maximum positive thrust force is the desired outcome. Along with the horizontal forces, the average vertical forces in each run are also considered. The run parameters are shown in Table 5.2.

Table 5.2: Face-centered CCD

Run No.	Wave Height H [cm]	Wave Freq. f [Hz]	Pitch Amp. ϕ [degrees]	Flow Vel. U [m/s]	R1:F_x [N]	R2:F_z [N]
1	5	0.5	30	0	1.24	0.66
2	3	0.4	20	0.2	-0.25	3.15
3	1	0.3	10	0.4	-1.85	2.26
4	1	0.5	30	0.4	-4.28	10.66
5	1	0.5	10	0	0.54	0.28
6	5	0.3	30	0.4	-4.44	7.95
7	1	0.3	30	0	0.55	0.44
8	3	0.4	20	0.2	0.07	2.54
9	5	0.5	10	0.4	-1.49	3.53
10	5	0.3	10	0	0.45	0.53
11	5	0.3	30	0	1.12	-0.05
12	3	0.4	20	0.2	0.26	3.87
13	5	0.5	10	0	1.44	0.84
14	1	0.3	30	0.4	-2.48	2.53
15	1	0.5	10	0.4	-1.23	4.19
16	1	0.5	30	0	3.04	0.97
17	5	0.3	10	0.4	-1.03	7.58
18	3	0.4	20	0.2	-0.19	2.50
19	1	0.3	10	0	0.36	0.70
20	5	0.5	30	0.4	-3.29	12.30
21	3	0.4	20	0	-1.24	0.66
22	5	0.4	20	0.2	-0.31	1.66
23	3	0.4	30	0.2	-0.25	4.96
24	3	0.4	20	0.4	-1.55	6.10
25	3	0.4	20	0.2	-0.18	1.93
26	3	0.3	20	0.2	-0.52	1.71
27	3	0.4	20	0.2	0.24	2.50
28	3	0.5	20	0.2	0.24	2.50
29	3	0.4	10	0.2	-0.44	1.40
30	1	0.4	20	0.2	-0.29	-0.19

The effects of the submerged platform need to be determined and ultimately subtracted from the measurements to obtain the desired foil effects. Accordingly, the same RSM run parameters were performed without the foil installed. It was found that only the forward speed significantly affected the forces on the struts, and thus for the three forward speeds tested, the corresponding effect of the struts is subtracted.

5.3 Results

5.3.1 Ground Truth

In order to ensure the platform produces realistic results, preliminary flat water tests were performed at fixed attack angles and compared with empirically determined force coefficients by Sheldahl & Klimas [46]. Simulated values using the K-omega SST turbulence model were also compared. For all tests, a Reynolds number of $1.7e+06$ is used, which resulted in a forward speed of 0.7 m/s. The results can be seen in Figures 5.9 & 5.10 below:

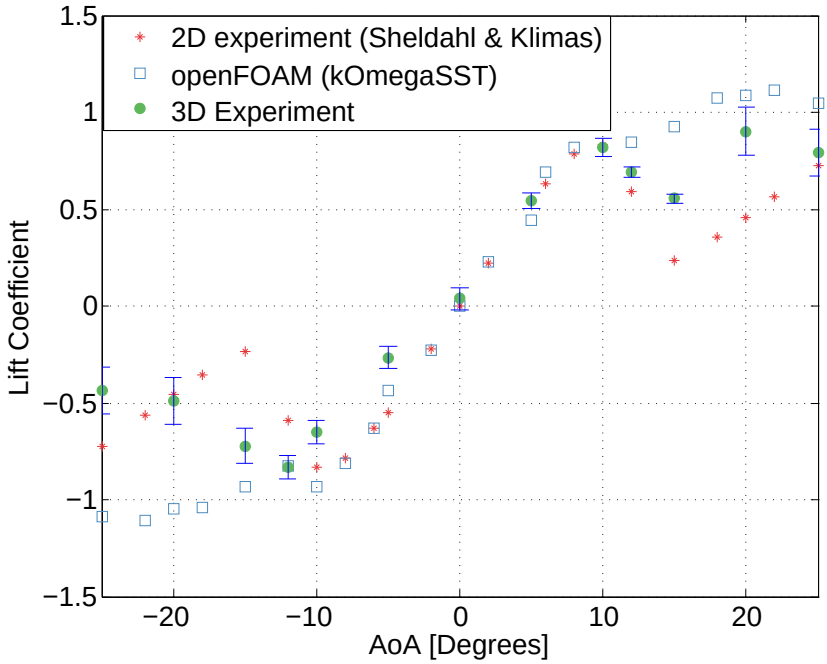

Figure 5.9: Lift coefficient curve. $U = 0.7$ m/s; Re $= 1.7 \times 10^5$

In Figure 5.9, the simulated and 2D experimental data match quite well up until stall, where the simulated data continues to increase, although a distinct change in the mean slope is apparent. The three-dimensional experimental results appear sufficient for positive attack angles with the exception of $\alpha = 20$ degrees. For negative attack angles however, a change in slope can be seen that results in the stall point being several degrees removed when compared to the other data sets. This is thought to be attributed to a limitation of the experimental platform itself, as it was noted that the negative vertical loads resulted in a slightly lower load cell sensitivity than the positive. The error bars represent one standard deviation above and below the data point, where the standard deviation was computed using the variation of the load cell measurements after the desired speed was reached.

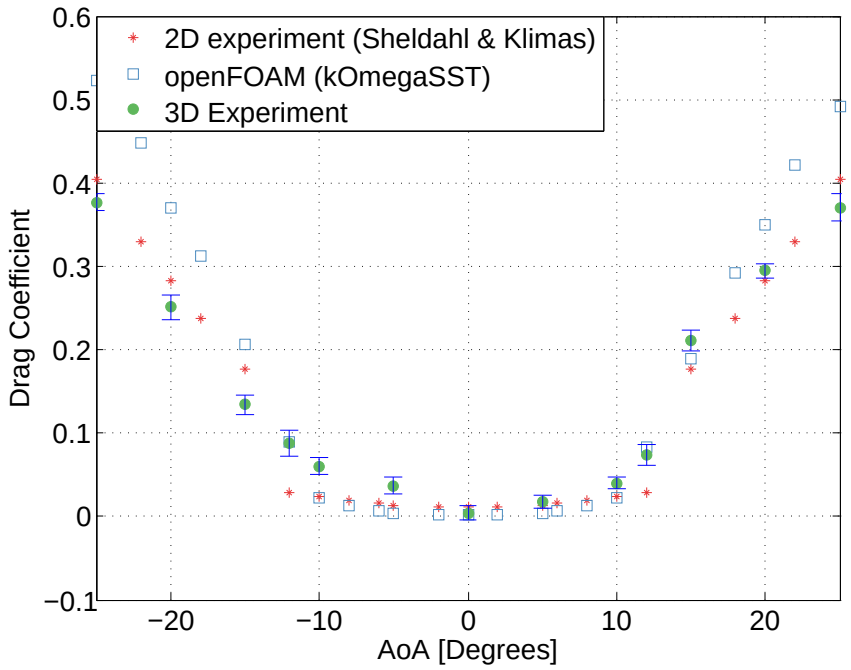

Figure 5.10: Drag coefficient curve. $U = 0.7$ m/s; Re $= 1.7 \times 10^5$

The drag coefficients shown in Figure 5.10 illustrate that the numerical results slightly overestimate drag at attack angles larger than ± 15 degrees. Both sets of experimental data are quite similar, however the three-dimensional results appear more variable, and slightly unsymmetrical. The variability and non-symmetry in both plots should be addressed in future works, preferably by incorporating flexible rods to completely eliminate mechanical cross-talk between the front and rear load cells.

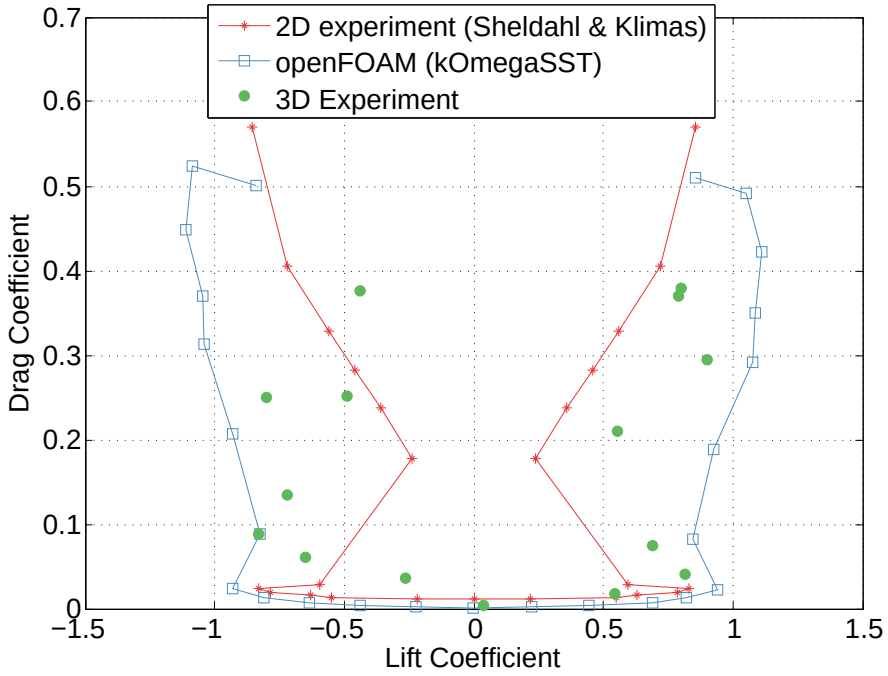

Figure 5.11: Drag vs. lift coefficient. $U = 0.7$ m/s; Re $= 1.7 \times 10^5$

Lastly, Figure 5.11 again shows more desirable results for the positive lift region than the negative, some non-symmetry of the three-dimensional data is again apparent. Overall, the trends between all curves are comparable for lower drag coefficients, and become harder to predict as drag increases.

5.3.2 Design of Experiments

The factors are restated in Table 5.3, along with the corresponding high (+1) and low (-1) values considered in the CCD design. The high and low values were selected considering what is possible within the OERC tow tank, as previously discussed in Section 2. Again, the relatively small wave heights possible within the wave tank make it unlikely that wave height will be deemed significant. It should be noted that the following models are only valid within the range of factors tested. Assumptions of normality, independence, and constant variance were met by both models.

Table 5.3: Control Variables and Subsequent Ranges

Factor	Description	Low (-1)	High (+1)
A	Wave Height, H [cm]	1	5
B	Wave Frequency, f [Hz]	0.3	0.5
C	Foil Amplitude, ϕ [Deg]	10	30
D	Forward Speed, U [m/s]	0	0.4
R1	Horizontal Force, F_x		
R2	Vertical Force, F_z		

5.3.2.1 Thrust Force

For the RSM analysis, a stepwise regression approach was used with a significance level of 5%. Starting with the average horizontal forces, the DOE analysis indicates that a two factor-interaction (2FI) model should be fit. The significance of the factors tested on the thrust developed is shown in a Pareto plot in Figure 5.12.

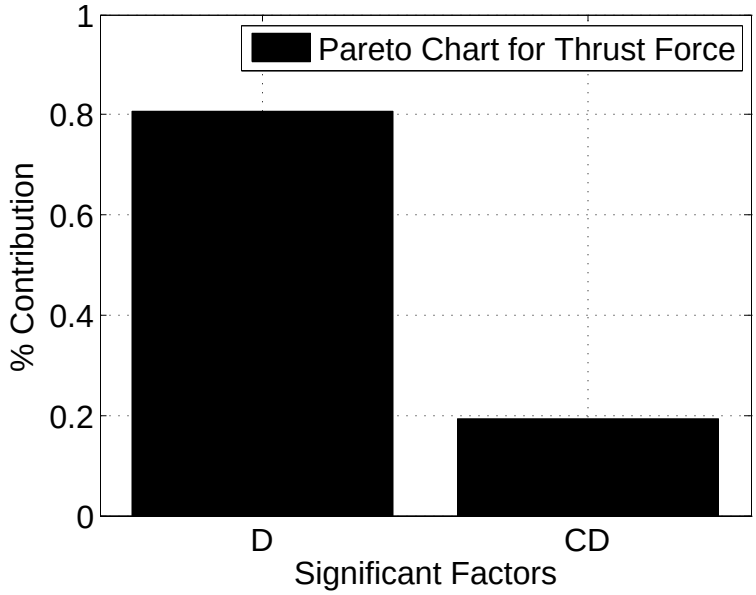

Figure 5.12: Pareto chart for the thrust force in the CCD analysis

Logically, it can be seen that the forward speed (D) is by far the single most significant factor for thrust, and also results in the next most significant factor combination when

combined with the hydrofoil amplitude (CD). In contrast to the simulation model, the wave frequency and its interaction with the foil amplitude are not present. As in the numerical Pareto plot generated via the uniform design (Section 3), the wave height is deemed insignificant for the ranges tested. The coded regression equation is presented below (Eq. 5.2).

$$F_x = -0.54 - 0.27\phi - 1.90U - 0.81\phi U \tag{5.2}$$

The model gave an adjusted R^2 value of about 0.79 and a predicted R^2 of about 0.69. The actual versus predicted values for the model is shown in Figure 5.13.

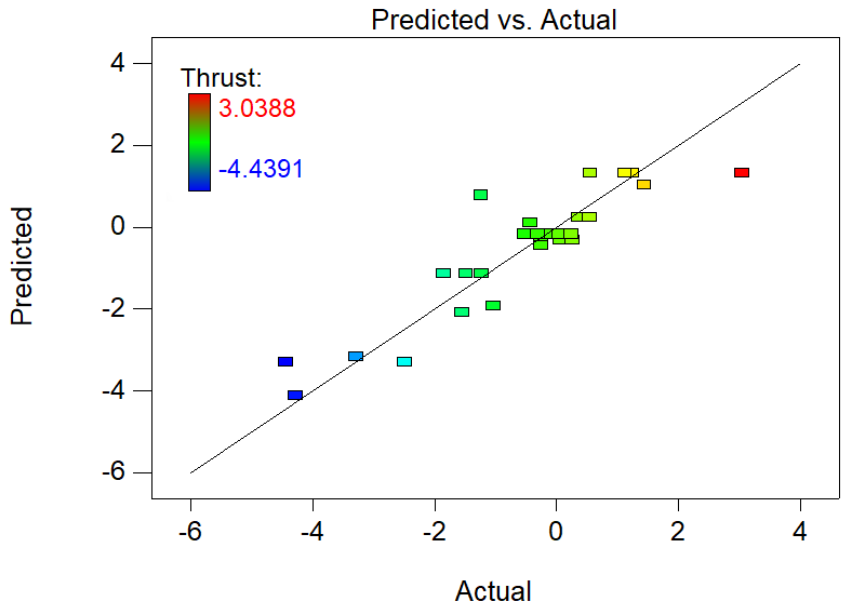

Figure 5.13: Actual versus predicted values for the thrust force in the CCD model

The interaction surface plot between the forward speed, U, and foil amplitude, ϕ, is shown in Figure 5.14. For this plot, the wave height and frequency were set to their corresponding midrange values (3 cm and 0.4 Hz respectively). It further illustrates

that the forward speed governs whether the hydrofoil amplitude is advantageous or not. For low forward speeds, a higher hydrofoil amplitude is preferred but as the forward speed increases, a smaller amplitude will result in positive thrust for a wider range of speeds.

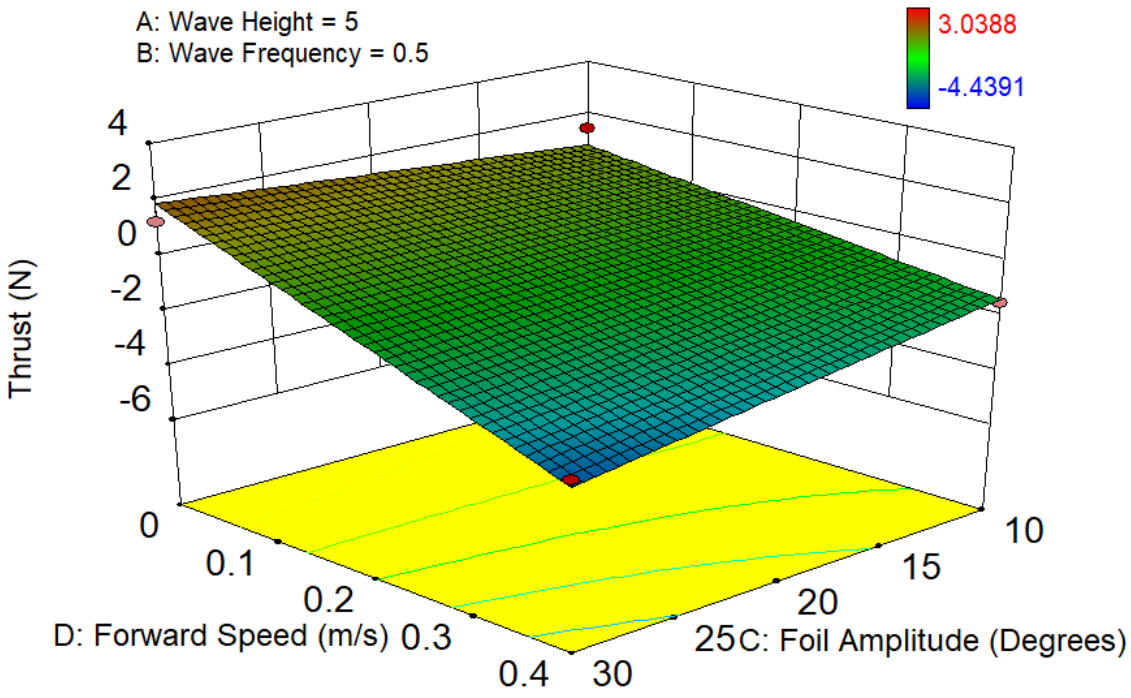

Figure 5.14: Three-dimensional surface showing the interaction effect of hydrofoil amplitude and forward speed on the thrust force

5.3.2.2 Vertical Force

The factor contributions to the vertical force response are shown in Figure 5.15.

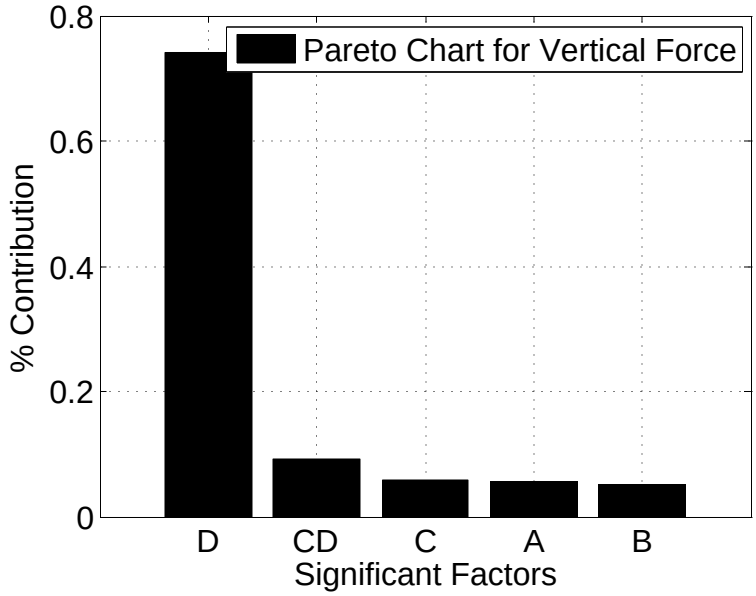

Figure 5.15: Pareto chart for the vertical force in the CCD analysis

Once again, the forward speed is the most significant factor, followed by its interaction with foil amplitude. Next, at similar significance levels are hydrofoil amplitude, wave height and wave frequency. The resulting coded model equation is shown below (Eq. 5.3).

$$F_y = 3.01 + 0.86H + 0.81f + 0.89\phi + 3.76U + 1.16\phi U \tag{5.3}$$

The adjusted R^2 and predicted R^2 are 0.79 and 0.62 respectively. The actual versus predicted plot is shown in Figure 5.16.

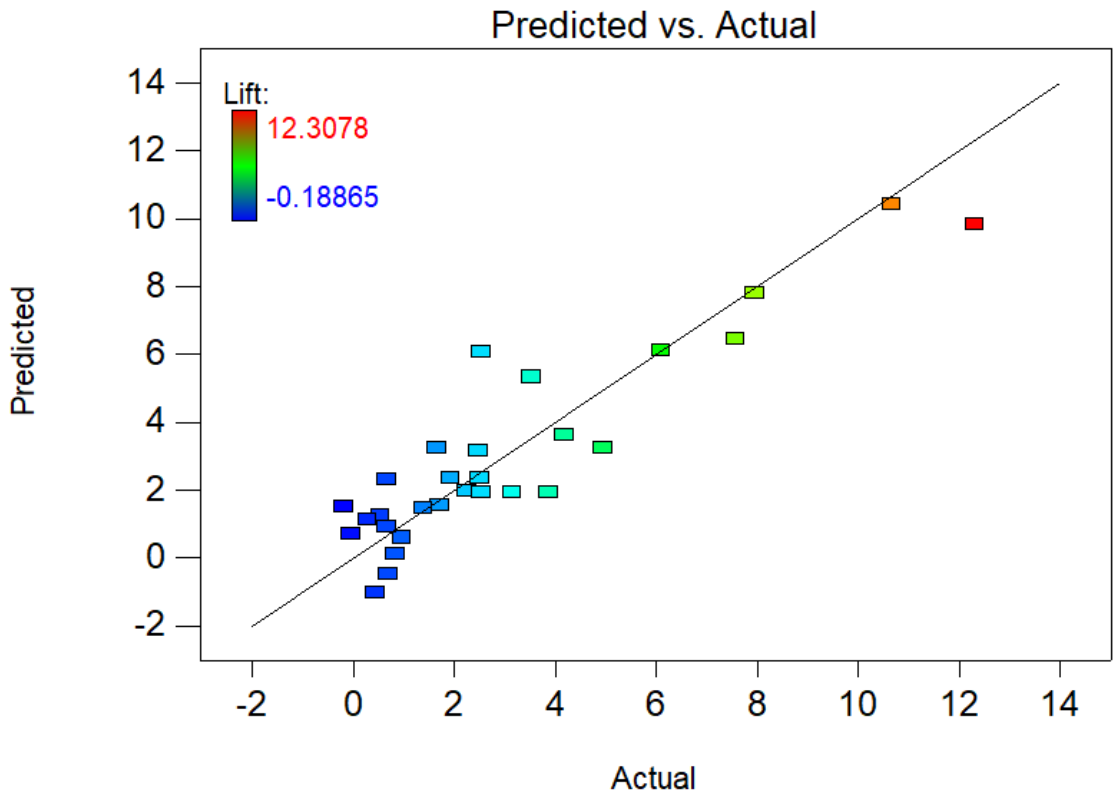

Figure 5.16: Actual versus predicted values for the vertical forces in the CCD analysis

Figure 5.17 shows the interaction between the hydrofoil amplitude and forward speed with the wave height and frequency set to their corresponding midrange values (3 cm and 0.4 Hz respectively). It can be seen that at low forward speeds, the lift remains relatively constant for increasing amplitudes. Conversely, at a faster speeds the lift increases with increasing amplitudes.

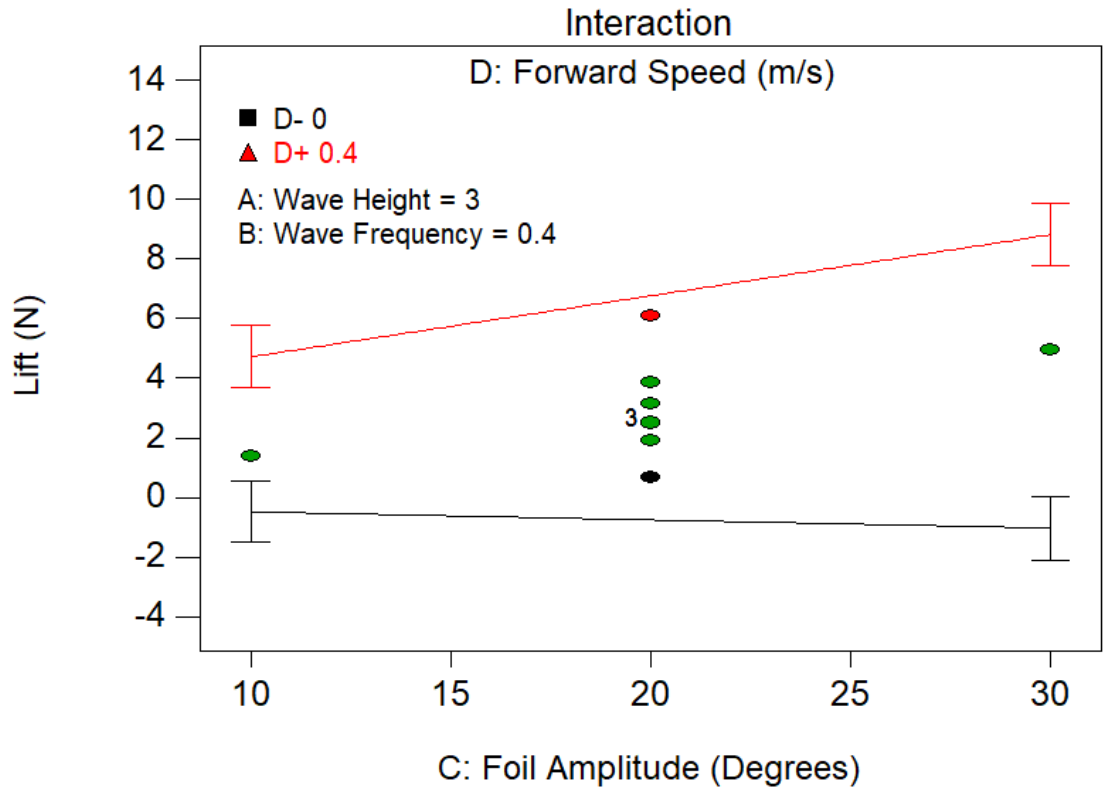

Figure 5.17: Interaction diagram between the hydrofoil amplitude and forward velocity

Similar to the uniform design analysis, the RSM analysis of the moment on the hydrofoil indicated that the overall mean did not change enough throughout the runs to necessitate a model. The mean of the moment is thus the best predictor of hydrofoil moment.

5.3.3 Comparison with Simulation

Using both thrust model equations developed via the simulation and experimental data respectively, a comparison of the two models is illustrated in Figure 5.18. While, in general, similar trends can be seen throughout the runs, it is apparent that the simulation does not capture all of the effects necessary to predict the generated forces.

In most cases, the simulated values are offset from the values given by the experimental model.

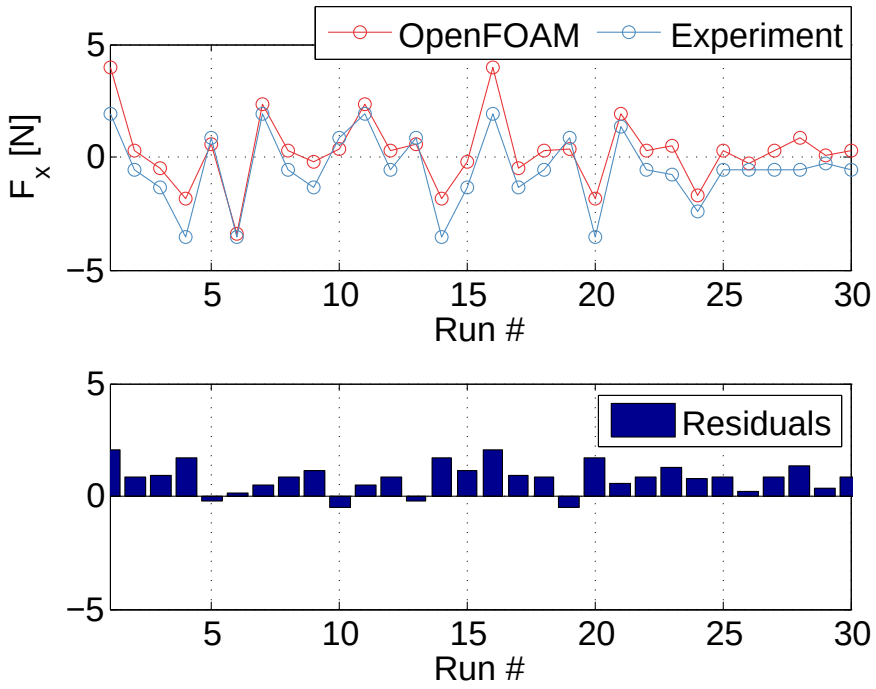

Figure 5.18: A comparison of the thrust force models generated in OpenFoam and experiment

The comparison of vertical forces shown in Figure 5.19 show a similar trend.

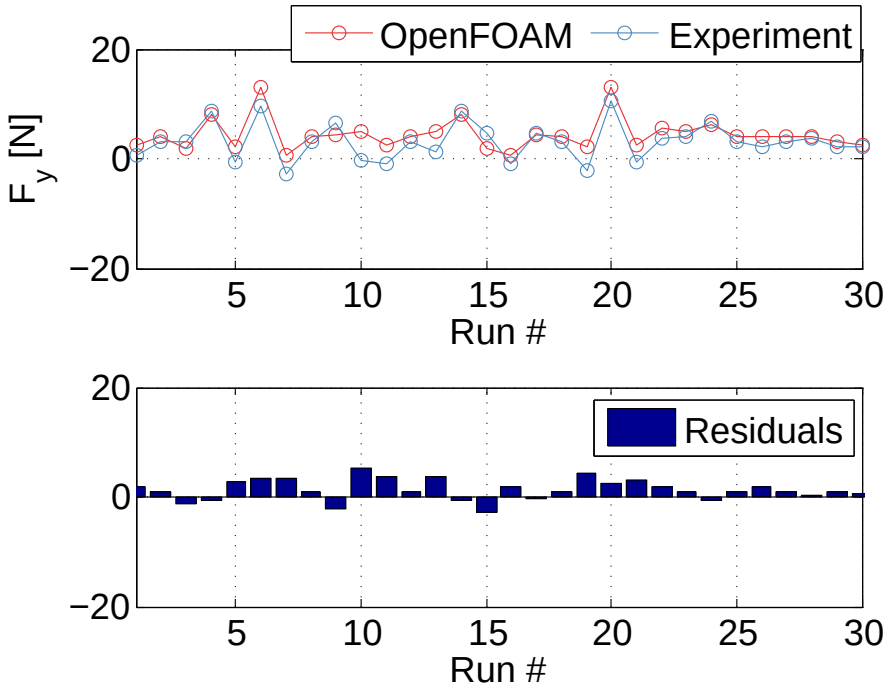

Figure 5.19: A comparison of the vertical force models generated in OpenFoam and experiment

While the prediction capabilities of the simulation model are not exceptional, it is motivating that the trends of the simulation model generally agree with the experimental model. It can be thus concluded with reasonable confidence that the four factors tested account for the majority of the influence on the developed forces.

Furthermore, for the significant thrust factors, both models indicate that forward speed is the most important factor, followed sequentially by the 2FI between forward speed and hydrofoil amplitude. However, in the simulation model, the wave frequency and the interaction between wave frequency and hydrofoil amplitude also meets the significance criterion. It is probable that the more controlled simulation environment allowed the smaller relative influence of these factors to be uncovered. For both models, lower speeds and higher foil amplitudes result in thrust production, more specifically,

both models indicate that the transition from thrust to drag production occurs in the neighbourhood of 0.2 m/s.

The vertical force models indicate all the same factors are significant, with the exception of wave frequency which is only present in the experimental model. A difference is in the second most significant factor, which is wave height for the simulation model and the 2FI of foil amplitude and forward speed for the experimental model. Both models indicate that increasing the hydrofoil pitch amplitude causes an increase in the vertical forces for a non-zero forward speed. Overall, increasing the significant factors in both model equations are shown to increase the vertical forces.

5.3.4 Note on Spring Test

Using the spring-mode control strategy developed in Section 4.5, several tests were performed to assess whether the hydrofoil can achieve similar motions as in the prescribed mode, forced only by the waves. The wave height was set to 5 cm for all runs performed, and the wave frequency, f, forward speed, U, and spring constant, K_s, were varied. In cases with non-zero forward speed, the foil was displaced by the incident waves and achieved an oscillatory motion, which was subsequently reduced as the foil reached the desired speed. The wave phase was found to self adjust to approximately 90 degrees. Unfortunately, no thrust was found to be produced. Indeed, even when the carriage remained stationary, only drag was found to occur. A likely cause of this is improper setting of the "zero" position of the foil, as it was later determined that the pitch angle of the hydrofoil had a tendency to be several degrees positive of the zero position. Overall, oscillatory pitching motions were achieved with the

spring-mode, however further testing is necessary to accurately determine its thrust producing capabilities.

Chapter 6

Conclusion & Future Works

6.1 Summary

The potential of using an oscillating foil as an energy transfer mechanism for ASVs has been investigated in linear gravity waves. By taking advantage of the energy stored in waves, small marine vehicles in general, have the potential for increased mission lengths and more efficient operation.

A quasi-steady mathematical model was presented where empirically determined force and moment coefficients were used to estimate the forces generated by the foil based on the dynamic angle of attack. The model demonstrates the benefits of an oscillating foil over a stationary one, and also allows a forward speed, or current velocity, to be considered. The model was augmented to account for added mass and wake effects, which serve to reduce the force magnitudes slightly. The models provided preliminary analysis into conditions resulting in positive thrust force development and guided parameter selection for the simulation and physical experiments.

Providing further analysis, the rigid body motion problem was implemented in Open-

FOAM, where the oscillatory motion was achieved using an AMI and the solver permitted linear gravity waves and a current velocity to be modelled. A DOE uniform design technique was employed to determine the influential factors and factor interactions on the horizontal, vertical and moment forces developed, and facilitated generation of a polynomial model equation. Among the factors investigated, it was found that forward speed and its 2FI with the hydrofoil pitch amplitude are the most significant factors, with wave frequency and its interaction with pitch amplitude also deemed significant. It was found that the forces generated using the mathematical model severely underestimated the numerically generated forces.

To provide comparison with the force magnitudes generated in the numerical model, an experimental hydrodynamic testing platform was designed and constructed. The hydrofoil was fabricated out of machined HDPE pieces and is controlled using a DC motor. The DC motor was installed within the foil, allowing the foil position to be directly measured underwater. The foil was attached between two aluminum struts, and fixed to the frame using low profile tension/compression load cells that measured the forces generated. The motor and load cells were characterized, and two control strategies were developed to test active and passive foil control. A CCD experimental design was selected, and ground truth tests were performed at fixed attack angles which generally agree with other empirical data, serving to validate the platform.

As in the numerical experiment, the physical experiment results were used to develop a model equation. A comparison with the numerical model indicates general agreement, however a tendency for the OpenFOAM model to over-predict forces is noted. Both models reveal that the moment force does not change enough to warrant a model, and that the mean value is the best predictor of moment. Lastly, the spring-mode control

strategy was implemented and further tests were run. Although similar motions to the prescribed mode were indeed achieved, no thrust was produced. A positive outcome is that the phase lag between the foil and the wave self-adjusts to 90°. It is anticipated that with further experimentation and tuning, similar results to the prescribed mode could be achieved.

Both numerical and experimental results demonstrated that thrust can be achieved in waves using an actively pitch-controlled hydrofoil. It was also demonstrated that DOE methodologies can be useful for generating models and providing comparison between simulation and experiment, without requiring the exact same runs to be performed. Before further testing, several improvements are recommended.

6.2 Experimental Recommendations & Future Works

Based on the physical experiments performed, the following upgrades are recommended.

1. An external encoder is needed for more accurate measurement of the hydrofoil pitch angle. Early in the testing, it was found that the zero position of the foil shifted slightly from run to run. For this reason, this position was reset after each run. By implementing an external encoder on one of the circular plates, this issued could be resolved.

2. To achieve the desired phase lag of 90 degrees between the foil and wave, the wave height was plotted in real-time on the control computer and the foil motions were started manually. While, in general, the phase lag remained near 90 degrees

(± 10 degrees), automating this procedure would greatly reduce the error and avoid reruns.

3. At several instances during the testing, it was noted that the encoder was not capturing small angle changes of the foil. This was determined to be an issue with the screwed connection between the motor adapter and the end cap. After experimenting unsuccessfully with Loctite adhesive, the end cap and motor adapter were welded together. This solved the problem and should be used for any further testing with the experimental platform.

4. Rather than relying on the calibration matrix to account for the cross talk effect between front and rear load cells, a modification to the front load cell arrangement should be performed such that they only measure vertical forces and the horizontal forces are measured by the rear load cells. This would provide a more reliable measurement of the forces.

5. On several occurrences, it was noted that the load cells gave unusual measurements which was due to loose connections to the signal conditions. Acquiring the appropriate dock for the signal conditioners would help in this regard.

In future works, it will be beneficial to test the system in a wider range of wave conditions and wave theories, preferably in conditions most representative of the North Atlantic region. This should also be done numerically. Furthermore, it will be interesting to see the changes when the foil is allowed to heave, which could be tested by devising a heave spring mechanism, or installing the foil on a model vessel and performing free-running tests. Lastly, consideration should be given to how the foil system could be installed aboard a small marine vehicle.

Bibliography

[1] "MOST (AV) Ltd unmanned marine systems," http://www.autonautusv.com/, accessed: 2017-09-30. ix, 3, 4

[2] D. Vrooman, "Vibrating propeller," *US Patent*, vol. 22, p. 097, 1858. ix, 4

[3] H. Linden, "Improved combination with floating bodies, of fins adapted to effect their propulsion," Patent, 1895. ix, 9

[4] J. Stroeve, M. M. Holland, W. Meier, T. Scambos, and M. Serreze, "Arctic sea ice decline: Faster than forecast," *Geophysical research letters*, vol. 34, no. 9, 2007. 1

[5] E. Carrig and S. Nguyen, "Wind, solar-powered asv self-righting catamaran datamaran surveys open water autonomously for long deployments," *SEA TECHNOLOGY*, vol. 55, no. 9, pp. 43–+, 2014. 3

[6] "ASV unmanned marine systems," https://www.asvglobal.com/, accessed: 2016-09-30. 3

[7] R. Hine, S. Willcox, G. Hine, and T. Richardson, "The wave glider: A wave-powered autonomous marine vehicle," in *OCEANS 2009, MTS/IEEE Biloxi-Marine Technology for Our Future: Global and Local Challenges*. IEEE, 2009, pp. 1–6. 3, 4

[8] C. Zheng, L. Shao, W. Shi, Q. Su, G. Lin, X. Li, and X. Chen, "An assessment of global ocean wave energy resources over the last 45 a," *Acta Oceanologica Sinica*, vol. 33, no. 1, pp. 92–101, 2014. 4

[9] Y. Terao, "Wave devouring propulsion system: from concept to trans-pacific voyage," in *ASME 2009 28th International Conference on Ocean, Offshore and Arctic Engineering*. American Society of Mechanical Engineers, 2009, pp. 119–126. 4

[10] K. Belibassakis and E. Filippas, "Ship propulsion in waves by actively controlled flapping foils," *Applied Ocean Research*, vol. 52, pp. 1–11, 2015. 4, 6

[11] N. Smith, Z. Li, R. Bachmayer, and F. Luchino, "Development of a semi-submersible unmanned surface craft," in *Oceans-St. John's, 2014*. IEEE, 2014, pp. 1–7. 5

[12] J. M. Benyus, "Biomimicry: Innovation inspired by nature," 2002. 5

[13] T. Y.-T. Wu, "Swimming of a waving plate," *Journal of Fluid Mechanics*, vol. 10, no. 3, pp. 321–344, 1961. 5

[14] M. Lighthill, "Note on the swimming of slender fish," *Journal of fluid Mechanics*, vol. 9, no. 2, pp. 305–317, 1960. 5

[15] M. Chopra, "Hydromechanics of lunate-tail swimming propulsion," *Journal of Fluid Mechanics*, vol. 64, no. 2, pp. 375–392, 1974. 6

[16] M. Chopra and T. Kambe, "Hydromechanics of lunate-tail swimming propulsion. part 2," *Journal of Fluid Mechanics*, vol. 79, no. 1, pp. 49–69, 1977. 6

[17] H. Yamaguchi and N. Bose, "Oscillating foils for marine propulsion," *Oscillating Foils for Marine Propulsion*, vol. 3, pp. 539–544, 1994. 6

[18] M. Murray and L. Howle, "Spring stiffness influence on an oscillating propulsor," *Journal of Fluids and Structures*, vol. 17, no. 7, pp. 915–926, 2003. 6

[19] J. Katz and D. Weihs, "Hydrodynamic propulsion by large amplitude oscillation of an airfoil with chordwise flexibility," *Journal of Fluid Mechanics*, vol. 88, no. 3, pp. 485–497, 1978. 6

[20] K. A. Harper, M. D. Berkemeier, and S. Grace, "Modeling the dynamics of spring-driven oscillating-foil propulsion," *IEEE Journal of Oceanic Engineering*, vol. 23, no. 3, pp. 285–296, 1998. 6

[21] X. Zhang, Y.-m. Su, L. Yang, and Z.-l. Wang, "Hydrodynamic performance of flapping-foil propulsion in the influence of vortices," *Journal of marine science and application*, vol. 9, no. 2, pp. 213–219, 2010. 6

[22] J. Anderson, K. Streitlien, D. Barrett, and M. Triantafyllou, "Oscillating foils of high propulsive efficiency," *Journal of Fluid Mechanics*, vol. 360, pp. 41–72, 1998. 6, 27

[23] D. A. Read, F. Hover, and M. Triantafyllou, "Forces on oscillating foils for propulsion and maneuvering," *Journal of Fluids and Structures*, vol. 17, no. 1, pp. 163–183, 2003. 6, 36

[24] E. Bøckmann, "Wave propulsion of ships," 2015. 7

[25] S. Licht, V. Polidoro, M. Flores, F. S. Hover, and M. S. Triantafyllou, "Design and projected performance of a flapping foil auv," *IEEE Journal of Oceanic Engineering*, vol. 29, no. 3, pp. 786–794, 2004. 7

[26] M. S. Triantafyllou, A. H. Techet, and F. S. Hover, "Review of experimental work in biomimetic foils," *IEEE Journal of Oceanic Engineering*, vol. 29, no. 3, pp. 585–594, 2004. 7

[27] T. Wu, "Extraction of flow energy by a wing oscillating in waves," Tech. Rep., 1971. 7, 13

[28] H. Isshiki, "A theory of wave devouring propulsion (1st report)," 日本造船学会論文集, vol. 1982, no. 151, pp. 54–64, 1982. 8

[29] ——, "A theory of wave devouring propulsion (2nd report)-optimized foil motions for a passive-type wave devouring propulsor," *J. Soc. Naval Arch. Japan*, vol. 152, 1982. 8

[30] N. Bose and J. Lien, "Energy absorption from ocean waves: a free ride for cetaceans," *Proceedings of the Royal Society of London B: Biological Sciences*, vol. 240, no. 1299, pp. 591–605, 1990. 8

[31] G. Politis and K. Politis, "Biomimetic propulsion under random heaving conditions, using active pitch control," *Journal of Fluids and Structures*, vol. 47, pp. 139–149, 2014. 8

[32] L. W. A. De Silva and H. Yamaguchi, "Numerical study on active wave devouring propulsion," *Journal of marine science and technology*, vol. 17, no. 3, pp. 261–275, 2012. 8, 36

[33] E. Esmaeilifar, M. H. Djavareshkian, B. F. Feshalami, and A. Esmaeili, "Hydrodynamic simulation of an oscillating hydrofoil near free surface in critical unsteady parameter," *Ocean Engineering*, vol. 141, pp. 227–236, 2017. 9

[34] Y. Terao and N. Sakagami, "Design and development of an autonomous wave-powered boat with a wave devouring propulsion system," *Advanced Robotics*, vol. 29, no. 1, pp. 89–102, 2015. 9

[35] E. Bøckmann and S. Steen, "Experiments with actively pitch-controlled and spring-loaded oscillating foils," *Applied Ocean Research*, vol. 48, pp. 227–235, 2014. 10

[36] J. Bowker, N. C. Townsend, M. Tan, and R. Shenoi, "Experimental study of a wave energy scavenging system onboard autonomous surface vessels (asvs)," in *OCEANS 2015-Genova*. IEEE, 2015, pp. 1–9. 10

[37] B. J. Simpson, S. Licht, F. S. Hover, and M. S. Triantafyllou, "Energy extraction through flapping foils," in *ASME 2008 27th International Conference on Offshore Mechanics and Arctic Engineering*. American Society of Mechanical Engineers, 2008, pp. 389–395. 10

[38] F. Hover, Ø. Haugsdal, and M. Triantafyllou, "Effect of angle of attack profiles in flapping foil propulsion," *Journal of Fluids and Structures*, vol. 19, no. 1, pp. 37–47, 2004. 10, 36

[39] I. Yamamoto, Y. Terada, T. Nagamatu, and Y. Imaizumi, "Propulsion system with flexible/rigid oscillating fin," *IEEE Journal of Oceanic engineering*, vol. 20, no. 1, pp. 23–30, 1995. 10

[40] T. S. Garrison, *Oceanography: an invitation to marine science*. Cengage Learning, 2015. 13

[41] T. Perez, *Ship motion control: course keeping and roll stabilisation using rudder and fins*. Springer Science & Business Media, 2006. 13

[42] MATLAB, *version 7.10.0 (R2010a)*. Natick, Massachusetts: The MathWorks Inc., 2010. 15, 23

[43] R. G. Dean and R. A. Dalrymple, *Water wave mechanics for engineers and scientists*. World Scientific Publishing Company, 1991, vol. 2. 18

[44] O. Faltinsen, *Sea loads on ships and offshore structures*. Cambridge university press, 1993, vol. 1. 18

[45] Y. C. Fung, *An introduction to the theory of aeroelasticity*. Courier Dover Publications, 2008. 22

[46] R. E. Sheldahl and P. C. Klimas, "Aerodynamic characteristics of seven symmetrical airfoil sections through 180-degree angle of attack for use in aerodynamic analysis of vertical axis wind turbines," Sandia National Labs., Albuquerque, NM (USA), Tech. Rep., 1981. 23, 104

[47] J. N. Newman, *Marine hydrodynamics*. MIT press, 1977. 29

[48] T. Theodorsen, "General theory of aerodynamic instability and the mechanism of flutter," 1949. 30

[49] G. J. Leishman, *Principles of helicopter aerodynamics with CD extra*. Cambridge university press, 2006. 30, 31

[50] S. Lapointe and G. Dumas, "Numerical simulations of self-sustained pitch–heave oscillations of a naca 0012 airfoil," in *20th Annual Conference of the CFD Society of Canada*, 2012. 36

[51] H. G. Weller, G. Tabor, H. Jasak, and C. Fureby, "A tensorial approach to computational continuum mechanics using object-oriented techniques," *Computers in physics*, vol. 12, no. 6, pp. 620–631, 1998. 40

[52] J. H. Ferziger and M. Peric, *Computational methods for fluid dynamics*. Springer Science & Business Media, 2012. 42

[53] P. Higuera, J. L. Lara, and I. J. Losada, "Realistic wave generation and active wave absorption for navier–stokes models: Application to openfoam®," *Coastal Engineering*, vol. 71, pp. 102–118, 2013. 42, 51

[54] C. W. Hirt and B. D. Nichols, "Volume of fluid (vof) method for the dynamics of free boundaries," *Journal of computational physics*, vol. 39, no. 1, pp. 201–225, 1981. 44

[55] C. J. Greenshields, "Openfoam user guide," *OpenFOAM Foundation Ltd, version*, vol. 3, no. 1, 2015. 47

[56] R. Mehdipour, "Simulating propeller and propeller-hull interaction in openfoam," 2014. 50

[57] V. Mishra, S. Beatty, B. Buckham, P. Oshkai, and C. Crawford, "Application of an arbitrary mesh interface for cfd simulation of an oscillating wave energy converter," in *Proc. 11th Eur. Wave Tidal Energy Conf*, 2015, pp. 07B141–07B1410. 50

[58] F. Menter, "Zonal two equation kw turbulence models for aerodynamic flows," in *23rd fluid dynamics, plasmadynamics, and lasers conference*, 1993, p. 2906. 54

[59] N. Vaughn, C. Polnaszek *et al.*, "Design-expert® software," *Stat-Ease, Inc, Minneapolis, MN*, 2007. 55

[60] V. Czitrom, "One-factor-at-a-time versus designed experiments," *The American Statistician*, vol. 53, no. 2, pp. 126–131, 1999. 55

[61] H. Pham, *Springer handbook of engineering statistics*. Springer Science & Business Media, 2006. 56

[62] K.-T. Fang, "Uniform design: application of number-theoretic methods in experimental design," *Acta Math. Appl. Sin.*, vol. 3, pp. 363–372, 1980. 56

[63] Y. Wang and K. FANG, "A note on uniform distribution and experimental design," in *Selected Papers Of Wang Yuan*. World Scientific, 2005, pp. 417–421. 56

[64] K.-T. Fang, R. Li, and A. Sudjianto, *Design and modeling for computer experiments*. CRC Press, 2005. 56

[65] T. Schnipper, A. Andersen, and T. Bohr, "Vortex wakes of a flapping foil," *Journal of Fluid Mechanics*, vol. 633, pp. 411–423, 2009. 75

[66] R. Godoy-Diana, J.-L. Aider, and J. E. Wesfreid, "Transitions in the wake of a flapping foil," *Physical Review E*, vol. 77, no. 1, p. 016308, 2008. 75

[67] G. W. Johnson, *LabVIEW graphical programming*. Tata McGraw-Hill Education, 1997. 89

[68] R. H. Myers, D. C. Montgomery, and C. M. Anderson-Cook, *Response surface methodology: process and product optimization using designed experiments*. John Wiley & Sons, 2016. 102

A Mathematical Model

```
%Augmented unsteady model − foil assisted propulsion
%Author: Matt Gauthier
%Date: June 1st, 2016
%Description: Resolve resultant forces on foil into horizontal and
%vertical components. Include added mass and wake effects.

clear
clc;
format short
close all;

%Constants
a = 0.03; %wave amplitude
g = 9.81; %gravity
T_period = 3.3333333; %wave period
rho = 1000; %fluid density
c = 0.25; %chord length
span = 1; %foil span
t = 0:0.02:15*T_period;
z = −0.6; %submergence
x = 0; %horizontal position
F_amp = 20*pi/180; %foil pitch amplitude
initial = 3*pi/2; %initial phase
phaseLag = 90*pi/180; %phase lag between wave and foil
del_t = 1;
nu = .00000183; %dynamic viscosity
b = c/2; %mid−chord
Uc = 0.4; %current velocity

%dependent parameters
A_proj = c * span; %projected area
```

```
flatArea = A_proj; %flat area
omega = 2*pi/T_period; %angular frequency
k = omega^2/g; %wave number
lamda = g/(2*pi) * T_period^2; %wave length
AR = span/c; %aspect ratio
a_1 = -1/2; %pivot point (THIS IS MEASURED IN HALF-CHORDS!)
added_mass = rho * pi/8 * (c/2)^4; %added mass of flat plate

%Import Aerodynamic data for NACA 0015 (Re: 360000)
%NB. angles in radians!%

% A = csvread('Flat_plate_AR_2.5.csv');
A = csvread('NACA0015_lift_drag_RE36e4.csv');
B = csvread('NACA_0015_moment_RE36e6.csv');

%Parse Data

alfa = A(:,1);
cL1 = A(:,2);
cD1 = A(:,3);
alfa_m = B(:,1);
cM = B(:,2);

%Plot and determine appropriate order curve fit

% figure
% scatter(alfa, cL1);
% xlabel('Angle of Attack')
% ylabel('cL, cD')
% hold on
% scatter(alfa, cD1);
```

```
% set(gcf,'Color', 'w');
% grid on
% legend('cL', 'cD')

%Determine fourier coefficients for cL, cD

P1 = fit(A(:,1), A(:,2), 'fourier8'); %order determined from above
P2 = fit(A(:,1), A(:,3), 'fourier4');
P3 = fit(B(:,1), B(:,2), 'fourier8');

Forces2 = {0};



for time = 1:numel(t)

    %foil angle
    phi(time) = F_amp * sin((omega * t(time) + phaseLag)); %Lag is based on initial
        ↪ definition


    %flow condition
profile(time) = a*sin(omega*t(time) - k*x);
u = omega*a*exp(k*z)*sin((omega*time - k*x - phaseLag));
w = omega*a*exp(k*z)*cos((omega*time - k*x - phaseLag));

U = [-u; w; zeros(size(u))];
V = (norm(U));
Ucomb = U + Uc;
uMag = norm(Ucomb);

%Conditional Statements to control the wave + current resultant vector direction%
if Uc(1,:)/V > 1
```

```
    var = 1;
    var2 = 0;
    initial = 0;
else
    var = 0;
    var2 = 1;
    startAngle = acos(V/sqrt(V^2 + Uc(1,:)^2));
end

combinedWavePhase(time) = (var2*(omega * t(time)) + initial + startAngle + var*(pi/2 -(acos(
    ↪ V/sqrt(V^2 + Uc(1,:)^2))))* cos(omega*t(time)+pi));

        n(time) = ((2*pi)+abs((combinedWavePhase(time))))/(2*pi);
        rev(time) = abs(floor(n(time)))-1;

        if combinedWavePhase(time) > 2*pi
            combinedWavePhase(time) = (combinedWavePhase(time) - rev(time)*2*pi);
        elseif combinedWavePhase(time) < 0
            combinedWavePhase(time) = combinedWavePhase(time) + 2*pi;
        else
            combinedWavePhase(time);
        end

        %Define the angle of attack
        alfa_eff(time) = (combinedWavePhase(time) + phi(time));

        if alfa_eff(time) < 0
            alfa_eff(time) = alfa_eff(time) + 2*pi;
        else
            alfa_eff(time);
        end
```

```
%Below we now have coefficients for every AoA
cL_Sheldahl(time) = P1(alfa_eff(time));
cL_Sheldahl(cL_Sheldahl < 0) = 0;
cD_Sheldahl(time) = P2(alfa_eff(time));
cM_Sheldahl(time) = P3(alfa_eff(time));


        %%foil angular velocity%%
        if time == 1
        del_alfa_eff(time) = (alfa_eff(time))/(del_t);
        else
        del_alfa_eff(time) = (alfa_eff(time)-alfa_eff(time-1))/(del_t);
        end

        %%Foil angular acceleration%%
        if time == 1
        ddel_alfa_eff(time) = (del_alfa_eff(time))/(del_t);
        else
        ddel_alfa_eff(time) = (del_alfa_eff(time) - del_alfa_eff(time-1))/(del_t);
        end

%%Define Theodorsen Deficiency Function%%

        red_k = (omega * c)/(2 * (uMag));
        F_k = (besselj(1, red_k)*(((besselj(1, red_k))+bessely(0, red_k))) + bessely(1, red_k)
            ↪ *(bessely(1, red_k)-besselj(0, red_k)))/...
                    (((besselj(1, red_k) + bessely(0, red_k)))^2 + (besselj(0, red_k) - bessely
                        ↪ (1, red_k))^2);

        G_k = -(((bessely(1, red_k) * bessely(0, red_k)) + (besselj(1, red_k) * besselj(0, red_k
            ↪ )))/...
```

```
(((besselj(1, red_k) + bessely(0, red_k)))^2 + (besselj(0, red_k) - bessely(1,
    ↪ red_k))^2));

THEO_deficiency = F_k + i*G_k;



%%Theordorsen Lift and Moment%%

Theo_lift = 0.5 * rho * uMag^2 * A_proj * cL_Sheldahl(time)* THEO_deficiency;
Theo_drag = 0.5 * rho * uMag^2 * A_proj * cD_Sheldahl(time);
Z = zeros(size(Theo_lift));

%This accounts for the change in the lift force
rotPhase(time) = omega*t(time);
rev2(time) = floor((omega*t(time))/(2*pi));

if rotPhase(time)-rev2(time)*2*pi > pi/2
    Theo_lift = -Theo_lift;
end
if rotPhase(time)-rev2(time)*2*pi > pi
    Theo_lift = -Theo_lift;
end
if rotPhase(time)-rev2(time)*2*pi > 3*pi/2
    Theo_lift = -Theo_lift;
end

if rotPhase(time)-rev2(time)*2*pi < pi/2
    Theo_lift = Theo_lift;
end
```

```
%This accounts for positive or negative lift to start
if (2*pi - combinedWavePhase(1)) > F_amp
    Forces1 = [Theo_drag -real(Theo_lift) Z]';
else
    Forces1 = [Theo_drag real(Theo_lift) Z]';
end


%Rotation matrix to return forces to the earth fixed coordinate system
earthFixed = [cos(combinedWavePhase(time)) -sin(combinedWavePhase(time)) 0;sin(
    ↪ combinedWavePhase(time)) cos(combinedWavePhase(time)) 0; 0 0 1];
Forces2(time) = {earthFixed * Forces1};

Moment(time) = ((0.5 * rho * A_proj * Ucomb(1,:)^2 * c^2 * cM_Sheldahl(time) *
    ↪ THEO_deficiency) + (added_mass * (ddel_alfa_eff(time)) * c/4));
%Only due to added?mass effects if the pivot is at c/4!!AM_trans = Forces2(1,:);
end

Res_forces = cell2mat(Forces2);


avgM = mean(real(Moment));
X = -Res_forces(1,:);
avgX = mean(real(X));
Y = Res_forces(2,:);
avgY = mean(Y);
thrust_coeff = smooth(real(X))/(0.5 * rho * A_proj * ((Uc(1,:))^2));
vert_coeff = smooth(real(Y))/(0.5 * rho * A_proj * ((Uc(1,:))^2));
moment_coeff = smooth(real(Moment))/(0.5 * rho * A_proj * ((Uc(1,:))^2) * c);
```

```
%Plot forces%

set(0,'DefaultAxesColorOrder', linspecer(8));
N = 6;
C = linspecer(N);

figure
subplot(5,1,1)
plot(t/T_period, profile, 'color',C(1,:), 'LineStyle', '-', 'Marker', 'o','MarkerSize', 3)
xlim([1 5]);
set(gca,'FontSize', 16)
grid on
ylabel('\eta [m]')
subplot(5,1,2)
plot(t/T_period, phi, 'color',C(2,:), 'LineStyle', '-', 'Marker', '<','MarkerSize', 3)
xlim([1 5]);
set(gca,'FontSize', 16)
grid on
ylabel('\phi [rad]')
subplot(5,1,3)
plot(t/T_period, real(X), 'color','k', 'LineStyle', '-', 'Marker', '*','MarkerSize', 1)
hold on
mean1 = mean(thrust_coeff);
meanstr1 = num2str(mean1);
mean2 = mean(vert_coeff);
meanstr2 = num2str(mean2);
plot(t/T_period, ones(size(thrust_coeff)) * mean1, 'g-.')
xlim([1 5]);
set(gca,'FontSize', 16)
ylabel('F_{x} [N]')
```

```
grid on
hold on
subplot(5,1,4)
plot(t/T_period, real(Y),'color', 'k', 'LineStyle', '-', 'Marker', 's','MarkerSize', 1)
grid on
set(gca,'FontSize', 16)
ylabel('F_{z} [N]')
hold on
plot(t/T_period, ones(size(vert_coeff)) * mean2, 'm-.')
xlim([1 5]);
subplot(5,1,5)
plot(t/T_period, Moment, 'color', 'k', 'LineStyle', '-', 'Marker', 'd', 'MarkerSize', 1)
xlim([1 5]);
grid on
set(gca,'FontSize', 16)
set(gcf,'Color', 'w');
xlabel('t/T')
ylabel('M [Nm] ')
```

B OpenFoam Files

ControlDict

```
FoamFile
{
    version 2.0;
    format ascii;
    class dictionary;
    location "system";
    object controlDict;
}
// * * * * * * * * * * * * * * * * * * * * * * * * * * * * * * * * * * * * * * * * * * * * //
libs
(
        "libwaveGeneration.so"
        "libwaveAbsorption.so"
);

application olaDyMFoam;

startFrom latestTime;

startTime 0;

stopAt endTime;

endTime 20;

deltaT 0.001;

writeControl adjustableRunTime;
```

```
writeInterval 0.05;

purgeWrite 0;

writeFormat binary;

writePrecision 6;

writeCompression off;

timeFormat general;

timePrecision 6;

runTimeModifiable true;

adjustTimeStep yes;

maxCo 0.99;
maxAlphaCo 0.1;
maxDeltaT 0.025;

functions
{
    forces
    {
        type forces; // use the forces class
        functionObjectLibs ("libforces.so"); // "plugin" library to load
        patches (wing); // Name of patches to integrate forces
        outputControl timeStep; // When to write the output
```

```
        rhoName rho; // Name of the reference density
        rhoInf 1000; // Reference density for fluid
        CofR (0 −0.5 0); // Origin for moment calculations
        log true;
        liftDir (0 0 1);
        dragDir (1 0 0);
    }

    forceCoeffs
    {
        type forceCoeffs;
        libs ( "libforces.so" );
        writeControl timeStep;
        writeInterval 1;
        patches ( wing );
        rho rhoInf;
        log true;
        rhoInf 1000;
        liftDir (0 0 1);
        dragDir (1 0 0); //recall a negative drag coeff = desired
        CofR (0 1 0);
        pitchAxis (0 1 0);
        magUInf 0.5;//free stream velocity ... zero?
        lRef 0.25; //check
        Aref 0.25;//check
    }
}
```

DynamicMeshDict

```
FoamFile
{
    version 2.0;
    format ascii;
    class dictionary;
    object dynamicMeshDict;
}
// * * * * * * * * * * * * * * * * * * * * * * * * * * * * * * * * * * * * * * * * * * * * //

{
 dynamicFvMesh solidBodyMotionFvMesh;
 solidBodyMotionFvMeshCoeffs

{
        cellZone rotor;
        solidBodyMotionFunction oscillatingRotatingMotion;
        oscillatingRotatingMotionCoeffs
        {
            origin (0 -0.5 0);
            amplitude (0 -10 0); //units of rad
            omega 3.301714603; //units of rad/s [encounter frequency]
        }
}
}
// * * * * * * * * * * * * * * * * * * * * * * * * * * * * * * * * * * * * * * * * * * * * //
```

WaveDict

```
FoamFile
{
    version 2.0;
    format ascii;
    class dictionary;
    location "constant";
    object waveDict;
}
// * * * * * * * * * * * * * * * * * * * * * * * * * * * * * * * * * * * * * * * * * * * * //

waveType regular;

waveTheory StokesI;

genAbs 1;

absDir 0.0;

nPaddles 1;

waveHeight 0.05;

wavePeriod 1.90300679;

waveDir 0.0;

wavePhase 3.619114737;
```

```
uCurrent (0. 0. 0.);
// ********************************************************************** //
```

U

```
FoamFile
{
    version 2.0;
    format ascii;
    class volVectorField;
    location "0";
    object U;
}
// * * * * * * * * * * * * * * * * * * * * * * * * * * * * * * * * * * * * * * * * * * * * //

#include "include/initialConditions"

dimensions [0 1 −1 0 0 0 0];

internalField uniform (0 0 0);

boundaryField
{
   inlet
   {
        type waveVelocity;
        waveDictName waveDict;
        value uniform (0 0 0);
   }

    outlet
    {
        type waveAbsorption2DVelocity;
```

```
        uCurrent (0 0 0);
        value uniform (0 0 0);
    }

    top
    {
        type pressureInletOutletVelocity;
        tangentialVelocity uniform (0 0 0);
        value uniform (0 0 0);
    }

    wing
    {
        type movingWallVelocity;
        value uniform (0 0 0);
    }

    bottom
    {
        type slip;
    }

    front
    {
        type empty;
    }

    back
    {
        type empty;
    }
```

```
    AMIinner
    {
        type cyclicAMI;
        value $internalField;
    }

    AMIouter
    {
        type cyclicAMI;
        value $internalField;
    }
}
// ************************************************************************* //
```

C Experimental Test Platform Design Drawings

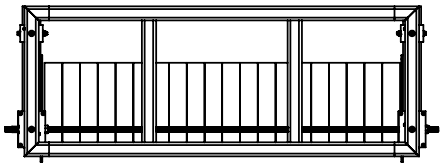

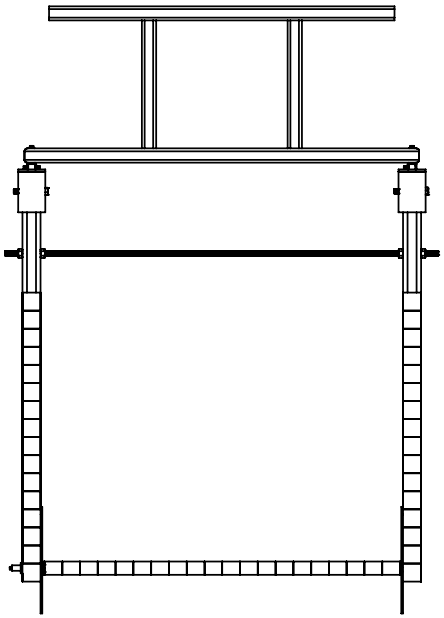

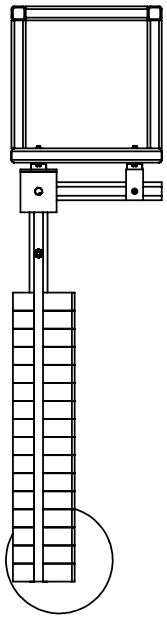

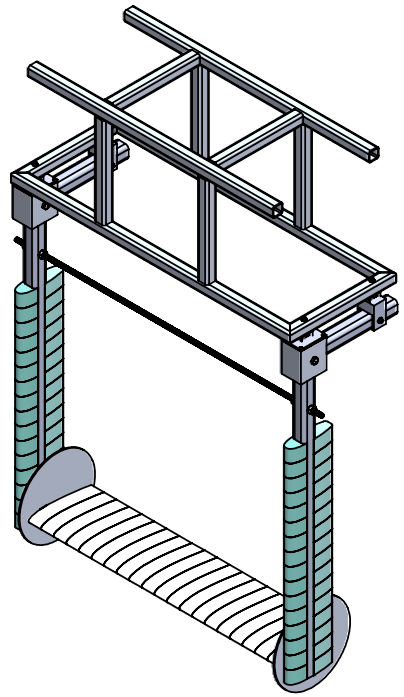

UNLESS OTHERWISE SPECIFIED: DIMENSIONS ARE IN: mm [Inches] SURFACE FINISH: TOLERANCES: LINEAR: ANGULAR:	Memorial University of Newfoundland Autonomous Ocean Systems Laboratory	DEBURR AND BREAK SHARP EDGES		NAME	SIGNATURE	DATE	PROJECT expDesign	REVISION:	
		MATERIAL: Various	DRAWN	Matt Gauthier		18.03.2017	TITLE: PLATFORM_ASM	SCALE:1:50	
		QUANTITY:	CHK'D				DWG NO. MTMG-01	SHEET 1 OF 18	A4

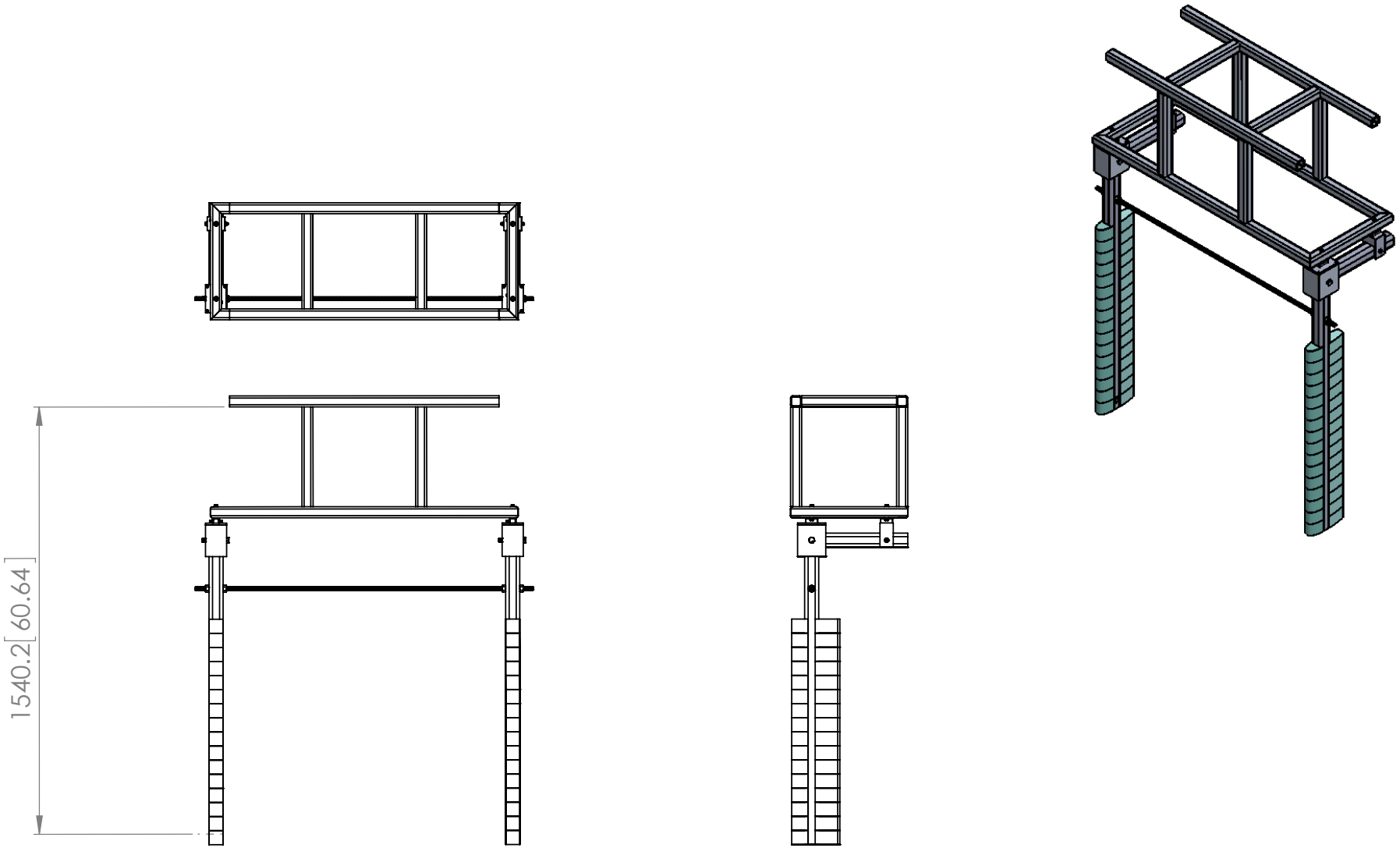

UNLESS OTHERWISE SPECIFIED:
DIMENSIONS ARE IN: mm [Inches]
SURFACE FINISH:
TOLERANCES:
LINEAR:
ANGULAR:

Memorial University of Newfoundland

Autonomous Ocean Systems Laboratory

DEBURR AND BREAK SHARP EDGES

		NAME	SIGNATURE	DATE
MATERIAL: Various	DRAWN	Matt Gauthier		18.03.2017
QUANTITY:	CHK'D			

PROJECT: expDesign
TITLE: FRAME_ASM
DWG NO. MTMG-02
REVISION:
SCALE:1:20
SHEET 2 OF 18
A4

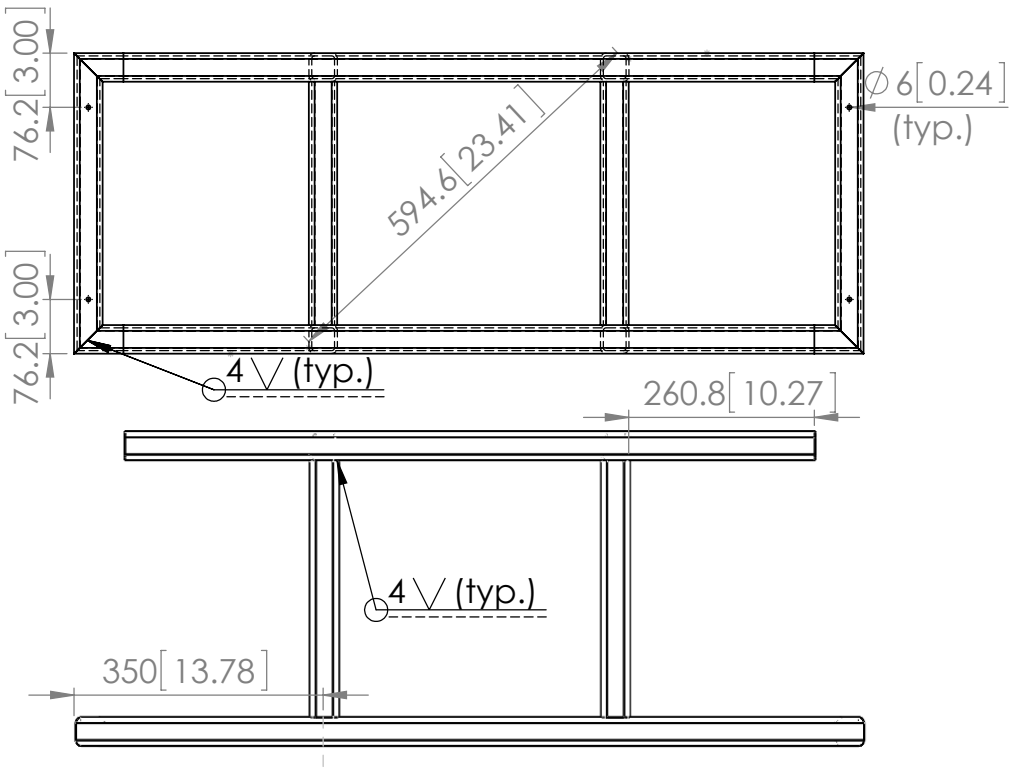

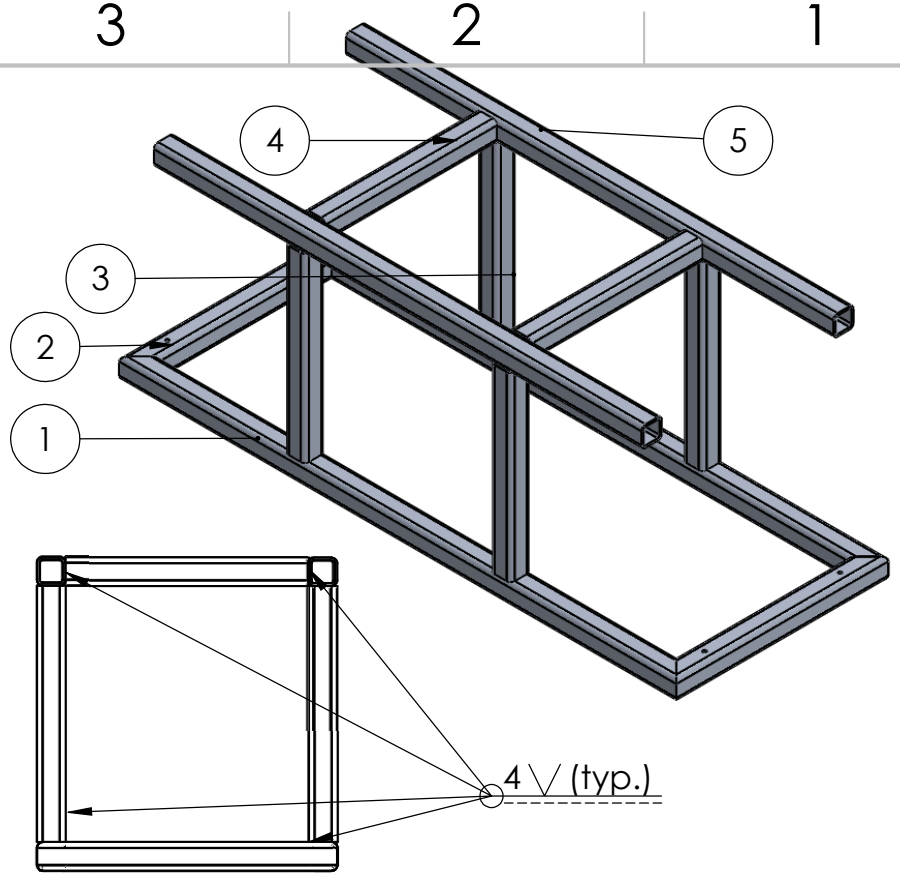

ITEM NO.	QTY.	DESCRIPTION	LENGTH
1	2	TUBE, SQUARE 40 X 40 X 4	1110
2	2	TUBE, SQUARE 40 X 40 X 4	422.4
3	4	TUBE, SQUARE 40 X 40 X 4	360
4	2	TUBE, SQUARE 40 X 40 X 4	342.4
5	2	TUBE, SQUARE 40 X 40 X 4	971.55

UNLESS OTHERWISE SPECIFIED:
DIMENSIONS ARE IN: mm [Inches]
SURFACE FINISH:
TOLERANCES:
LINEAR:
ANGULAR:

Memorial University of Newfoundland

Autonomous Ocean Systems Laboratory

DEBURR AND BREAK SHARP EDGES

MATERIAL: Alum. 6061

QUANTITY:

	NAME	SIGNATURE	DATE
DRAWN	Matt Gauthier		18.03.2017
CHK'D			

PROJECT expDesign

TITLE: tubularFrame_2

DWG NO. MTMG-03

REVISION:

SCALE:1:10

SHEET 3 OF 18

A4

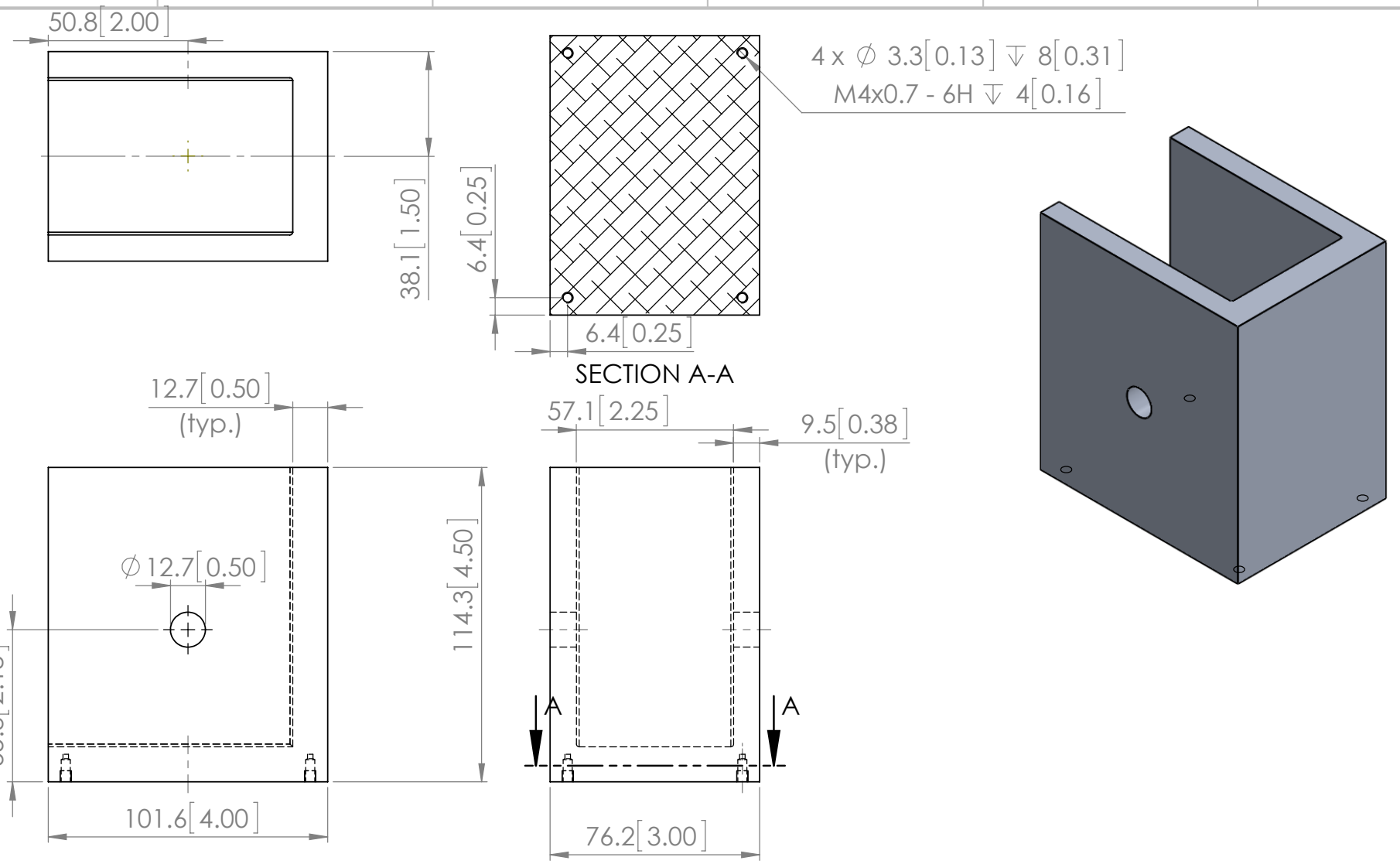

UNLESS OTHERWISE SPECIFIED: DIMENSIONS ARE IN: mm [Inches] SURFACE FINISH: TOLERANCES: LINEAR: ANGULAR:	Memorial University of Newfoundland Autonomous Ocean Systems Laboratory	DEBURR AND BREAK SHARP EDGES		NAME	SIGNATURE	DATE	PROJECT expDesign	REVISION:	
		MATERIAL: Al. 6061	DRAWN	Matt Gauthier		18.03.2017	TITLE: hingeMountingPlate	SCALE:1:2	
		QUANTITY:	CHK'D				DWG NO. MTMG-04	SHEET 4 of 18	A4

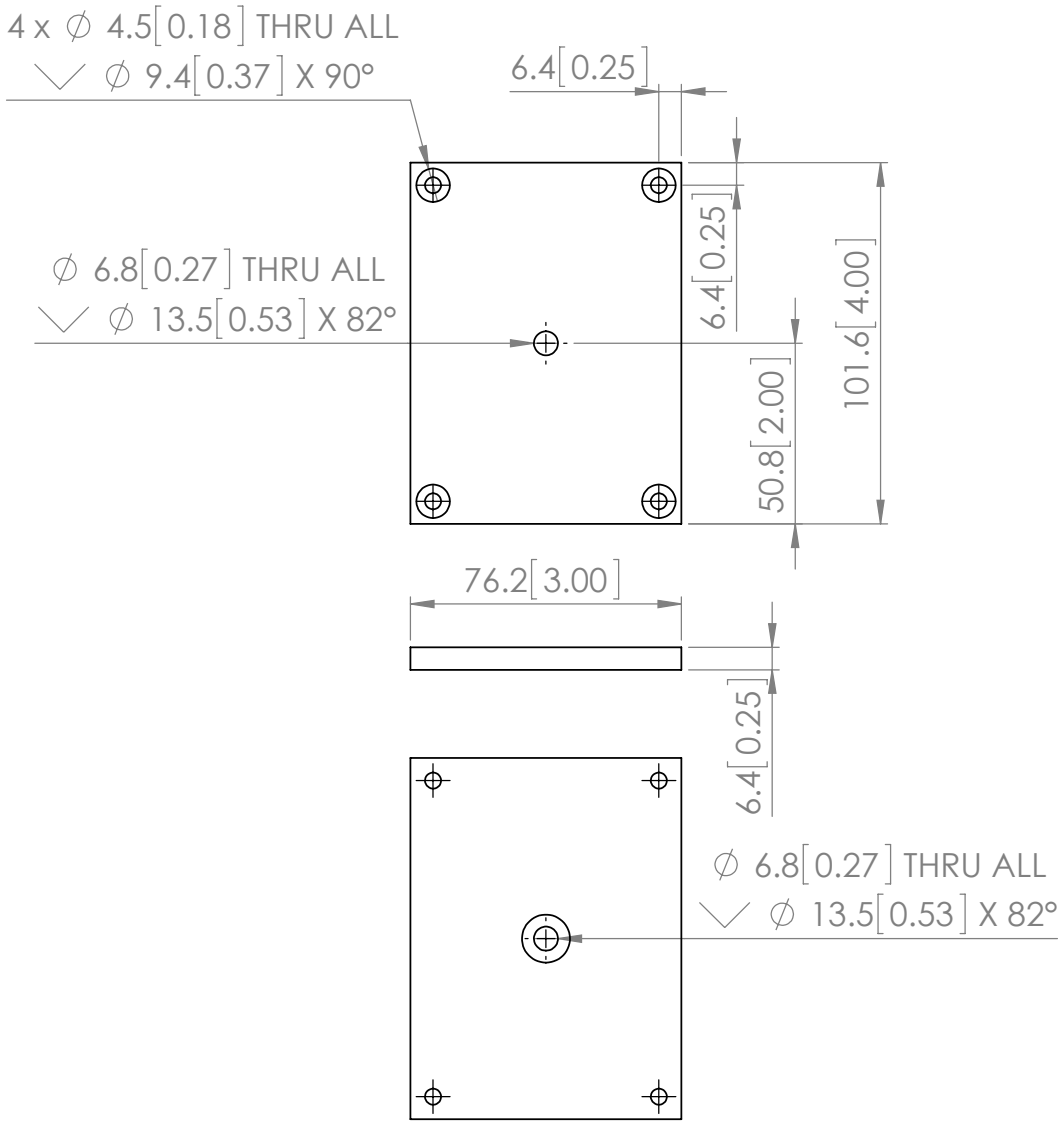

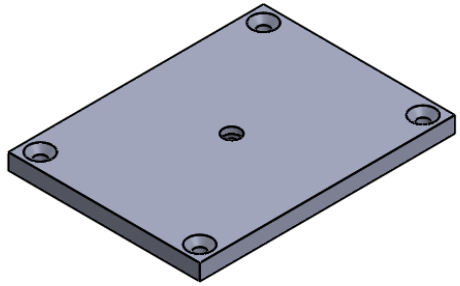

UNLESS OTHERWISE SPECIFIED: DIMENSIONS ARE IN: mm [Inches] SURFACE FINISH: TOLERANCES: LINEAR: ANGULAR:	Memorial University of Newfoundland Autonomous Ocean Systems Laboratory	DEBURR AND BREAK SHARP EDGES		NAME	SIGNATURE	DATE	PROJECT: expDesign	REVISION:
		MATERIAL: Al. 6061	DRAWN	Matt Gauthier		18.03.2017	TITLE: loadCellAttachment	SCALE:1:2
		QUANTITY:	CHK'D				DWG NO. MTMG-05	SHEET 5 OF 18 A4

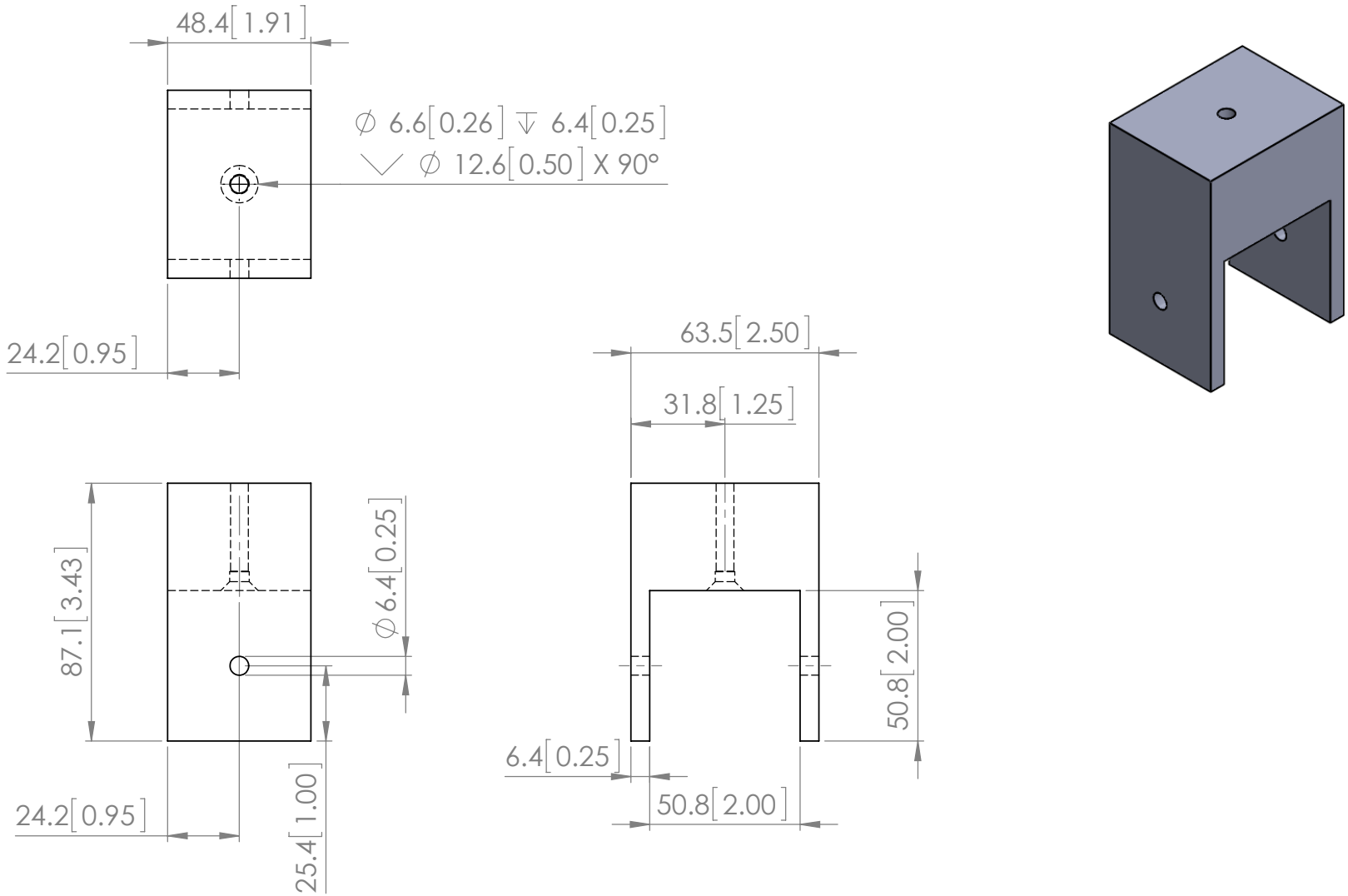

UNLESS OTHERWISE SPECIFIED: DIMENSIONS ARE IN: mm [Inches] SURFACE FINISH: TOLERANCES: LINEAR: ANGULAR:	Memorial University of Newfoundland Autonomous Ocean Systems Laboratory	DEBURR AND BREAK SHARP EDGES		NAME	SIGNATURE	DATE	PROJECT: expDesign	REVISION:
		MATERIAL: Al. 6061	DRAWN	Matt Gauthier		18.03.2017	TITLE: boosterPlate	SCALE:1:1
		QUANTITY:	CHK'D				DWG NO. MTMG-06	SHEET 6 of 18 A4

ITEM NO.	QTY.	DESCRIPTION	LENGTH
1	1	TUBE, SQUARE 50.80 X 50.80 X 6.35	1123
2	1	TUBE, SQUARE 50.80 X 50.80 X 6.35	333.5

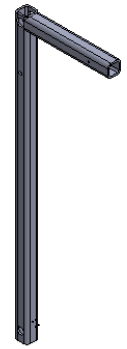

nB. Where no dimension given, holes to be centered on tubing.

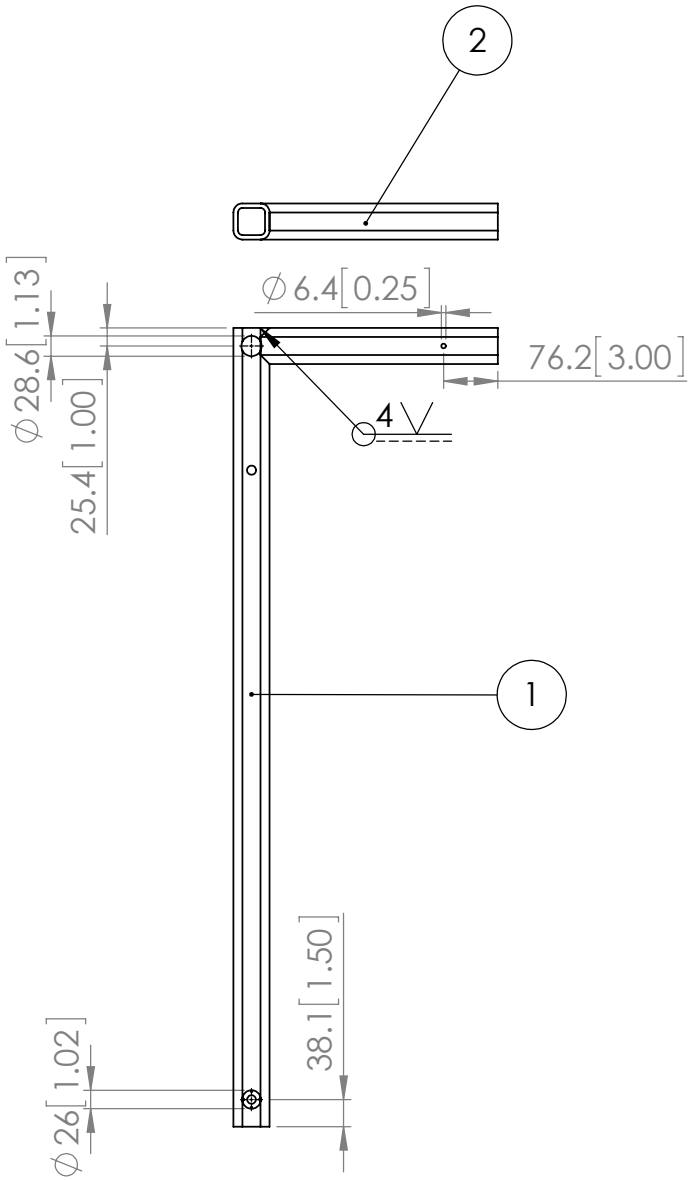

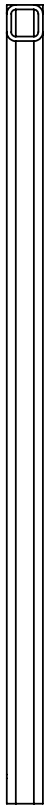

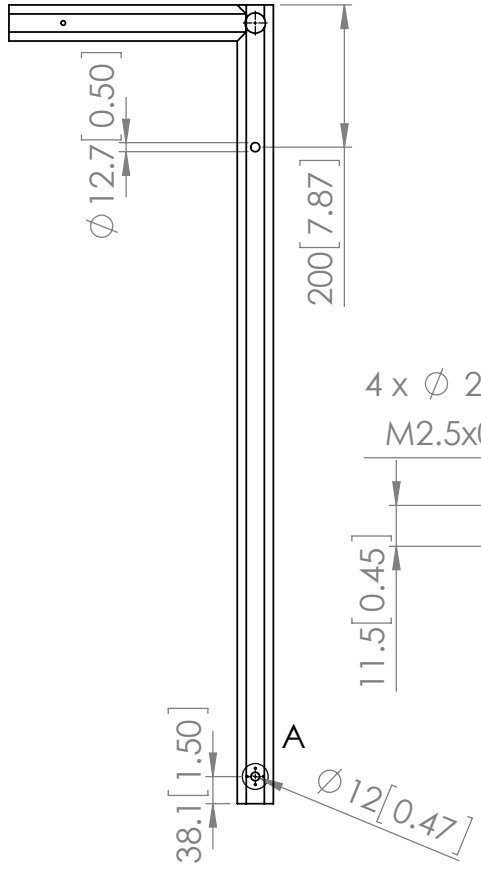

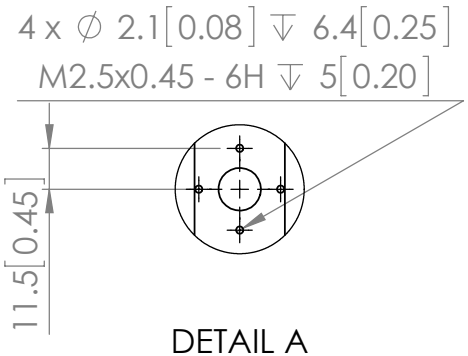

DETAIL A
SCALE 1 : 2

UNLESS OTHERWISE SPECIFIED:
DIMENSIONS ARE IN: mm [Inches]
SURFACE FINISH:
TOLERANCES:
LINEAR:
ANGULAR:

Memorial University of Newfoundland

Autonomous Ocean Systems Laboratory

DEBURR AND BREAK SHARP EDGES

		NAME	SIGNATURE	DATE
MATERIAL:	Al. 6061	DRAWN	Matt Gauthier	09.04.2017
QUANTITY:		CHK'D		

PROJECT	expDesign
TITLE:	LStrut
DWG NO.	MTMG-07
REVISION:	2.1
SCALE:1:20	
SHEET 7 0f 18	A4

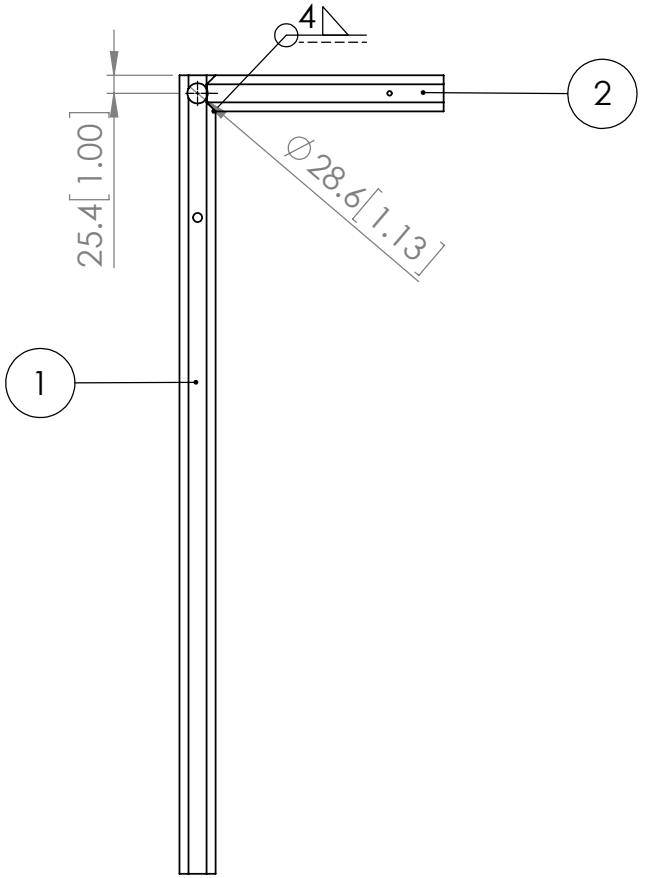

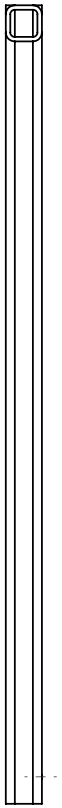

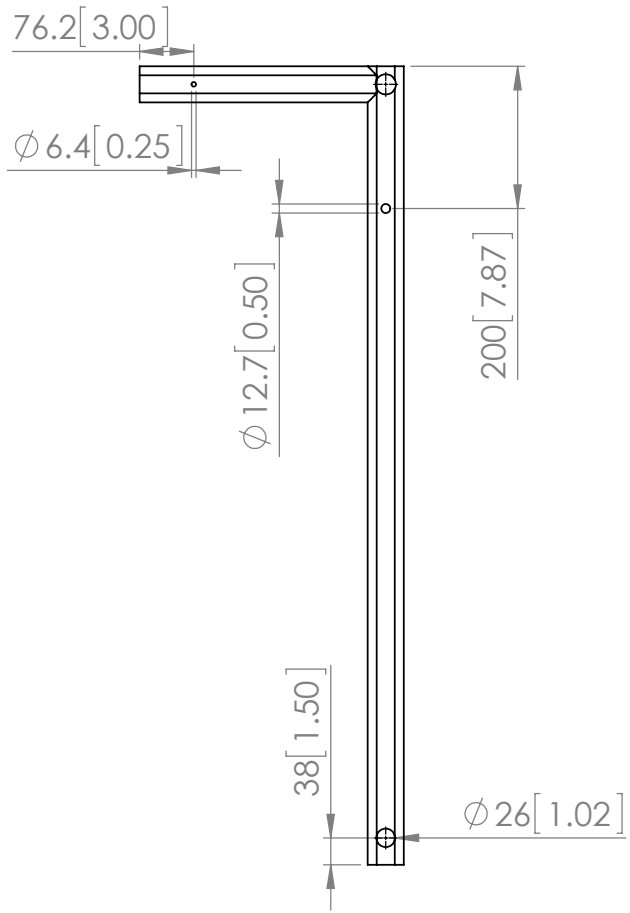

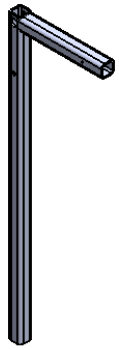

nB. Where no dimension given, holes to be centered on tubing.

Weldment Cut List			
ITEM NO.	QTY.	DESCRIPTION	LENGTH
1	1	TUBE, SQUARE 50.80 X 50.80 X 6.35	1123
2	1	TUBE, SQUARE 50.80 X 50.80 X 6.35	333.5

UNLESS OTHERWISE SPECIFIED:
DIMENSIONS ARE IN: mm [Inches]
SURFACE FINISH:
TOLERANCES:
LINEAR:
ANGULAR:

Memorial University of Newfoundland

Autonomous Ocean Systems Laboratory

DEBURR AND BREAK SHARP EDGES

		NAME	SIGNATURE	DATE
MATERIAL:	Al. 6061	DRAWN	Matt Gauthier	09.04.2017
QUANTITY:		CHK'D		

PROJECT: expDesign
TITLE: strut
DWG NO. MTMG-08
REVISION:
SCALE:1:10
SHEET 8 OF 18
A4

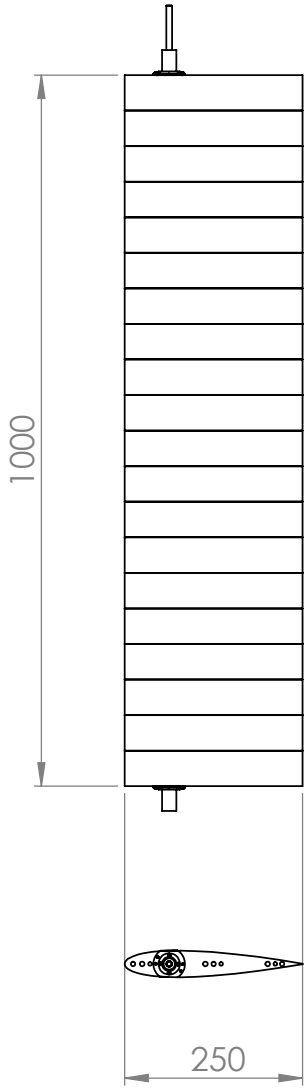

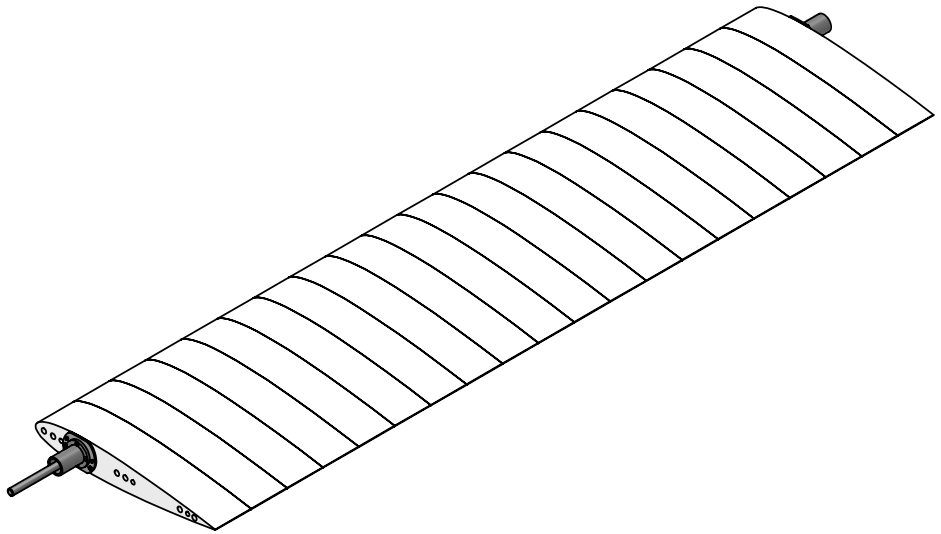

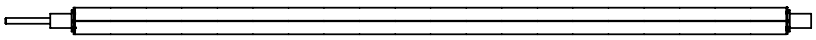

UNLESS OTHERWISE SPECIFIED: DIMENSIONS ARE IN: mm [Inches] SURFACE FINISH: TOLERANCES: LINEAR: ANGULAR:	Memorial University of Newfoundland Autonomous Ocean Systems Laboratory	DEBURR AND BREAK SHARP EDGES		NAME	SIGNATURE	DATE	PROJECT expDesign	REVISION:	
		MATERIAL: Various	DRAWN	Matt Gauthier		24.08.2016	TITLE: FOIL_ASM1	SCALE:1:10	
		QUANTITY:	CHK'D				DWG NO.	SHEET 1 OF 1	A4

DETAIL A
SCALE 1 : 5

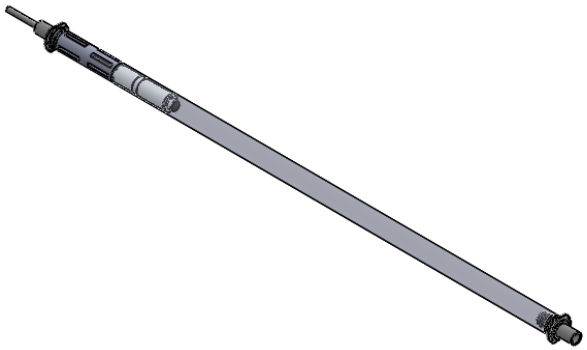

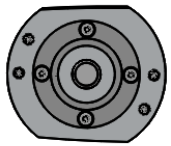

DETAIL B
SCALE 1 : 2

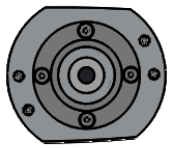

DETAIL C
SCALE 1 : 2

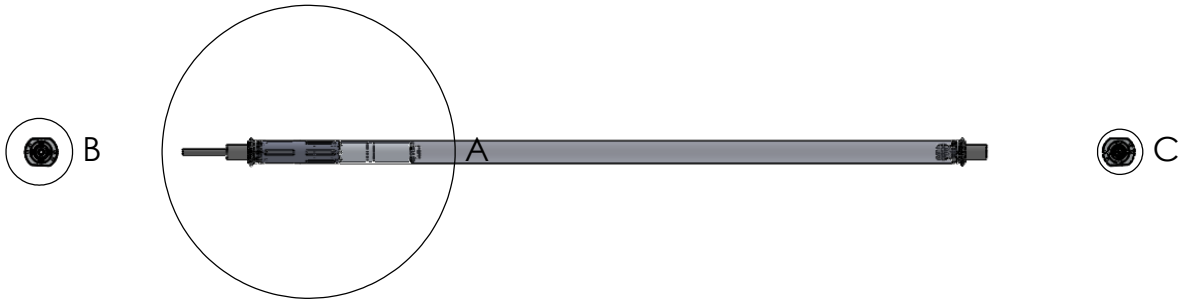

UNLESS OTHERWISE SPECIFIED: DIMENSIONS ARE IN: mm [Inches] SURFACE FINISH: TOLERANCES: LINEAR: ANGULAR:	Memorial University of Newfoundland Autonomous Ocean Systems Laboratory	DEBURR AND BREAK SHARP EDGES		NAME	SIGNATURE	DATE	PROJECT expDesign	REVISION:	
		MATERIAL: Various	DRAWN	Matt Gauthier		24.08.2016	TITLE: FOIL_ASM2 w/o Foil	SCALE:1:10	
		QUANTITY:	CHK'D				DWG NO. MTMG-10	SHEET 1 OF 1	A4

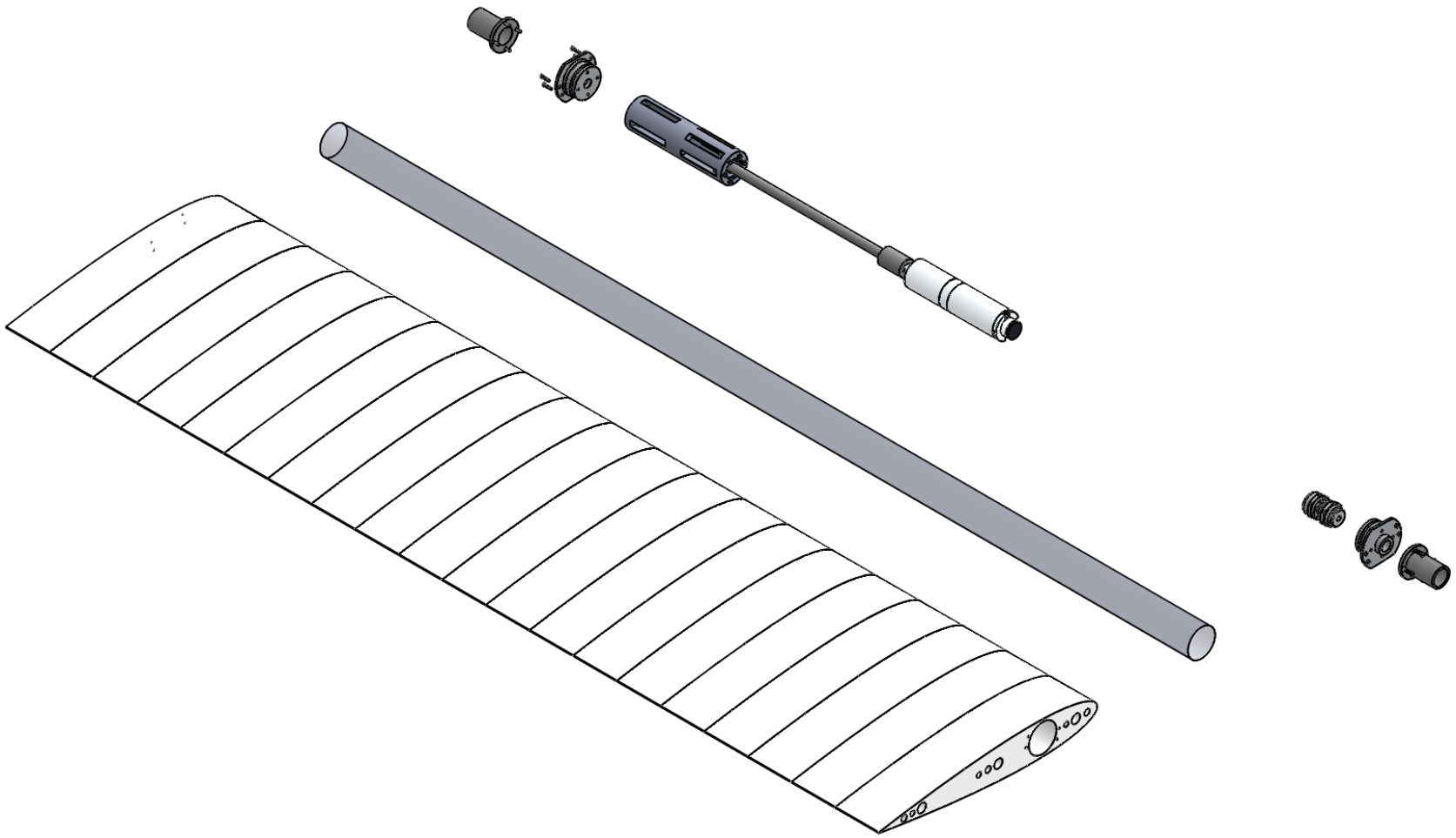

UNLESS OTHERWISE SPECIFIED:
DIMENSIONS ARE IN: mm [Inches]
SURFACE FINISH:
TOLERANCES:
LINEAR:
ANGULAR:

Memorial University of Newfoundland

Autonomous Ocean Systems Laboratory

DEBURR AND BREAK SHARP EDGES

			NAME	SIGNATURE	DATE	PROJECT	REVISION:
MATERIAL:	Various	DRAWN	Matt Gauthier		24.08.2016	TITLE: FOIL_ASM_EXPLODE_EXPLODE	SCALE:1:20
QUANTITY:		CHK'D				DWG NO. MTMG-11	SHEET 1 OF 1 A4

expDesign

nB. Platic dowels and screws to be used for alignment and assembly.

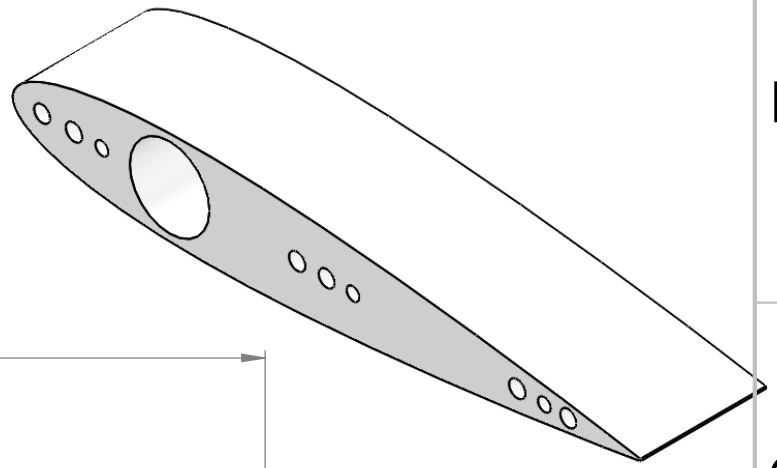

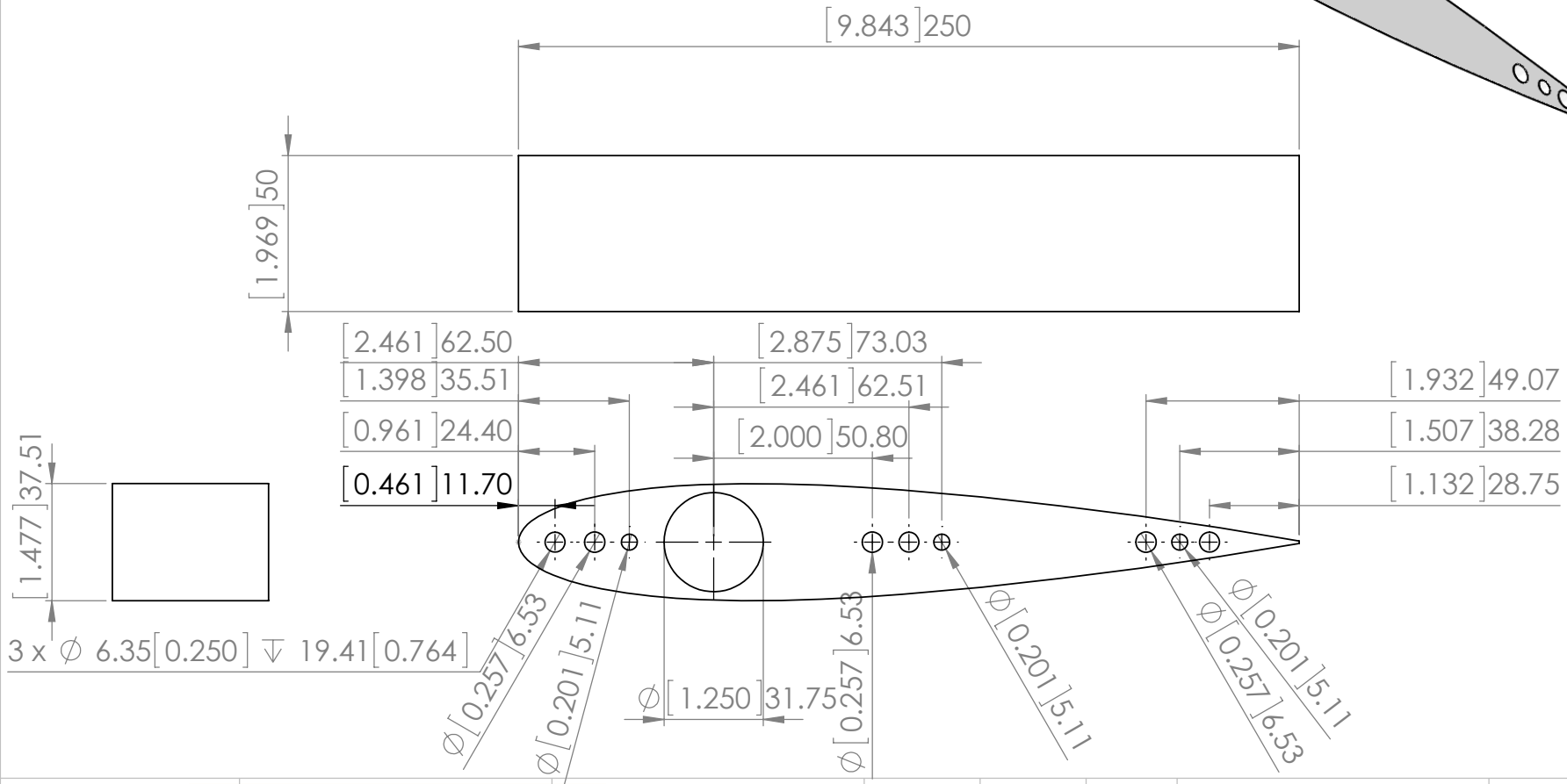

UNLESS OTHERWISE SPECIFIED: DIMENSIONS ARE IN: mm [Inches] SURFACE FINISH: TOLERANCES: LINEAR: ANGULAR:	Memorial University of Newfoundland Autonomous Ocean Systems Laboratory	DEBURR AND BREAK SHARP EDGES		NAME	SIGNATURE	DATE	PROJECT expDesign	REVISION:
		MATERIAL: HDPE	DRAWN	Matt Gauthier		24.08.2016	TITLE: foilSegment	SCALE:1:2
		QUANTITY: 20	CHK'D				DWG NO. MTMG-12	SHEET 1 OF 1 A4

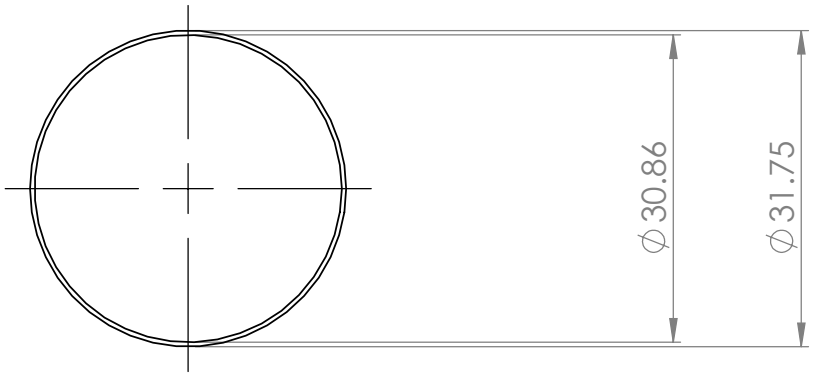

DETAIL B
SCALE 7 : 5

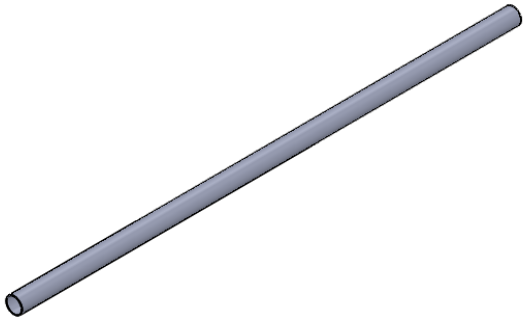

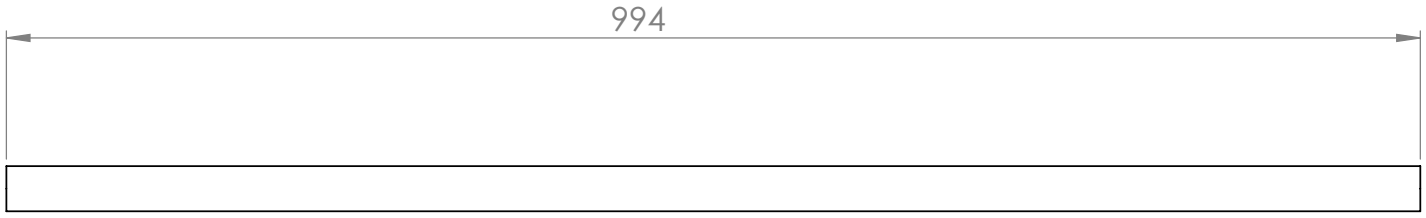

UNLESS OTHERWISE SPECIFIED: DIMENSIONS ARE IN: mm [Inches] SURFACE FINISH: TOLERANCES: LINEAR: ANGULAR:	Memorial University of Newfoundland Autonomous Ocean Systems Laboratory	DEBURR AND BREAK SHARP EDGES		NAME	SIGNATURE	DATE	PROJECT expDesign	REVISION:	
		MATERIAL: Al. 6061	DRAWN	Matt Gauthier		18.03.2017	TITLE: housingTube	SCALE:1:10	
		QUANTITY:	CHK'D				DWG NO. MTMG-13	SHEET 12 OF 18	A4

nB. All slots have same dimensions [6 x 40].

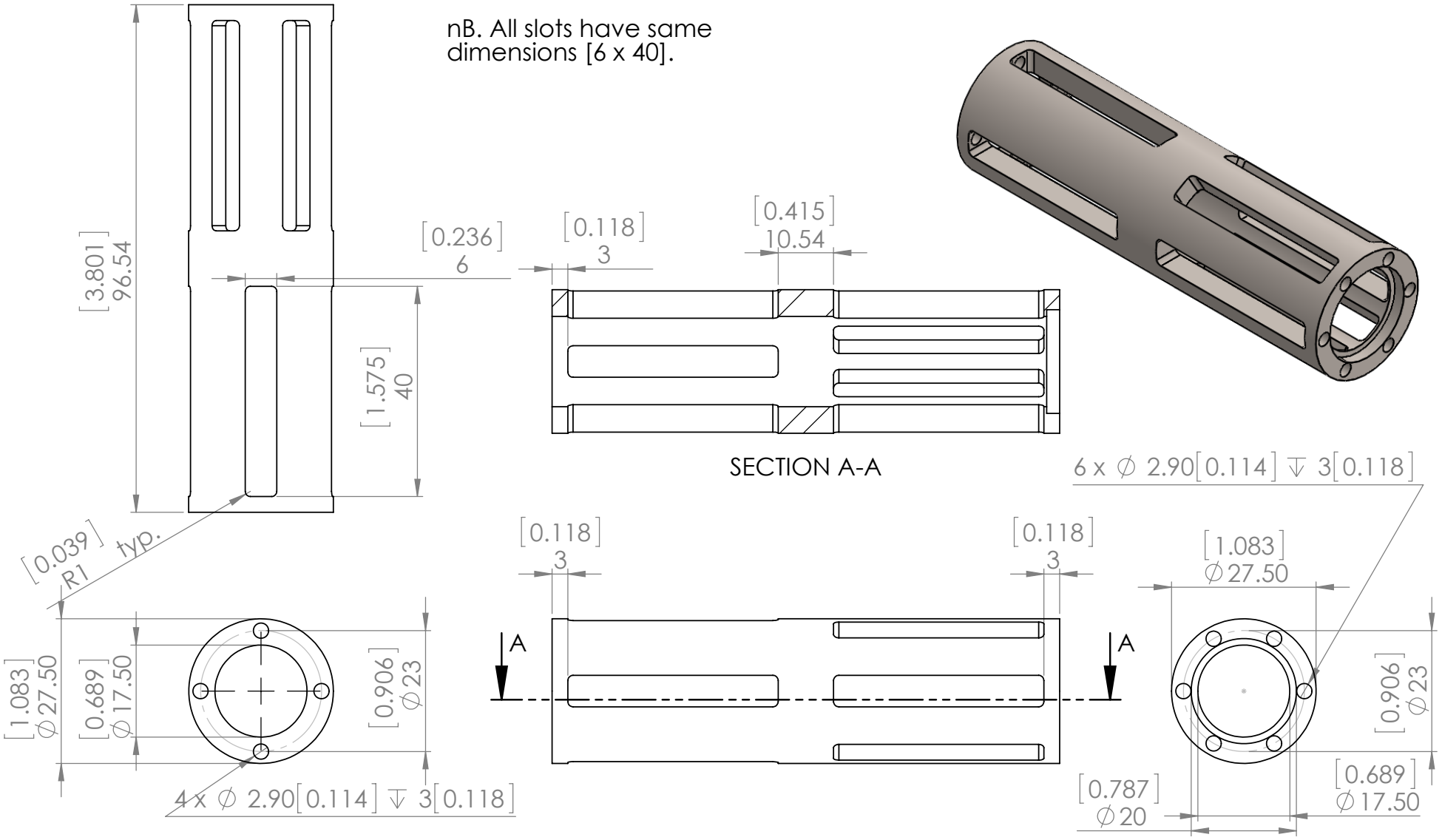

UNLESS OTHERWISE SPECIFIED: DIMENSIONS ARE IN: mm [Inches] SURFACE FINISH: TOLERANCES: LINEAR: ANGULAR:	Memorial University of Newfoundland Autonomous Ocean Systems Laboratory	DEBURR AND BREAK SHARP EDGES		NAME	SIGNATURE	DATE	PROJECT expDesign	REVISION:
		MATERIAL: Al. 6061	DRAWN	Matt Gauthier		09.04.2017	TITLE: motorAdapter	SCALE:1:1
		QUANTITY:	CHK'D				DWG NO. MTMG-14	SHEET 13 OF 18 A4

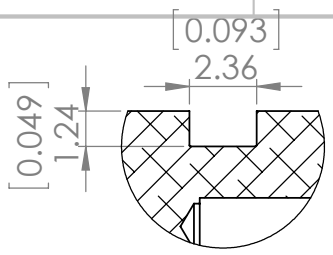

DETAIL C
SCALE 4 : 1

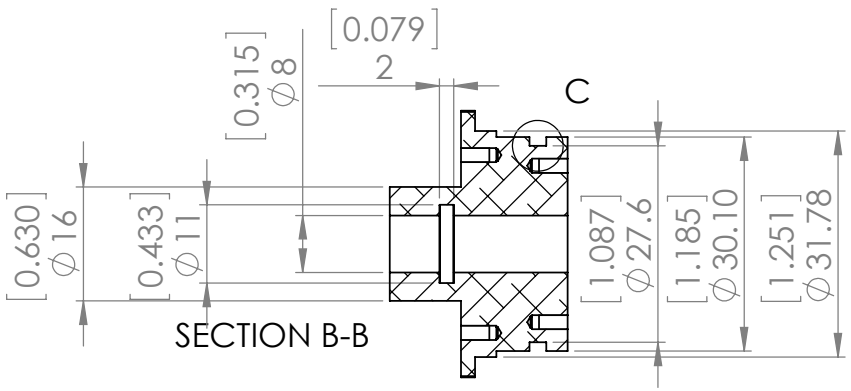

SECTION B-B

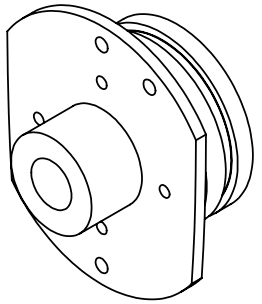

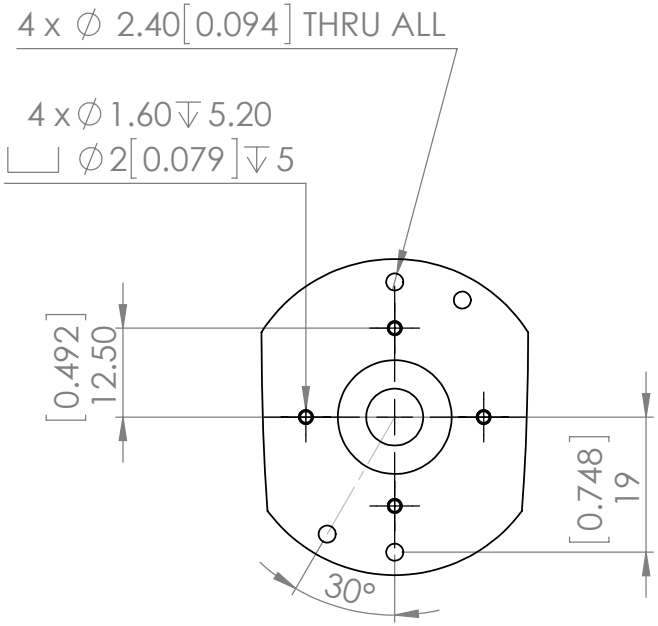

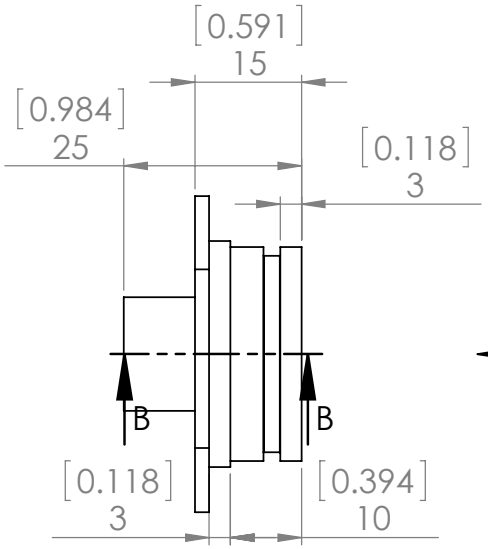

D

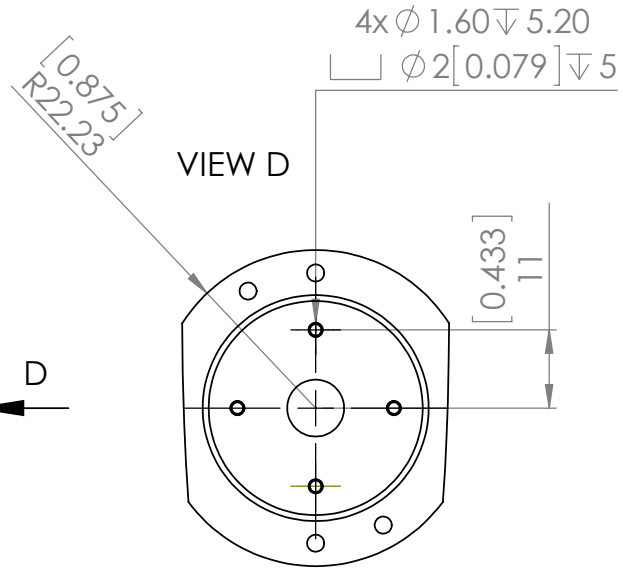

UNLESS OTHERWISE SPECIFIED: DIMENSIONS ARE IN: mm [Inches] SURFACE FINISH: TOLERANCES: LINEAR: ANGULAR:	Memorial University of Newfoundland Autonomous Ocean Systems Laboratory	DEBURR AND BREAK SHARP EDGES		NAME	SIGNATURE	DATE	PROJECT: expDesign	REVISION:
		MATERIAL: Al 6061	DRAWN	Matt Gauthier		09.04.2017	TITLE: endCapA	SCALE:1:1
		QUANTITY:	CHK'D				DWG NO. MTMG-15	SHEET 14 OF 18 A4

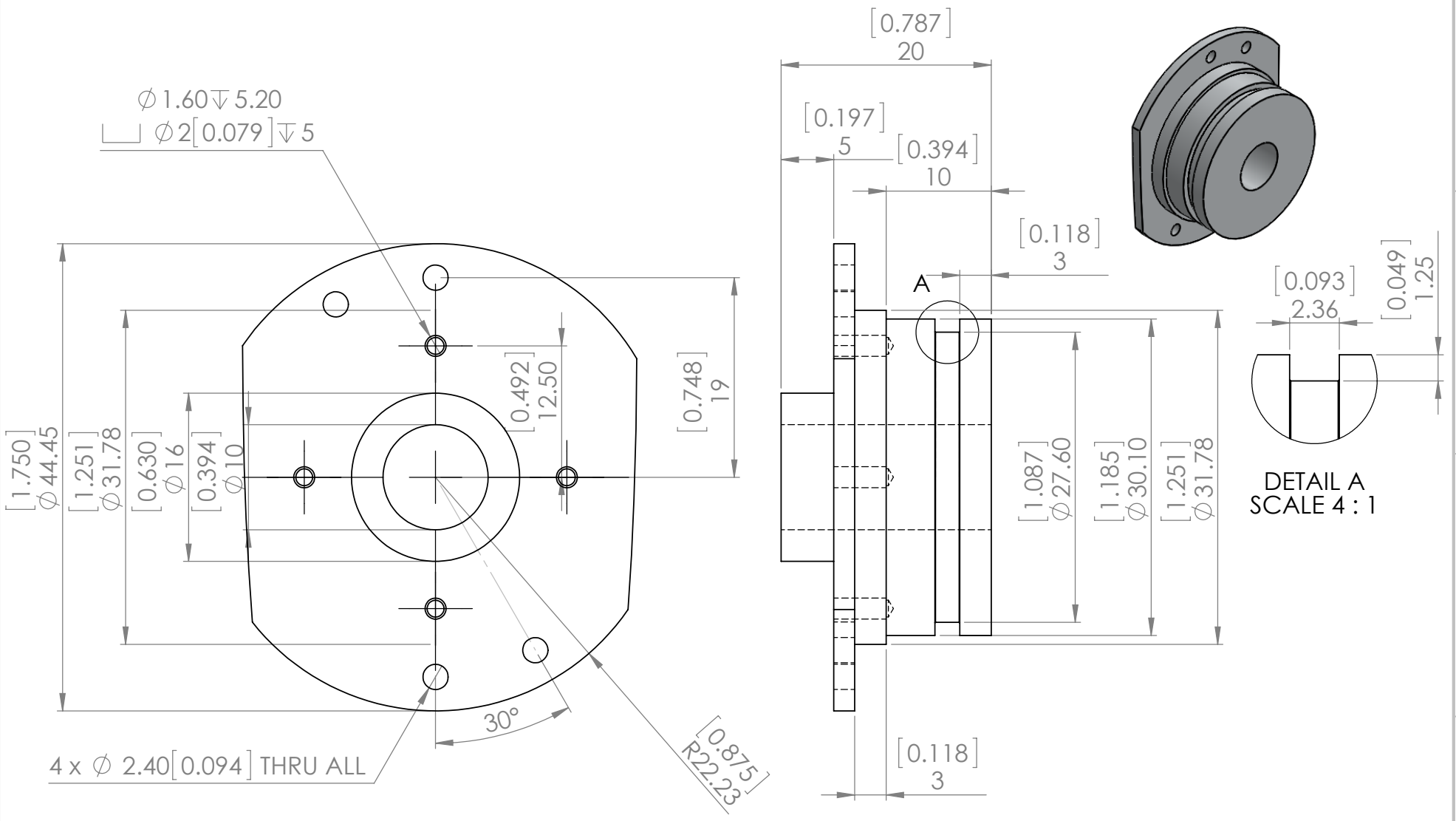

UNLESS OTHERWISE SPECIFIED: DIMENSIONS ARE IN: mm [Inches] SURFACE FINISH: TOLERANCES: LINEAR: ANGULAR:	Memorial University of Newfoundland Autonomous Ocean Systems Laboratory	DEBURR AND BREAK SHARP EDGES		NAME	SIGNATURE	DATE	PROJECT: expDesign	REVISION:
		MATERIAL: Al 6061	DRAWN	Matt Gauthier		18.03.2017	TITLE: endCapB	SCALE:1:1
		QUANTITY: 1	CHK'D				DWG NO. MTMG-16	SHEET 15 OF 18 A4

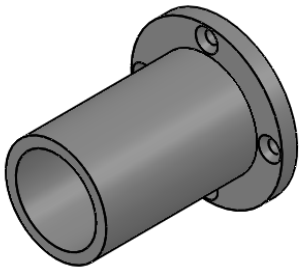

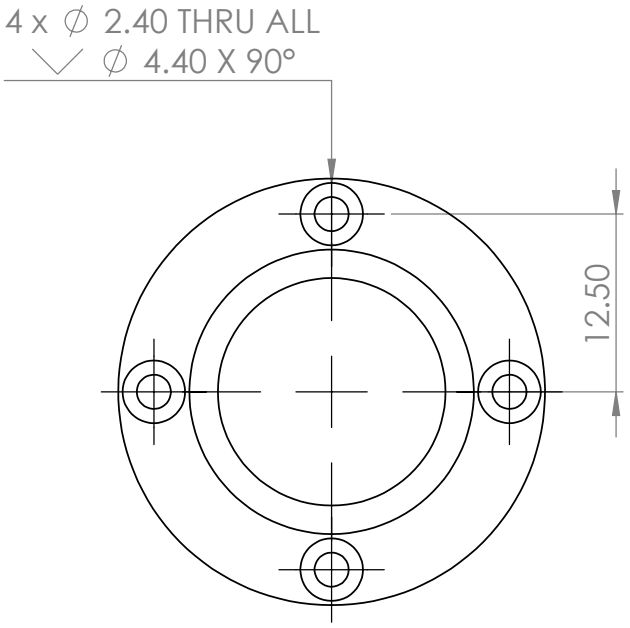

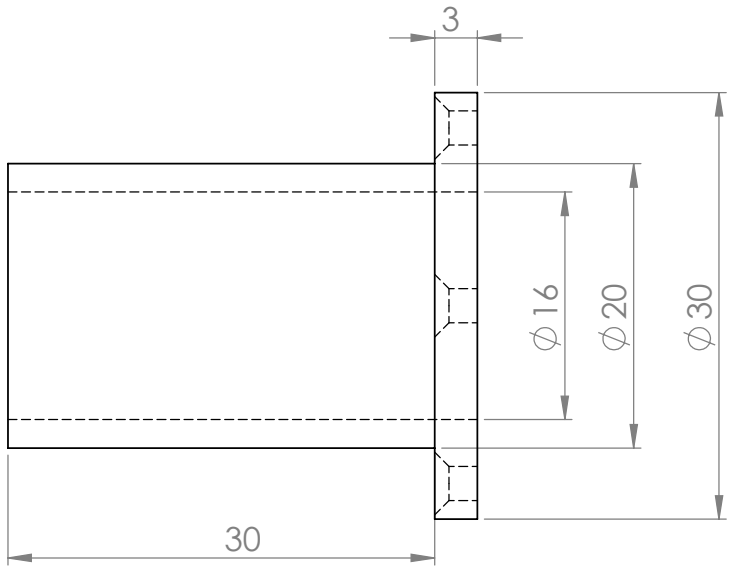

UNLESS OTHERWISE SPECIFIED: DIMENSIONS ARE IN: mm [Inches] SURFACE FINISH: TOLERANCES: LINEAR: ANGULAR:	Memorial University of Newfoundland Autonomous Ocean Systems Laboratory	DEBURR AND BREAK SHARP EDGES		NAME	SIGNATURE	DATE	PROJECT: expDesign	REVISION:
		MATERIAL: Al 6061	DRAWN	Matt Gauthier		18.03.2017	TITLE: Bushing	SCALE:1:1
		QUANTITY:	CHK'D				DWG NO. MTMG-17	SHEET 16 OF 18 A4

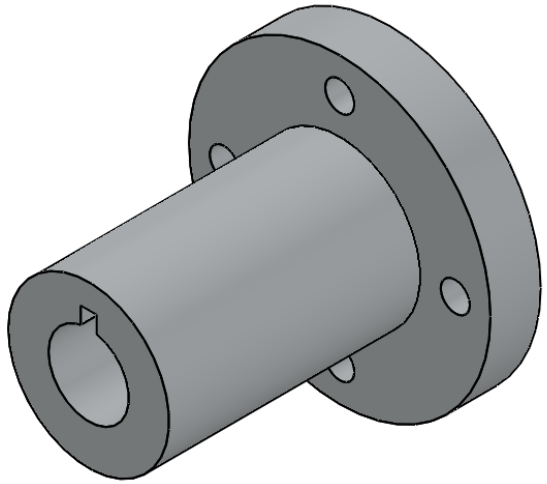

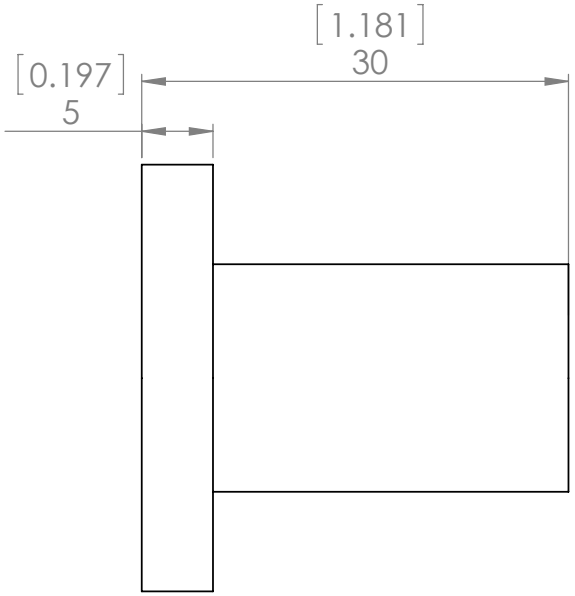

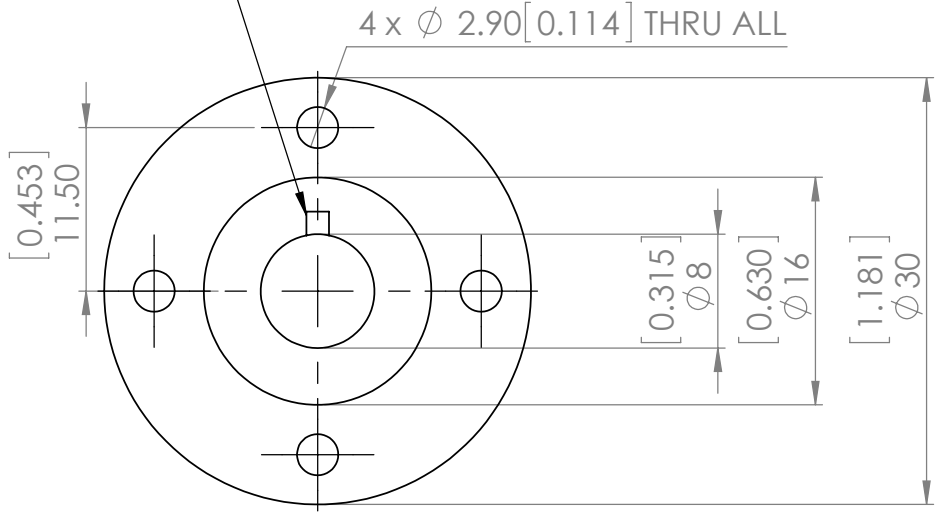

UNLESS OTHERWISE SPECIFIED: DIMENSIONS ARE IN: mm [Inches] SURFACE FINISH: TOLERANCES: LINEAR: ANGULAR:	Memorial University of Newfoundland Autonomous Ocean Systems Laboratory	DEBURR AND BREAK SHARP EDGES		NAME	SIGNATURE	DATE	PROJECT: expDesign	REVISION:
		MATERIAL: Al. 6061	DRAWN	Matt Gauthier		18.03.2017	TITLE: Shaft_Ground	SCALE:2:1
		QUANTITY:	CHK'D				DWG NO. MTMG-18	SHEET 17 OF 18 A4

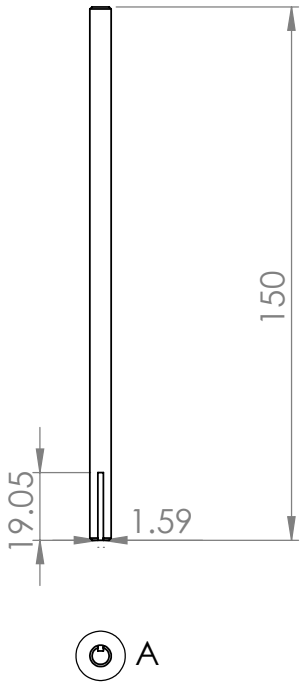

A

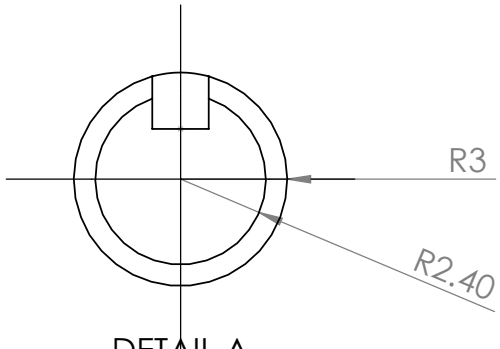

DETAIL A
SCALE 5 : 1

UNLESS OTHERWISE SPECIFIED: DIMENSIONS ARE IN: mm [Inches] SURFACE FINISH: TOLERANCES: LINEAR: ANGULAR:	Memorial University of Newfoundland Autonomous Ocean Systems Laboratory	DEBURR AND BREAK SHARP EDGES		NAME	SIGNATURE	DATE	PROJECT: expDesign	REVISION:
		MATERIAL: SS	DRAWN	Matt Gauthier		18.03.2017	TITLE: shaft	SCALE:1:2
		QUANTITY:	CHK'D				DWG NO. MTMG-19	SHEET 18 OF 18 A4

D Teensy Code

```
#include <Encoder.h>
#include <Metro.h>
#include <ADC.h>

#define ADC_RESOLUTION 12

#Define variables
float vreme, exvreme, error_rpm, error_theta, error_theta1, ts, EMANew, alpha, alpha2;
//vreme means time in Serbian
float EMAOld = 0;
float c_theta = 0, c_thetaOld;
float iFoil = 5.719;          //6.15 dry; 5.719 wet;
double c_rpm;          //commanded RPM
double theta = 0, theta1, thetaOld;     //motor angle
double del_theta = 0;
double rpm = 0;          //motor RPM
double acc = 0, acc1, accOld;       //acceleration
double gain_rpm, setGain, checkFreq, rpmOld, rpm1;  //rpm PI(D) output
float accum_rpm = 0;          //integral of rpm error
float accum_theta = 0;          //integral of RPM error
int exenc = -999;          //previous encoder reading
int del_enc = -499;          //delta only
double del_rpm, exrpm;
int cpr = 1024;          //encoder counts per revolution
char receivedChar;
int pwmpin = 23;   //Teensy PWM pin (A9)
int dir = 2;   //Teensy motor direction pin
double duty = 0.0;   //PWM duty cycle
int direc;   //motor direction (0 or 1)
char rc;
double gearRatio = 150;  //gear ratio
```

```
double spring;    //current from motor driver Current Sensor
int avgN, avgN2;
//int led = 13;

// ADC variables
const int inputCurrentPin = A0;
ADC *adc = new ADC();   //adc object
int currentSample = adc->analogRead(inputCurrentPin, ADC_0);
ADC::Sync_result result;
float current, curentSampleFloat;



//cascaded controller : RPM internal loop, Position outside
double kp_rpm = 0.0085;   //RPM PI(D) loop proportional gain
double ki_rpm = 0.008;    //RPM PI(D) loop integral gain
float kp_theta = 4.5;    //Position (angle) PI(D) loop proportional gain
float ki_theta = 0.15;    //Position PI(D) loop integral gain

// System Properties

int Ks = 3; //[Nm/rad]

const byte numChars = 90;
char receivedChars[numChars];
const char * pReceivedChar;
boolean newData = false;

float period_calculate_ms = 1;
//time period for pwm_duty_updater_metro and calculate_vars_metro

double ang = 0;  //(at the moment) command angle amplitude - used
```

```
double mag = 0.0;  //max command angle magnitude − not used
double freq = 0.0;


Encoder myEnc(12, 15); //Teensy pins for encoder A and B quadrature signal


Metro pwm_duty_updater_metro = Metro(period_calculate_ms);
Metro serial_print_metro = Metro(30); //30
Metro serial_read_metro = Metro(10);
Metro calculate_vars_metro = Metro(period_calculate_ms);


void setup() {
  //pinMode(led, OUTPUT);     //initialize the digital pin as an output.
  Serial.begin(28800);
  pinMode(pwmpin, OUTPUT);
  pinMode(dir, OUTPUT);

  analogWriteFrequency(pwmpin, 20000);  //set PWM frequency
  avgN = 100;
  alpha = 2.0 / (avgN + 1.0);


  // Setting up the ADC measurement in continuous mode for ADC 0
  pinMode(inputCurrentPin, INPUT);
  adc−>setAveraging(1);     // set number of averages
  adc−>setResolution(ADC_RESOLUTION);  // set bits of resolution
 // it can be ADC_VERY_LOW_SPEED, ADC_LOW_SPEED, ADC_MED_SPEED,
 // ADC_HIGH_SPEED_16BITS, ADC_HIGH_SPEED or ADC_VERY_HIGH_SPEED
```

```
  adc->setConversionSpeed(ADC_CONVERSION_SPEED::VERY_HIGH_SPEED ); //
      ↪ change the conversion speed

 // it can be VERY_LOW_SPEED, ADC_LOW_SPEED, ADC_MED_SPEED,
     ↪ ADC_HIGH_SPEED or ADC_VERY_HIGH_SPEED

  adc->setSamplingSpeed(ADC_SAMPLING_SPEED::VERY_HIGH_SPEED ); // change the
      ↪ sampling speed
  adc->startContinuous(inputCurrentPin);

}

void loop() {

  ts = millis();     //start time
  while (true) {

    //digitalWrite(led, HIGH);  //turn the LED on (HIGH is the voltage level)

    //exponential moving average (comment out for prescribed mode)
    currentSample = (uint16_t) adc->analogReadContinuous(inputCurrentPin);
    curentSampleFloat = (((float)3.3 * currentSample / (int)(0xFFFF >> (16 -
        ↪ ADC_RESOLUTION))) - 2.4) /   0.066;

    current = EMAOld + alpha * (curentSampleFloat - EMAOld);
    EMAOld = current;



    if (serial_read_metro.check() == 1) {
      recvWithStartEndMarkers();
      pReceivedChar = (const char*) receivedChars;
```

```
    sscanf(pReceivedChar, "%lf,%lf,%lf,%*f\n", &ang, &mag, &freq);
    //c_rpm = ang; //read command angle
    //setGain = ang; //Steady State
    //Ks = ang; //For Spring Mode
    c_theta = ang; //For Prescribed Mode
  }



  if (pwm_duty_updater_metro.check() == 1) {
    pwm_duty_updater();
  }

  if (serial_print_metro.check() == 1) {
    Serial.printf("%f,%f,%f,%f,%f \n", vreme / 1000, theta, rpm, acc, current);
    //print data to serial
    newData = false;
  }

  if (calculate_vars_metro.check() == 1) {
    int enc = (myEnc.read()); //read encoder count

    vreme = millis() - ts;  //time in milliseconds

    if (accum_rpm > 2000 and error_rpm > 0) {
      accum_rpm += 0;   //RPM error integrator with a limit
    }
    else if (accum_rpm < -2000 and error_rpm < 0) {
      accum_rpm += 0;
    }
    else {
```

```
  accum_rpm += error_rpm;
}

if (accum_theta > 2000 and error_theta > 0) {
  accum_theta += 0;   //Position error integrator with a limit
}
else if (accum_theta < -2000 and error_theta < 0) {
  accum_theta += 0;
}
else {
  accum_theta += error_theta;
}

del_enc = enc - exenc;

theta = (myEnc.read() * 360.0) / (4.0 * cpr * gearRatio);
//theta [degrees] = (encoder_count*360)/(4*encoder_counts_per_revolution);
exenc = enc;
error_theta = c_theta - theta; //Need for spring

c_rpm = kp_theta*(c_theta-theta)+ki_theta*accum_theta; //Positoin PI(D) outputs
    ↪ RPM command

rpm = (double)(del_enc / (double)((period_calculate_ms / 1000.0) * 4.0 * cpr * gearRatio
    ↪ )) * 60.0;
//fixed delta time of period_calculate_ms is used for RPM calculation

acc = (double)(del_enc / (double)(4.0 * cpr * gearRatio * (period_calculate_ms / 1000.0)
    ↪ *       (period_calculate_ms / 1000) * 4 * cpr * gearRatio)) * ((60.0 * 60.0));

/* else
```

```
        {
         Serial.printf("%f,%f,%d,%d \n", 1.1, 2.2, 3, 4); //print data to serial
        }*/


    }

    // digitalWrite(led, LOW); // turn the LED off (LOW is the voltage level)
  }


}

void pwm_duty_updater() { //updates pwm duty cycle through PI speed controller

  //gain_rpm = −1; //Need for steady state motion (CW = 1; CCW = −1)
  //gain_rpm = iFoil ∗ acc + (Ks ∗ error_theta) + 0.26 ∗ rpm + bias; // Need for spring−mode
  gain_rpm = kp_rpm∗(c_rpm−rpm)+ki_rpm∗accum_rpm;       //Need for prescribed motion

  if (gain_rpm > 0)       //motor direction
    direc = 1;
  else
    direc = 0;

// Uncomment for steady state motion
// gain_rpm = abs(gain_rpm);  //sets duty cycle (max duty cycle 255)
// duty = gain_rpm∗setGain;
// if (duty > setGain)
// duty = setGain;
//
// gain_rpm = abs(gain_rpm);  //Need for spring motion
```

```
// duty = gain_rpm;
// if (duty > gain_rpm)
// duty = gain_rpm;



  gain_rpm = abs(gain_rpm);  //Need for prescribed motion
  duty = gain_rpm * 255;
  if (duty > 255)
    duty = 255;
  //
  digitalWrite(dir, direc); //update direction
  analogWrite(pwmpin, duty); //update duty cycle
}

void recvWithStartEndMarkers() { //https://forum.arduino.cc/index.php?topic=288234.0
  static boolean recvInProgress = false;
  static byte ndx = 0;
  char startMarker = '<';
  char endMarker = '\n';
  char rc;

  if (Serial.available() > 0) {
    while (Serial.available() > 0 && newData == false) {
      rc = Serial.read();

      if (recvInProgress == true) {
        if (rc != endMarker) {
          receivedChars[ndx] = rc;
          ndx++;
          if (ndx >= numChars) {
            ndx = numChars - 1;
```

```
            }
          }
          else {
            receivedChars[ndx] = '\n'; // terminate the string
            recvInProgress = false;
            ndx = 0;
            newData = true;
          }
        }

        else if (rc == startMarker) {
          recvInProgress = true;
        }
      }
    }
}
```

E Load Cell and Motor Specifications

MINIATURE LOW PROFILE TENSION LINKS
LOW PROFILE 0.75" TO 1" HEIGHT

LC703 Series
Tension/Compression
Calibrated in Tension
±10 lb to ±1,000 lb
±45 N to ±4,500 N

1 Newton = 0.2248 lb
1 daNewton = 10 Newtons
1 lb = 454 g
1 t = 1000 kg = 2204 lb

LC703
$295
Model Shown

Model LC703-100
Shown Larger Than Actual Size

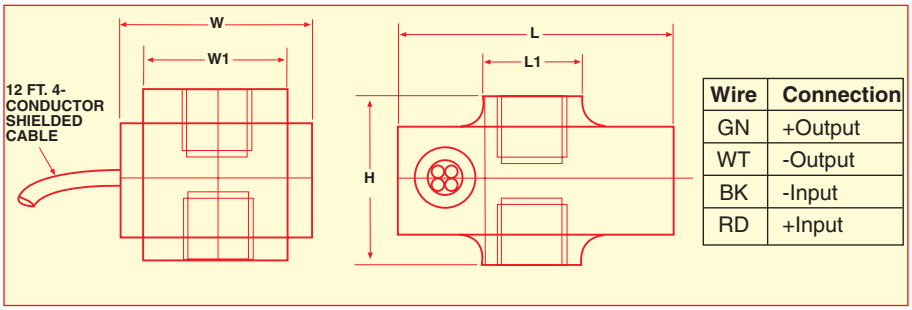

Wire	Connection
GN	+Output
WT	-Output
BK	-Input
RD	+Input

- **Low Profile**
- **High Accuracy**
- **Rugged Industrial Design**

The LC703 Series is an economical universal (Tension/Compression) load cell with an extremely low profile. Ranges above 100 lb are Stainless Steel; 100 lb and below are Aluminum. The LC703's low profile, economical price and rugged design make it suitable for many industrial applications including robotics, automated weighing systems or as part of a batch-process control system.

SPECIFICATIONS:

Excitation: 10 Vdc (15 V max)
Output: 2 mV/V nominal
5-Point Calibration:
0%, 50%, 100%, 50%, 0%
Linearity: 10 to 100 lb ±0.15% >100 lb ±0.10 FSO
Hysteresis: ±0.15% ±0.10FSO
Repeatability: ±0.05%
Zero Balance: ±1.0% FSO
Operating Temp Range:
-40 to 82°C (-40 to 180°F)
Compensated Temp Range:
16 to 71°C (60 to 160°F)
Thermal Effects:
Zero: ±0.005% FSO/°F
Span: ±0.005%% FSO/°F

Dimensions Shown in Inches (mm)

Capacity (lb)	L (Max)	L1	W	W1	H	Thread
±10	1.50 (38)	0.56 (14)	0.54 (14)	0.38 (9.5)	0.75 (19)	10-32x0.20
±25 to 100	1.62 (41)	0.56 (14)	0.66 (17)	0.50 (13)	0.75 (19)	¼-28x0.23
±150 to 1 K	1.75 (44)	0.56 (14)	0.93 (24)	0.75 (19)	1.0 (25)	⅜-24x0.38

Safe Overload: 150% of Capacity
Ultimate Overload: 300% of Capacity
Output Resistance: 350 Ω ±10 Ω
Input Resistance: 360 Ω minimum
Full Scale Deflection: .003" nominal

Construction:
≤100 lb Aluminum
>100 lb 17-4 PH Stainless Steel
Electrical: 12 ft (3.6 m) shielded 4-conductor PVC cable

Most Popular Models Highlighted

To Order *(Specify Model Number)*

CAPACITY (lb)	MODEL NO.	PRICE	COMPATIBLE METERS*
±10	**LC703-10**	**$295**	DP41-W, DP41-S, DP25-S
±25	**LC703-25**	**295**	DP41-W, DP41-S, DP25-S
±50	**LC703-50**	**295**	DP41-W, DP41-S, DP25-S
±75	**LC703-75**	**295**	DP41-W, DP41-S, DP25-S
±100	**LC703-100**	**295**	DP41-W, DP41-S, DP25-S
±150	**LC703-150**	**295**	DP41-W, DP41-S, DP25-S
±200	**LC703-200**	**295**	DP41-W, DP41-S, DP25-S
±300	**LC703-300**	**295**	DP41-W, DP41-S, DP25-S
±500	**LC703-500**	**395**	DP41-W, DP41-S, DP25-S
±750	**LC703-750**	**395**	DP41-W, DP41-S, DP25-S
±1,000	**LC703-1K**	**395**	DP41-W, DP41-S, DP25-S

Metric Ranges Available - Consult Engineering **See Section D For Compatible Meters*

***Ordering Example: 1) LC703-200** is a 200 lb capacity universal link with 12 ft cable, **$295**.*
***2) LC703-500** is a 500 lb capacity tension link with 12 ft cable, **$395**.*

Your configured drive

Part number*: B772E2E3895E Revision 20

maxon motor
driven by precision

Motor - DCX26L GB KL 48V
Planetary gearhead - GPX26HP 150:1
Sensor - ENX16 EASY 1024IMP

maxon motor worldwide
http://www.maxonmotor.com/maxon/view/content/contact_page
E-Mail: e-shop@maxonmotor.com
Internet: www.maxonmotor.com

General Terms and Conditions: http://www.maxonmotor.com/maxon/view/content/terms_and_conditions_page

Interactive 3D model
Click on the icon to activate your 3D model

Your configuration can be viewed here:
http://www.maxonmotor.com/maxon/view/configurator/?ConfigID=B772E2E3895E

*If the link doesn't work, you can open your configuration with the part number from the catalog.

Attachments / CAD files

Please double click with left mouse button on a pushpin symbol to open a file. You could also save a file when you click the symbol with the right mouse button.

B772E2E3895E.stp (STP AP 214)

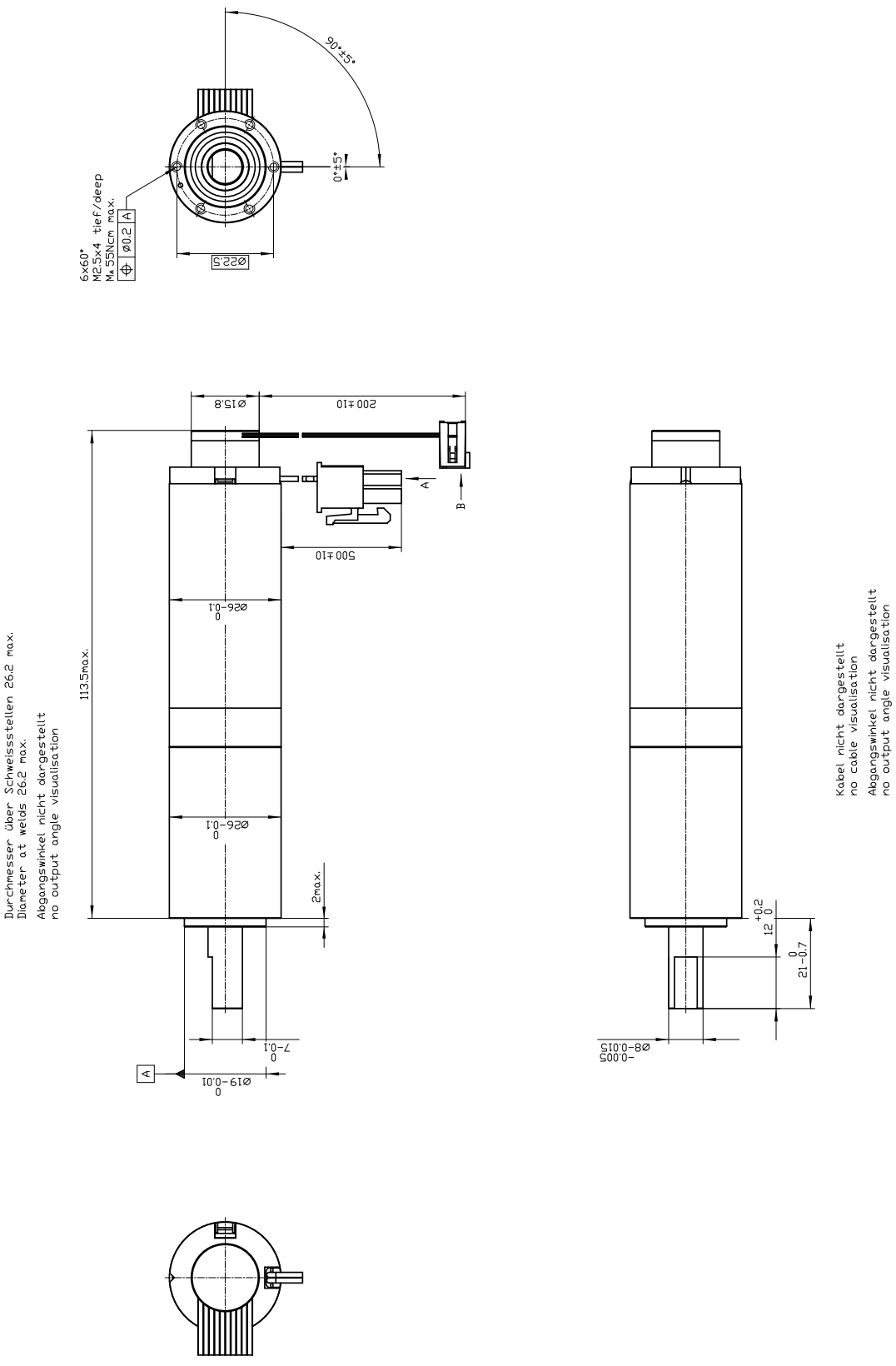

Drawings are not to scale!

Motor - DCX26L GB KL 48V
Planetary gearhead - GPX26HP 150:1
Sensor - ENX16 EASY 1024IMP

Motor - DCX26L GB KL 48V
Planetary gearhead - GPX26HP 150:1
Sensor - ENX16 EASY 1024IMP

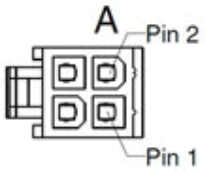

Connector type, motor	
Molex 39-01-2040	
Pin assignment	
Pin 1	red wire (+)
Pin 2	black wire (-)

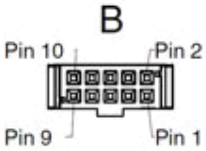

Connector type, encoder	
2.54mm 10-pol	
Pin assignment	
Pin 1	Not connected
Pin 2	VCC
Pin 3	GND
Pin 4	Not connected
Pin 5	Channel A\
Pin 6	Channel A
Pin 7	Channel B\
Pin 8	Channel B
Pin 9	Channel I\
Pin 10	Channel I

Summary of your selected configuration

Motor - DCX26L GB KL 48V
Planetary gearhead - GPX26HP 150:1
Sensor - ENX16 EASY 1024IMP

Total weight of the drive: 323 g

Motor: DCX26L GB KL 48V	
Commutation	Graphite brushes
Nominal voltage	48 V
Motor bearings	Preloaded ball bearing
Electrical connection, motor	
Electrical connection, motor	Cable
Connector type, motor	Molex 39-01-2040
Cable length	500 mm
Connection orientation	
Connection orientation	Configure output angle
Gearhead GPX26HP 150:1	
Gearhead type	High Power
Reduction	150
Number of stages	3
Sensor ENX16 EASY 1024IMP	
Counts per turn	
Counts per turn	1024
Encoder angle	90 degree

Operating range

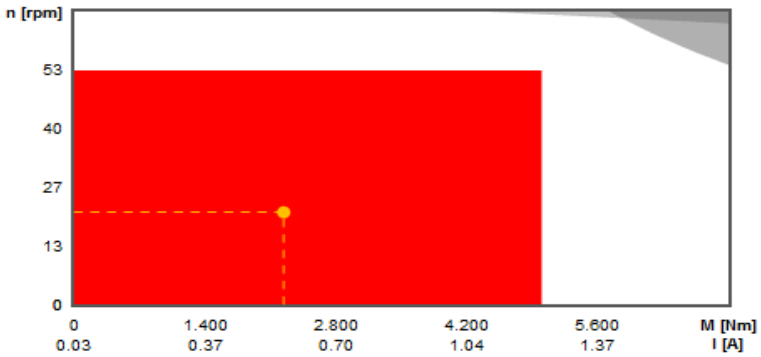

Continuous operation range
Short-term operating range
Continuous operation range at reduced thermal resistance Rth2 50%
Not recommended range

Motor - DCX26L GB KL 48V

Values at nominal voltage		
Nominal voltage	48	V
No load speed	10700	rpm
No load current	32.9	mA
Nominal speed	9730	rpm
Nominal torque (max. continuous torque)	59.1	mNm
Nominal current (max. continuous current)	1.41	A
Stall torque	697	mNm
Stall current	16.2	A
Max. efficiency	91.2	%
Characteristics		
Max. output power	73.4	W
Terminal resistance	2.95	Ohm
Terminal inductance	0.514	mH
Torque constant	42.9	mNm/A
Speed constant	223	rpm/V
Speed/torque gradient	15.3	rpm/mNm
Mechanical time constant	3.4	ms
Rotor inertia	21.2	gcm^2
Thermal data		
Thermal resistance housing-ambient	10.2	K/W
Thermal resistance winding-housing	3.01	K/W
Thermal time constant of the winding	23.8	s
Thermal time constant of the motor	620	s
Ambient temperature	-40..100	°C
Max. winding temperature	155	°C
Mechanical data		
Max. permissible speed	14400	rpm
Min. axial play	0	mm
Max. axial play	0.1	mm
Radial backlash	0.02	
Max. axial load (dynamic)	5.5	N
Max. force for press fits (static)	40	N
max. radiale Last 5 mm from flange	20.5	Nm

Further specifications		
Number of pole pairs	1	
Number of commutator segments	11	
Weight	172	g
Number of autoclave cycles	0	
Typical noise level	44	dBA

Information about motor data: http://www.maxonmotor.com/medias/CMS_Downloads/DIVERSES/12_137_EN.pdf

Planetary gearhead - GPX26HP 150:1

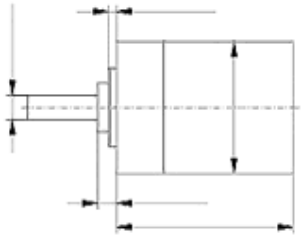

Gearhead data		
Reduction	150:1	
Absolute reduction	328509/2197	
Max. transmittable power (continuous)	30	W
Max. transmittable power (intermittent)	40	W
Number of stages	3	
Max. continuous torque	5	Nm
Max. intermittent torque	7	Nm
Direction of rotation, drive to output	=	
Max. efficiency	65	%
Weight	145	g
Average backlash no-load	1.1	degree
Mass inertia	3.438	gcm^2
Gearhead length	47.1	mm

Technical data		
Output shaft bearing	Ball bearings	
Gearhead type	GPX	
Max. radial backlash	0.1	mm
mm from flange	10	mm
Min. axial play	0	mm
Max. axial play	0.2	mm
Max. permissible radial load	180	N
mm from flange	10	mm
Max. axial load (dynamic)	110	N
Max. force for press fits	120	N
Recommended motor speed	8000	rpm
Max. intermittent input speed	10000	rpm
Min. recommended temperature range	-40..100	°C
Number of autoclave cycles	0	

Information about gearhead data: http://www.maxonmotor.com/medias/CMS_Downloads/DIVERSES/12_203_EN.pdf

Sensor - ENX16 EASY 1024IMP

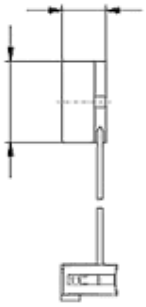

Type		
Counts per turn	1024	
Number of channels	3	
Line Driver	RS422	
Max. outer diameter	16	mm
Max. housing length	8.5	mm
Max. electrical speed	90000	rpm
Max. speed	30000	rpm

Technical data		
Supply voltage, typical	5	V
Supply voltage tolerance +/-	10	%
Output signal driver	Differential, EIA RS 422	
Current per cable	-20...20	mA
Min. state length	20	°el
Max. state length	160	°el
Signal rise time/Signal fall time	20/20	ns
Min. state duration	125	ns
Direction of rotation	A for B, CW	
Index position	A low & B low	
Index synchronously to AB	yes	
Index pulse width	90	e°
Typical current draw at standstill	23	mA
Max. moment of inertia of code wheel	0.05	gcm^2
Weight	6.4	g
Operating temperature range	-40..100	°C
Number of autoclave cycles	0	

Datasheet: http://www.maxonmotor.com/medias/CMS_Downloads/DIVERSES/ENXEASY_en.pdf